January 2010

Enhancing Nonlinear Ultrasonic Methods for Laboratory and Clinical Applications

Christopher Lloyd
Washington University in St. Louis

WASHINGTON UNIVERSITY IN SAINT LOUIS

Department of Physics

Dissertation Committee:

James G. Miller, Chair
Anders E. Carlsson
Mark S. Conradi
Mark R. Holland
Sándor J. Kovács
Ravi Rosalingam

Enhancing Nonlinear Ultrasonic Methods for Laboratory and Clinical Applications

by

Christopher William Lloyd

A dissertation presented to the
Graduate School of Arts and Sciences
of Washington University in
partial fulfillment of the
requirements for the degree
of Doctor of Philosophy

August 2010

Saint Louis, Missouri

Table of Contents

List of Figures

List of Tables

Acknowledgements

First and foremost, the research contained in this Thesis was performed using the facilities of the Laboratory for Ultrasonics at Washington University in Saint Louis. As such, I owe a great debt of gratitude to the principal investigator (and my thesis advisor), Dr. James Miller, for allowing me to gain exposure to the workings of the group during my first few summers in the Physics department, and then allowing me to work full-time on ultrasonic research projects. During my entire time with the research group, he was an invaluable asset not only to offer assistance with the day-to-day research issues, but also kept a keen eye on the big picture of the research projects and trajectories for future work.

Additionally, Dr. Mark Holland has been a wonderful advisor in the myriad workings of research in the Physics laboratory environment, as well as offering valuable insight into the collaborative aspects of research with people who come from a medical background. Dr. Kirk Wallace, on the other hand, was an influence in my continuing interest in nonlinear ultrasound, while also providing guidance in the proper laboratory methods for the systematic study of ultrasound. Additionally, the study that forms the basis for Chapter 2 originated from work that was initially performed by Dr. Wallace, who initiated the use of steel delay lines for use in the focal diffractive regime at 7 MHz. And, all of the members of the Laboratory For Ultrasonics have shaped me as a researcher as well as a person. They include Dr. Scott Handley, Dr. Rebecca Trousil, Dr. Karen Marutyan, Dr. Steve Baldwin, Dr. Min Yang, Dr. Adam Bauer, Dr. Allyson Gibson, Stephanie Posdamer, Todd Krueger, Chris Anderson, Joe Hoffman, Ben Johnson, and Amber Nelson, which does not include the members of the Laboratory from

the past, whose legacies remain in the problems that they solved and the equipment they manufactured for future researchers to utilize.

The continuing collaborations of the Laboratory for Ultrasonics with ongoing efforts in the School of Medicine provide a wonderful opportunity to learn about ultrasound in the context of medical imaging. Of special note is a collaboration that was undertaken with the Cardiovascular Biophysics Laboratory, which was responsible for the clinical data that underpins the chapters concerning the cyclic variation of myocardial backscatter. To that end, I thank Dr. Sándor Kovács, who leads the Cardiovascular Biophysics Laboratory and is a tremendously talented researcher from both the Physics and the medical schools of thought, as well as the researchers with whom I worked during the collaboration (Dr. Charles Chung, Dr. Wei Zhang, Leo Shmuylovich, Erina Ghosh, and Sina Mossahebi). The analysis of the clinical data to determine the parametrized diastolic filling formalism parameters, which was necessary for the comparisons of Chapter 6, was performed by members of Dr. Kovács' laboratory. The staff of the Cardiac Catheterization Laboratory at Barnes Hospital has been a tremendous aid in the study of ultrasonic imaging in patients, both through their patience with the research process and their superb ability to conduct patient procedures with the highest level of care. Of special note is Peggy Brown, who has been the sonographer through these studies and gathers data of the highest quality possible, given the complexities of the echocardiographic setting.

Outside of the research setting, there are numerous people who have contributed so much to my development as a person and as a student. Too numerous to count are the teachers, in high school, and the professors, at Missouri University of Science and

Technology (where I attended for an undergraduate education), and at Washington University in Saint Louis, that fueled my desire to learn simply by teaching, and teaching very effectively. In particular, though, I thank Dr. Rebecca Trousil and Dr. Martin Israel, two professors at Washington University, for their oversight and suggestions on how to be an effective teaching assistant during the four years spent as a T.A. here at Washington University. Recognition also goes out to the other Physics students at Missouri University of Science and Technology for helping maintain our small but effective support group, to keep each other going when times were tough. The graduate students at Washington University deserve to be recognized for the same reason, since there are many long-standing traditions that may appear trivial at first, but function to mentor those who are new as well as keep people from isolation in their research as they get older. The weekly soccer game (Wednesdays, at noon, and hopefully staying that way forever), the ultimate Frisbee games, and the game and movie nights, in particular, were invaluable to me as I progressed through the program. The staff of Student Health not only patched up the injuries from the physical sports, but also served a valuable role in providing a support staff that helped remind me that I could take some satisfaction from the work contained in this Thesis, as well as find some joy in being a graduate student.

Since a wage sufficient to subsist upon is quite appreciated while advancing through research as a graduate student, I would like to thank the taxpayers of the United States of America for their generous support of government agencies, specifically the National Institutes of Health, the National Science Foundation, and the Food and Drug Administration. In this spirit, thanks are also given to those within the agencies who are

responsible for the funding of applications for grants of high scientific merit. Grants from the NIH and the NSF have partially supported my salary during my graduate studies. An NSF "Scholar-in-Residence at the FDA" grant provided a funding mechanism to broaden my (and our entire group's) horizons for science, by bringing us to Washington, D. C. as scholars-in-residence for varying amounts of time. Specifically, the work found in this thesis was funded, in part, by NIH HL040302, NIH HL072761, NIH HL053174, NIH AR057433, and NSF-FDA CBET 0717830.

On behalf of myself, as well as every graduate student who is not allowed to be light-hearted for a moment even in an acknowledgement section, I'd like to thank the various vendors of food and drink in the vicinity of Washington University. Our patronage is certainly symbiotic, as the wonderful restaurants of the Loop, as well as on campus, are oftentimes the best cure for a frustration in an experiment or a bad case of writer's block, for a small pittance of our graduate student salaries. For me, this exuberant praise includes coffee (both the instant variety as well as from the coffee shops that are nearby), as well as Pepsi's Mountain Dew (which has been a constant companion of mine for many years, through good flavors and bad).

Though I say it infrequently, and certainly don't express it as often as I should, I'd like to thank my extended family for their support through the years. It has meant a lot to me to have so many wonderful aunts, uncles, and cousins who get excited about my progress in graduate school despite the myriad walks of life that everyone has taken (doctors, lawyers, teachers, accountants, engineers, computer scientists, etc.). I have to thank my sister for her influences while I was younger, and for her support as I followed

in her footsteps in college despite our geographic separation. I hope that I can be as supportive of her and her children someday as she was of me.

Finally, I'd like to thank my parents (here referred to as "Mom" and "Dad"), who did their best with a stubborn mule of a son and all the problems I caused growing up. I find myself now grown up, somewhat mature, and thankful for all of the lessons and most of the memories that I have from all of those problems I gleefully created as a kid. I'd like to think they did a great job, and all I can hope for is that they find themselves proud of my accomplishments – none of which would have happened without their constant support.

Chapter 1: Introduction

The scope of this thesis is the study of nonlinear ultrasound, in both the clinical and the physical settings. In both of these settings, two challenges at hand are to increase the reliability, as well as the utility, of nonlinear ultrasonic methods to further the study of various materials (whether those materials are people in a medical setting, or some other material in a physics laboratory). By overcoming obstacles with the utility of nonlinear ultrasound, the measurement of the innate nonlinearity of a material may migrate from the physics laboratory to the clinical setting. Further, if the reliability of any of the measurement methods can be improved upon, then the usefulness of these methods for use in medicine as a quantitative clinical approach is validated. Because the settings involved are different in nature, the approach applied here is to address each of these seemingly disparate (but innately linked) research projects and settings in their own right, which will also serve to provide the motivation for the studies described in later chapters.

Part 1: The Physics of Nonlinear Ultrasonic Propagation

One of the primary focal areas for this thesis is the study of what is colloquially referred to as "nonlinear ultrasound". Specifically, this refers to the phenomenon of the progressive distortion of an ultrasonic pulse of amplitude sufficiently large that the distortion is not a linear function of the incident pressure, and the consequences of this

distortion on physical measurements. The nature of this nonlinear distortion, which has been described at length in other sources,[1-6] is explored in Chapters 3 and 4. A special case of interest occurs when the distortion in the ultrasonic pulse is a linear function of the propagation distance, an approximation that is valid under specific conditions. This distortion has been utilized to implement a dramatic improvement in echocardiographic imaging. In clinical imaging, the signals of interest are backscattered from the propagating ultrasonic wave, with the time of flight between the generation of the signal and the reception of the backscattered signal being used to infer the depth of the backscattering site. In this manner, ultrasonic images can be formed from the mapping of reflective (scattering) sites in the field. This method has been enhanced significantly with the use of the higher harmonics of the signal, generated by the intrinsic nonlinear properties of the medium being imaged. This enhancement comes about in part as a result of the higher frequency (from the nonlinear promotion of lower frequency pressure) and smaller footprint of the ultrasonic beam with less distortion in the near field of the transmitting transducer.[7]

The studies in the following chapters are concerned with the propagation of an ultrasonic pulse and the resultant nonlinear generation in the pulse. However, the concern of this thesis is the accurate determination of the intrinsic parameter of nonlinearity for specific media such as soft tissue, a goal that is more challenging than simply measuring the nonlinear distortion in the field. This parameter is widely referred to as the nonlinear parameter, and is often represented by the term B/A, where these coefficients represent the first two coefficients in a Taylor expansion of the equation of state of pressure. This parameter governs the rate at which a finite amplitude pressure

wave distorts, which is expected to differ among media exhibiting different material properties. This parameter has been measured and reported for a number of liquids, gases, and biological media of interest.[1, 2]

The measurement of the parameter B/A can follow one of several paths. Two broad categories are "finite-amplitude" methods[8-25] and "thermodynamic" methods.[2, 14, 16, 26-28] The thermodynamic methods are referred to as such because they do not require the propagation of a finite amplitude ultrasonic field, but instead study the intrinsic nonlinear parameter of materials through thermodynamic relations. These relations are usually determined by the measurement of the variation of specific material parameters while other parameters are held constant. A temperature based approach, for example, could measure the derivative of the sound speed with respect to pressure (holding the temperature of the sample constant) as well as the derivative of the sound speed with respect to temperature (holding the pressure constant).[2, 14, 16] Alternatively, the change in phase of an ultrasonic signal can be related to the underlying nonlinear parameter.[26, 27] Although the use of a phase approach has potential for the tomographic mapping of the nonlinear parameter in materials,[28] in general the thermodynamic approaches have thus far not proven to be practical for implementation in medical applications.

The other category of measurement methods is a finite amplitude approach. The term "finite amplitude" is used to set these methods apart from methods based on an "infinitesimal amplitude". In nonlinear applications, the behavior of an ultrasonic beam is determined, in part, by the local amplitude of the pressure in the beam. The "infinitesimal amplitude" approach makes use of a sufficiently low amplitude pulse that the physical distortion of the field is negligible, and the propagation of the ultrasonic

beam is a linear process. However, when the pressure in the field is sufficiently large (in echocardiographic applications, this might correspond to tens of kilopascals or larger) the distortion can no longer be neglected. The resulting distortion can be measured in a number of ways to infer the nonlinear parameter of a sample. Approaches employed include transmission through the sample,[12-17] a through-transmission setup that uses a relative measure between a known reference and the unknown sample,[18-25] pulse-echo methods that use a reflector at the rear wall of a sample[8, 9] and measurements of the backscattered pressure as a function of distance into the sample.[10, 11]

The through-transmission setup is simple in execution: the experiment revolves around the measurement of a transmitted ultrasonic pulse after the pulse travels a given distance through the sample of interest. The measurement of interest is the amount of nonlinear pressure that has developed over this distance, which can be related to the nonlinear parameter of the material. An early example by Thuras *et. al.*[12] illustrated this method for high-intensity pressure waves that propagate through an air tube (a horn), and a similar measurement has been described by Chavrier *et. al.* for various materials.[13] However, in most physical pressure fields, there are non-negligible effects from the diffraction of the wave as well as the attenuation (loss) in the sample. To overcome these effects, an approach has been described and used by several groups, which extrapolates the pressure amplitudes back to the origin (at the transmitting transducer), in order to discount the effects of both diffraction and attenuation.[14-17] An alternate way of approaching this method will be described in more detail in Chapter 2.

One downside to the through-transmission method from the previous authors is the need to know the pressure at multiple positions within the sample. This can be done

for fluids, given the proper experimental equipment, but is not usually feasible for solid materials. In such cases when the through-transmission method is impractical, a modification has been proposed or utilized by many authors. An early modification was utilized by Shklovskaya-Kordi,[18] in which a measure of the nonlinear pressure is done for two circumstances: through a reference material, and through a path of propagation where part of the reference material is displaced by the sample material of interest. This insertion method has been studied in several ways, including using a phase method[19] and a reverberation approach for materials with dissimilar impedances.[20] The method that has been most extensively studied, however, is a finite-amplitude insert-substitution (FAIS) approach. This term was assigned by Gong *et. al.*[21, 22] and involves the measurement of the nonlinearly generated pressure field at some fixed distance from a transmitting transducer. The key to the method is the exploitation of the propagation equation for a weakly nonlinear ultrasonic pulse (i.e. nonlinear, but of sufficiently small amplitude that the third harmonic pressure does not come into play over the path length of interest). This equation, along with compensations for the loss in the ultrasonic field due to reflections at sample interfaces, nonlinear generation in the overlying reference material, and attenuation in the sample, are combined to permit a relative measure of the nonlinear parameter in the sample. If the nonlinear parameter B/A is known for the reference material, then the parameter B/A for the sample can be determined absolutely. This method has been adopted and improved upon by Dong *et. al.*[23] as well as by others.[24, 25] These methodologies will be examined in more detail in Chapter 3.

A somewhat different method of measurement is a backscatter approach. This method uses a single transducer to both transmit and receive ultrasonic pressure pulses,

which are then used to glean information about the nonlinear parameter in the sample of interest. This method opens the possibility of implementation in clinical medicine, because backscatter methods are well suited for the clinical setting. The clinical echocardiographic method is also a backscatter method, so in principle the collection of data for determining the nonlinear parameter could occur at the same time that a standard echocardiographic image is generated. Further progress has been made by other groups[10, 11] to develop the methods for measuring the nonlinear parameter for a small region of a sample (rather than the entire path between the transducer and the sample site). In particular, Fujii *et. al.* demonstrated the feasibility of measuring the nonlinear parameter, for liver, and demonstrated that the nonlinear parameter differed between patients who had normal and those who had fatty-infiltrated livers.[10] The details of this theory, along with some implications of the Fujii *et. al.* manuscript, will be discussed in Chapter 4.

Part 2: The Cyclic Variation of Myocardial Backscatter

The overarching goals of the medical use of ultrasound have been, and are, two-fold: to give an accurate visual representation of structures in the tissue being examined (to be able to "see" the tissue), and to provide quantitative information about the state of the tissue to permit the accurate assessment of pathology. The former has been discussed in the context of nonlinear ultrasound, and is relevant here because imaging with the nonlinearly promoted frequencies in a propagating pressure field has been shown to improve image quality. The proper visualization of the anatomic features of the heart, for example, can aid in the diagnosis of hypertrophy (an enlarged heart), wall-motion abnormalities, and damage to the valves between the atria and ventricles. In addition,

quantitative information about the tissue of interest can also be determined using ultrasound. In this approach, colloquially known as tissue characterization, the direct observation or indirect inference of the physical parameters of the tissue can also provide information about the state of the tissue. Parameters, such as the backscatter from the tissue or the attenuation of the propagating sound wave through the tissue, can be measured to aid in the diagnosis of pathology.

One such parameter that has been utilized is known as the cyclic variation of myocardial backscatter, and was first investigated by Madaras *et. al.*[29] in 1983 and Barzilai *et. al.*[30] in 1984 in studies from our Laboratory. The study by Madaras *et al.* examined the scattering properties of the myocardium in a canine model using ultrasonic backscatter. Results demonstrated that the integrated backscatter (a measure of backscattered power) from a region of interest in the tissue changed in a systematic fashion over the heart cycle. The backscattered power from the heart

- decreases during systole such that it reaches a minimum near end-systole (the time when the contraction of the heart has completed), and
- returns to the original baseline level during diastole (when the heart relaxes).

The manuscript by Barzilai *et. al.* first illustrated the role of cyclic variation as a tissue characterization tool, by studying normally perfused myocardial tissue and that same tissue when it was made to be ischemic (deprived of blood flow). The exposed hearts of dogs were studied both prior to ischemic injury and immediately after ischemic injury (a "heart attack") was induced by occluding a segment of coronary artery. The magnitude of the cyclic variation of myocardial backscatter decreased as the tissue was injured from

a lack of oxygenated blood flow, and the timing of the pattern of cyclic variation with respect to cardiac contraction was altered, as well.

Subsequent to these studies, many other investigations have been performed to demonstrate the utility of cyclic variation as an aid in detecting the presence or progression of specific pathologies. The effects on the heart of a number of distinct pathologies were studied in this fashion:

- Myocardial ischemia (low blood flow)[30-36] and infarction (tissue death and resulting scar formation)[37-41]
- Left ventricular hypertrophy[42-45]
- Hypertrophic,[46] dilated,[47] and diabetic[48] cardiomyopathies
- Left ventricular filling (diastolic function)[49]
- Left ventricular contractility or contractile reserve[50-56]
- Valve stenosis (narrowing)[57, 58]
- Diabetes (in the absence of overt cardiac disease)[59, 60]
- Obesity[61]
- Renal disease[62]
- Muscular dystrophy[63]
- Hypothyroidism[64, 65]

Although the acquisition of the relevant data for the measurement of the cyclic variation of ultrasonic backscatter is carried out in somewhat different ways by different investigators, it is the manner chosen to reduce the acquired data that is focus of the work to be described here. Several distinct approaches, which are summarized in what follows, have been employed.

Peak-to-Peak Method

In this method, the magnitude of cyclic variation is determined by finding the strongest and weakest scattered signals over the period of the heart cycle, and determining the difference between the two (hence the term "peak-to-peak" method).[30-33, 37, 38, 40-43, 46, 49-54, 57, 62, 63, 66, 67] This method is simple to implement, but is also potentially susceptible to random noise in the ultrasonic signal. Typically, in order to improve the stability of the reported magnitude of cyclic variation for a particular patient, this peak-to-peak magnitude is averaged for several different heart cycles. However, this measurement has also been done in a reverse order, where the high and low values of the backscattered power are averaged across several beats, and the resultant average high and average low values are utilized to determine a cyclic variation by measuring the difference between the two.[31, 54] A closely related method is to average several consecutive "maximum" or "minimum" values and then use the average values to measure the magnitude of variation.[38, 46, 57, 62, 63]

Time Marker Difference Method

An alternate method for measuring the cyclic variation relies on the initial observation that the backscatter from specific regions of interest in the myocardium is usually at its maximum at end-diastole (when the heart has finished relaxing) and is at its minimum at end-systole (when the heart has finished squeezing).[34, 39, 47, 59, 60, 68, 69] Thus, the magnitude of cyclic variation can be alternatively defined as the backscattered power at end-diastole, minus the backscattered power at end-systole. This method measures an

apparent magnitude that is altered when the maximum and minimum of the backscatter do not occur at end-diastole and end-systole, respectively.[68]

A related method to the measurement of the difference between end-diastole and end-systole has been termed the cyclic variation index, or CVI, and has been employed in several papers.[44, 45, 58, 61, 64, 65] In this method, the difference between the backscattered power of end-diastole (ED) and end-systole (ES) is then normalized to the end-diastolic power,

$$CVI = \frac{ED - ES}{ED} \bullet 100\% \quad (1)$$

This method, by normalizing to the end-diastolic backscatter level, loses the parameter's independence from the system gain, because an arbitrary change in system gain will affect the cyclic variation index, independent of the underlying change in the end-systolic and end-diastolic backscattered powers.

Model-Fit Method

A fundamentally different approach from the measurement of extrema data points was first proposed by Mohr *et. al.* in 1989.[48, 70-73] This approach relies on the systematic variation of the backscatter from the myocardium, and fits an appropriate model to the shape of the variation over the heart cycle. Because this variation resembles a pulse (decreasing during systole, and returning to a baseline level during diastole), the proposed model uses a smoothed rectangular pulse. This shape is fit to the raw data using correlation as well as a selective power spectral approach to determine the amplitude of the pulse. Once the model-fit waveform is determined, the magnitude of cyclic variation can be determined from the variation of the model, rather than from the raw data. This

approach inherently handles noisy variations in the data through the correlation of a model, and can be used to automatically determine the magnitude of the cyclic variation as well as the timing relative to cardiac systole of the decrease of the backscattered power. The model that is used for the determination of cyclic variation may also be related to the physiologic changes in the myocardium that are responsible for the change in backscatter over the heart cycle.[71]

Fundamental Frequency Magnitude Method

An alternative to the model of the model-fit method discussed above is to fit a sine wave to the backscattered ultrasonic data, where the period of the sine wave is constrained to the period of the heart cycle.[35, 55, 56, 74] This model has the advantage of being calculated rapidly using a Fourier transform of the data, because the fundamental frequency component of the Fourier transform is simply related to the sine wave of the model. This can be confirmed by applying an inverse Fourier transform to the fundamental component alone. However, the goodness-of-fit for this model to the underlying data is dependent on how closely the data approximates a sine wave, which may or may not be a good fit. Another advantage of this method is that the phase of the sine wave is related to the relative location of the nadir in the cyclic variation data. Knowledge of both the phase and the magnitude of the fundamental component led to the generation of a phase-weighted magnitude of cyclic variation.[35, 36, 40, 41, 54] This reported variable is calculated by multiplying the magnitude of cyclic variation by a weight term, such that "normal" phases have a weight of +1, and as the phase becomes either greater than or less than normal the phase weight transitions to -1.

Consequences of Multiple Methods

As the discussion above indicates, there are a number of methods for quantifying the magnitude of the cyclic variation of backscatter from myocardium. As a result, the valid concern is that the same heart, studied by groups using different methods of analysis, might exhibit a "different" magnitude of cyclic variation depending upon the method used. The literature indicates that the average value of the magnitude of cyclic variation of backscatter in normal hearts studies, in the same location, and in the same echocardiographic view has been reported to be a low as 5 dB [34, 68, 73] and as high as 9 dB.[32, 66] This discrepancy is addressed in Chapter 5.

Underlying Cause of Cyclic Variation

The mechanisms that are responsible for the observed change in the backscattered power from myocardium over the heart cycle are incompletely understood. There have been several investigations designed to determine the effects of proposed mechanisms and physical models that would lead to the cyclic changes in the scattering properties of the myocardium.[31, 55, 71] In Chapter 6 the simultaneous investigation of the cyclic variation of backscatter and of diastolic function using a parametrized diastolic filling formalism is presented to determine those aspects of cyclic variation that are related to cardiac diastole.

References

1. Beyer, R.T., *The parameter B/A*, in *Nonlinear Acoustics*, M.F. Hamilton and D.T. Blackstock, Editors. 1998, Academic Press: San Diego, CA. p. 25-40.
2. Bjorno, L. and P.A. Lewin, *Measurement of Nonlinear Acoustic Parameters in Tissue*, in *Tissue Characterization With Ultrasound*, J.F. Greenleaf, Editor. 1986, CRC Press, Inc.: Boca Raton, Florida. p. 141-163.
3. Blackstock, D.T., M.F. Hamilton, and A.D. Pierce, *Progressive Waves in Lossless and Lossy Fluids*, in *Nonlinear Acoustics*, M.F. Hamilton and D.T. Blackstock, Editors. 1998, Academic Press: San Diego, CA. p. 65-150.
4. Breazeale, M.A., *Finite-Amplitude Waves in Solids*, in *Handbook of Acoustics*, M.J. Crocker, Editor. 1998, J. Wiley: New York. p. 211-219.
5. Kinsler, L.E., A.R. Frey, A.B. Coppens, and J.V. Sanders, *Fundamentals of Acoustics, 4th ed.* 2000, New York: John Wiley and Sons, Inc. 179-184.
6. Wallace, K.D., Ph.D. thesis, Washington University in Saint Louis (2001).
7. Wallace, K.D., M.R. Holland, B.S. Robinson, R.J. Fedewa, C.W. Lloyd, and J.G. Miller, Impact of Propagation Through an Aberrating Medium on the Linear Effective Apodization of a Nonlinearly Generated Second Harmonic Field. IEEE Transactions on Ultrasonics, Ferroelectrics and Frequency Control 2006;53(7):1260-1269.
8. Kourtiche, D. and et al., Harmonic propagation of finite-amplitude sound beams: second harmonic imaging in ultrasonic reflection tomography. Measurement Science and Technology 2004;15(1):21.

9. Saito, S., A. Yamamoto, and K. Nakamura, B/A Measurement for Liquid Media Using an LN Transducer with Inverted-Domain Layer. Japanese Journal of Applied Physics 2005;44:4431-4435.

10. Fujii, Y., N. Taniguchi, I. Akiyama, J.-W. Tsao, and K. Itoh, A new system for in vivo assessment of the degree of nonlinear generation using the second harmonic component in echo signals. Ultrasound in Medicine and Biology 2004;30(11):1511-1516.

11. Akiyama, I., *Reflection mode measurement of nonlinearity parameter B/A*, in *Nonlinear Acoustics At the Turn of the Millennium*, W. Lauterborn and T. Kutz, Editors. 2000, Elsevier: London. p. 321-324.

12. Thuras, A.L., R.T. Jenkins, and H.T. O'Neil, Extraneous Frequencies Generated in Air Carrying Intense Sound Waves. The Journal of the Acoustical Society of America 1935;6(3):173-180.

13. Chavrier, F., C. Lafon, A. Birer, C. Barriere, X. Jacob, and D. Cathignol, Determination of the nonlinear parameter by propagating and modeling finite amplitude plane waves. The Journal of the Acoustical Society of America 2006;119(5):2639-2644.

14. Bjorno, L., Characterization of biological media by means of their non-linearity. Ultrasonics 1986;24:254-9.

15. Law, W.K., L.A. Frizzell, and F. Dunn, Ultrasonic determination of the nonlinearity parameter B/A for biological media. Journal of the Acoustical Society of America 1981;69:1210-12.

16. Law, W.K., L.A. Frizzell, and F. Dunn, Determination of the nonlinearity parameter B/A of biological media. Ultrasound in Medicine and Biology 1985;11:307-18.

17. Wallace, K.D., C.W. Lloyd, M.R. Holland, and J.G. Miller, Finite Amplitude Measurements of the Nonlinear Parameter B/A for Liquid Mixtures Spanning a Range Relevant to Tissue Harmonic Mode. Ultrasound in Medicine & Biology 2007;33(4):620-629.

18. Shklovskaya-Kordi, V.V., An acoustic method of determining the internal pressure in a liquid. Soviet Physics - Acoustics 1963;9:82-85.

19. Saito, S., Measurement of the Nonlinearity Parameter in Dispersive Liquid using Focused Ultrasound. Japanese Journal of Applied Physics 1998;37:3035-3040.

20. Matar, O.B., M. Vila, and F.V. Meulen. *Experimental and numerical study of the insert-substitution method: application to the measurement of the nonlinear parameter β of solids*. in *Ultrasonics Symposium, 2001 IEEE*. 2001, 709-712 vol.1.

21. Gong, X.-F., Z.-M. Zhu, T. Shi, and J.-H. Huang, Determination of the acoustic nonlinearity parameter in biological media using FAIS and ITD methods. Journal of the Acoustical Society of America 1989;86:1-5.

22. Gong, X.-F., F. Ruo, Z. Cheng-ya, and S. Tao, Ultrasonic investigation of the nonlinearity parameter B/A in biological media. Journal of the Acoustical Society of America 1984;76:949-50.

23. Dong, F., E. Madsen, M. MacDonald, and J. Zagzebski, Nonlinearity parameter for tissue-mimicking materials. Ultrasound in Medicine and Biology 1999;25:831-838.

24. Harris, G.R., Y. Liu, S. Maruvada, and P.M. Gammell. *P4H-1 Finite Amplitude Method for Measurement of Nonlinearity Parameter B/A Using Plane-Wave Tone Bursts*. in *Ultrasonics Symposium, 2007. IEEE*. 28-31 Oct. 2007, 2072-2074.

25. Wu, J. and J. Tong, Measurements of the nonlinearity parameter B/A of contrast agents. Ultrasound in Medicine and Biology 1998;24:153-9.

26. Saito, S., Measurement of the acoustic nonlinearity parameter in liquid media using focused ultrasound. Journal of the Acoustical Society of America 1993;93:162-72.

27. Sehgal, C.M., B.R. Porter, and J.F. Greenleaf, Ultrasonic nonlinear parameters and sound speed of alcohol-water mixtures. Journal of the Acoustical Society of America 1986;79:566-570.

28. Ichida, N., T. Sato, H. Miwa, and K. Murakami, Real-Time Nonlinear Parameter Tomography Using Impulsive Pumping Waves. Sonics and Ultrasonics, IEEE Transactions on 1984;31(6):635-641.

29. Madaras, E.I., B. Barzilai, J.E. Perez, B.E. Sobel, and J.G. Miller, Changes in myocardial backscatter throughout the cardiac cycle. Ultrasonic Imaging 1983;5(3):229-39.

30. Barzilai, B., E.I. Madaras, B.E. Sobel, J.G. Miller, and J.E. Perez, Effects of myocardial contraction on ultrasonic backscatter before and after ischemia. Am J Physiol 1984;247(3 Pt 2):H478-83.

31. Micari, A., M. Pascotto, A.R. Jayaweera, J. Sklenar, N.C. Goodman, and S. Kaul, Cyclic variation in ultrasonic myocardial integrated backscatter is due to phasic changes in the number of patent myocardial microvessels. J Ultrasound Med 2006;25(8):1009-19.

32. Iliceto, S., L. Galiuto, P. Colonna, V.F. Napoli, and P. Rizzon, Effects of atrial pacing stress test on ultrasonic integrated backscatter cyclic variations in normal subjects and in patients with coronary artery disease. Eur Heart J 1997;18(10):1590-8.

33. Hu, X., J. Wang, Y. Sun, X. Jiang, B. Sun, H. Fu, et al., Relation of ultrasonic tissue characterization with integrated backscatter to contractile reserve in patients with chronic coronary artery disease. Clin Cardiol 2003;26(10):485-8.

34. Milunski, M.R., G.A. Mohr, J.E. Perez, Z. Vered, K.A. Wear, C.J. Gessler, et al., Ultrasonic tissue characterization with integrated backscatter. Acute myocardial ischemia, reperfusion, and stunned myocardium in patients. Circulation 1989;80(3):491-503.

35. Vitale, D.F., R.O. Bonow, G. Gerundo, N. Pelaggi, G. Lauria, D. Leosco, et al., Alterations in ultrasonic backscatter during exercise-induced myocardial ischemia in humans. Circulation 1995;92(6):1452-7.

36. Wickline, S.A., L.J. Thomas, 3rd, J.G. Miller, B.E. Sobel, and J.E. Perez, Sensitive detection of the effects of reperfusion on myocardium by ultrasonic tissue characterization with integrated backscatter. Circulation 1986;74(2):389-400.

37. Ohara, Y., Y. Hiasa, S. Hosokawa, N. Suzuki, T. Takahashi, K. Kishi, et al., Ultrasonic tissue characterization predicts left ventricular remodeling in patients with acute anterior myocardial infarction after primary coronary angioplasty. J Am Soc Echocardiogr 2005;18(6):638-43.

38. Hancock, J.E., J.C. Cooke, D.T. Chin, and M.J. Monaghan, Determination of successful reperfusion after thrombolysis for acute myocardial infarction: a noninvasive method using ultrasonic tissue characterization that can be applied clinically. Circulation 2002;105(2):157-61.

39. Vandenberg, B.F., J.E. Stuhlmuller, L. Rath, R.E. Kerber, S.M. Collins, H.E. Melton, et al., Diagnosis of recent myocardial infarction with quantitative backscatter imaging: preliminary studies. J Am Soc Echocardiogr 1991;4(1):10-8.

40. Iwakura, K., H. Ito, S. Kawano, A. Okamura, K. Asano, T. Kuroda, et al., Detection of TIMI-3 flow before mechanical reperfusion with ultrasonic tissue characterization in patients with anterior wall acute myocardial infarction. Circulation 2003;107(25):3159-64.

41. Takiuchi, S., H. Ito, K. Iwakura, Y. Taniyama, N. Nishikawa, T. Masuyama, et al., Ultrasonic tissue characterization predicts myocardial viability in early stage of reperfused acute myocardial infarction. Circulation 1998;97(4):356-62.

42. Yuda, S., L. Short, R. Leano, and T.H. Marwick, Myocardial abnormalities in hypertensive patients with normal and abnormal left ventricular filling: a study of ultrasound tissue characterization and strain. Clin Sci (Lond) 2002;103(3):283-93.

43. Masuyama, T., F.G. St Goar, T.L. Tye, G. Oppenheim, I. Schnittger, and R.L. Popp, Ultrasonic tissue characterization of human hypertrophied hearts in vivo

with cardiac cycle-dependent variation in integrated backscatter. Circulation 1989;80(4):925-34.

44. Di Bello, V., R. Pedrinelli, A. Bertini, D. Giorgi, E. Talini, G. Dell'Omo, et al., Cyclic variation of the myocardial integrated backscatter signal in hypertensive cardiopathy: a preliminary study. Coron Artery Dis 2001;12(4):267-75.

45. Di Bello, V., D. Giorgi, E. Talini, G. Dell' Omo, C. Palagi, M.F. Romano, et al., Incremental value of ultrasonic tissue characterization (backscatter) in the evaluation of left ventricular myocardial structure and mechanics in essential arterial hypertension. Circulation 2003;107(1):74-80.

46. Losi, M.A., S. Betocchi, M. Chinali, G. Barbati, G. D'Alessandro, A. Cacace, et al., Myocardial texture in hypertrophic cardiomyopathy. J Am Soc Echocardiogr 2007;20(11):1253-9.

47. Vered, Z., B. Barzilai, G.A. Mohr, L.J. Thomas, 3rd, R. Genton, B.E. Sobel, et al., Quantitative ultrasonic tissue characterization with real-time integrated backscatter imaging in normal human subjects and in patients with dilated cardiomyopathy. Circulation 1987;76(5):1067-73.

48. Holland, M.R., A.A. Gibson, L.R. Peterson, M. Areces, J.E. Schaffer, J.E. Perez, et al., Measurements of the cyclic variation of myocardial backscatter from two-dimensional echocardiographic images as an approach for characterizing diabetic cardiomyopathy. J Cardiometab Syndr 2006;1(2):149-52.

49. Yuda, S., L. Short, R. Leano, and T.H. Marwick, Abnormal left ventricular filling with increasing age reflects abnormal myocardial characteristics independent of ischemia or hypertrophy. Am J Cardiol 2003;91(1):63-7.

50. Naito, J., T. Masuyama, T. Mano, K. Yamamoto, Y. Doi, H. Kondo, et al., Influence of preload, afterload, and contractility on myocardial ultrasonic tissue characterization with integrated backscatter. Ultrasound Med Biol 1996;22(3):305-12.

51. Bouki, K.P., A. Lange, P. Palka, C.M. Moran, L.N. Fenn, R.A. Wright, et al., Regional variations of ultrasonic integrated backscatter in normal and myopathicleft ventricles. A new multi-view approach. European Heart Journal 1996;17(11):1747-1755.

52. Yuda, S., J. Dart, O. Najos, and T.H. Marwick, Use of cyclic variation of integrated backscatter to assess contractile reserve and myocardial viability in chronic ischemic left ventricular dysfunction. Echocardiography 2002;19(4):279-87.

53. Wickline, S.A., L.J. Thomas, 3rd, J.G. Miller, B.E. Sobel, and J.E. Perez, The dependence of myocardial ultrasonic integrated backscatter on contractile performance. Circulation 1985;72(1):183-92.

54. Komuro, K., S. Yamada, T. Mikami, K. Yoshinaga, K. Noriyasu, K. Goto, et al., Sensitive detection of myocardial viability in chronic coronary artery disease by ultrasonic integrated backscatter analysis. J Am Soc Echocardiogr 2005;18(1):26-31.

55. Wickline, S.A., L.J. Thomas, 3rd, J.G. Miller, B.E. Sobel, and J.E. Perez, A relationship between ultrasonic integrated backscatter and myocardial contractile function. J Clin Invest 1985;76(6):2151-60.

56. Mottley, J.G., R.M. Glueck, J.E. Perez, B.E. Sobel, and J.G. Miller, Regional differences in the cyclic variation of myocardial backscatter that parallel regional differences in contractile performance. J Acoust Soc Am 1984;76(6):1617-23.

57. Yildirim, N., E. Saricam, C. Ozbakir, S. Bozboga, and A. Ocal, Assessment of the relationship between functional capacity and right ventricular ultrasound tissue characterization by integrated backscatter in patients with isolated mitral stenosis. Int Heart J 2007;48(1):87-96.

58. Di Bello, V., D. Giorgi, P. Viacava, T. Enrica, C. Nardi, C. Palagi, et al., Severe aortic stenosis and myocardial function: diagnostic and prognostic usefulness of ultrasonic integrated backscatter analysis. Circulation 2004;110(7):849-55.

59. Perez, J.E., J.B. McGill, J.V. Santiago, K.B. Schechtman, A.D. Waggoner, J.G. Miller, et al., Abnormal myocardial acoustic properties in diabetic patients and their correlation with the severity of disease. J Am Coll Cardiol 1992;19(6):1154-62.

60. Wagner, R.F., K.A. Wear, J.E. Perez, J.B. McGill, K.B. Schechtman, and J.G. Miller, Quantitative assessment of myocardial ultrasound tissue characterization through receiver operating characteristic analysis of Bayesian classifiers. J Am Coll Cardiol 1995;25(7):1706-11.

61. Di Bello, V., F. Santini, A. Di Cori, A. Pucci, E. Talini, C. Palagi, et al., Effects of bariatric surgery on early myocardial alterations in adult severely obese subjects. Cardiology 2008;109(4):241-8.

62. Fijalkowski, M., A. Koprowski, M. Gruchala, R. Galaska, A. Debska-Slizien, J. Rogowski, et al., Effect of preload reduction by hemodialysis on myocardial

ultrasonic characterization, left atrial volume, and Doppler tissue imaging in patients with end-stage renal disease. J Am Soc Echocardiogr 2006;19(11):1359-64.

63. Giglio, V., V. Pasceri, L. Messano, F. Mangiola, L. Pasquini, A. Dello Russo, et al., Ultrasound tissue characterization detects preclinical myocardial structural changes in children affected by Duchenne muscular dystrophy. J Am Coll Cardiol 2003;42(2):309-16.

64. Di Bello, V., F. Monzani, D. Giorgi, A. Bertini, N. Caraccio, G. Valenti, et al., Ultrasonic myocardial textural analysis in subclinical hypothyroidism. Journal of the American Society of Echocardiography 2000;13(9):832-840.

65. Fabrizio, A.-L., D.B. Vitantonio, T. Enrica, D.C. Andrea, M. Fabio, A. Lucia, et al., Early textural and functional alterations of left ventricular myocardium in mild hypothyroidism. Eur J Endocrinol 2006;155(1):3-9.

66. D'Hooge, J., B. Bijnens, F. Jamal, C. Pislaru, S. Pislaru, J. Thoen, et al., High frame rate myocardial integrated backscatter. Does this change our understanding of this acoustic parameter? Eur J Echocardiogr 2000;1(1):32-41.

67. Mobley, J., C.E. Banta, H.M. Gussak, J.E. Perez, and J.G. Miller, Clinical Tissue Characterization: Online Determination of Magnitude and Time Delay Myocardial Backscatter. Video Journal of Echocardiography 1995;5(2):40-48.

68. Finch-Johnston, A.E., H.M. Gussak, J. Mobley, M.R. Holland, O. Petrovic, J.E. Perez, et al., Dependence of "apparent" magnitude on the time delay of cyclic variation of myocardial backscatter. Ultrasound Med Biol 1999;25(5):759-62.

69. Vandenberg, B.F., L. Rath, T.A. Shoup, R.E. Kerber, S.M. Collins, and D.J. Skorton, Cyclic variation of ultrasound backscatter in normal myocardium is view dependent: clinical studies with a real-time backscatter imaging system. J Am Soc Echocardiogr 1989;2(5):308-14.

70. Mohr, G.A., Z. Vered, B. Barzilai, J.E. Perez, B.E. Sobel, and J.G. Miller, Automated determination of the magnitude and time delay ("phase") of the cardiac cycle dependent variation of myocardial ultrasonic integrated backscatter. Ultrasonic Imaging 1989;11(4):245-59.

71. Holland, M.R., K.D. Wallace, and J.G. Miller, Potential relationships among myocardial stiffness, the measured level of myocardial backscatter ("image brightness"), and the magnitude of the systematic variation of backscatter (cyclic variation) over the heart cycle. J Am Soc Echocardiogr 2004;17(11):1131-7.

72. Holland, M.R., A.A. Gibson, C.A. Kirschner, D. Hicks, A. Ludomirsky, and G.K. Singh, Intrinsic myoarchitectural differences between the left and right ventricles of fetal human hearts: an ultrasonic backscatter feasibility study. J Am Soc Echocardiogr 2009;22(2):170-6.

73. Finch-Johnston, A.E., H.M. Gussak, J. Mobley, M.R. Holland, O. Petrovic, J.E. Perez, et al., Cyclic variation of integrated backscatter: dependence of time delay on the echocardiographic view used and the myocardial segment analyzed. J Am Soc Echocardiogr 2000;13(1):9-17.

74. Thomas, L.J., S.A. Wickline, J.E. Perez, B.E. Sobel, and J.G. Miller, A real-time integrated backscatter measurement system for quantitative cardiac tissue characterization. IEEE Trans Ultrason Ferroelectr Freq Control 1986;33(1):27-32.

Chapter 2: A Plane Wave Source With Minimal Harmonic Distortion For Investigating Nonlinear Acoustic Properties[†]

List of Parameters used in this Chapter:

β - coefficient of nonlinearity

c_0 - speed of sound of the material

D - diameter of a source transducer

f - frequency of the ultrasonic signal

λ - wavelength of the ultrasonic signal

ω_0 - angular frequency of the ultrasonic signal

p_0 - pressure of the ultrasonic signal

ρ_0 - mass density of a material

$\bar{x}$ - shock formation distance

Introduction

In previously published ultrasonic experiments designed to measure the intrinsic nonlinear parameter, β, interpretation of the measured data was frequently simplified by approximating the insonifying ultrasonic field as a plane wave over the region of interaction with the sample under investigation.[1-12] A number of methods to realize this approximation have been utilized and, in general, rely on careful positioning of the

[†] Material for this chapter comes from a published manuscript: Lloyd, CW, Wallace, KD, Holland, MR, and Miller, JG, Plane wave source with minimal harmonic distortion for investigating nonlinear acoustic properties. J. Acoust. Soc. Am. 2007;122:91-96.

sample in a region of the ultrasonic field where the diffraction pattern can be approximated as planar, such as the extreme near field,[1, 2] the natural focus,[3-5] or the far field.[6] Estimates of the nonlinear parameter can be determined from finite amplitude measurements of the level of harmonic distortion in the ultrasonic signal after propagation through either a series of thicknesses of a sample[1, 2] or a single sample.[3-12]

One method that has been used successfully in our Laboratory is to affix a stainless-steel delay line to a transmitting transducer such that the output field from the delay line satisfies a plane wave approximation.[3, 4] An advantage with this approach is that the high sound velocity in the stainless-steel (approximately four times faster than in water) permits the ultrasonic beam to satisfy the plane wave approximation in a relatively short distance, rather than after traveling a relatively long (possibly prohibitively long) path. Furthermore, this method reduces the generation of undesired harmonic distortion arising from propagation to the sample under investigation, as propagation within the stainless steel delay line results in only a negligible amount of finite amplitude distortion, eliminating the need for physical attenuators in the propagation path.[6]

In the current investigation, scanned hydrophone pseudo-array measurements and numerical simulations were used to investigate the applicability of a plane wave approximation for an ultrasonic pulse emanating from a stainless-steel delay line and to assess the amount of harmonic distortion generated from propagation in the delay line. Hydrophone measurements of the ultrasonic field in water were conducted in a meridian plane and compared with the results from simulations of the diffracting finite amplitude field associated with a 12.7 mm diameter contact transducer propagating either a 7 MHz or a 4 MHz tone burst through a 46.4 mm steel delay line and 25.0 mm of water.

Methods

Experimental Setup

The delay line used in this experiment was machined from an 88.9 mm diameter cylinder of type 304 stainless-steel. The faces of the cylinder were machined flat and parallel, and polished smooth, producing a delay line of 46.4 mm in length as measured by Vernier calipers. A 12.7 mm diameter, broadband, 10 MHz center frequency contact transducer (Panametrics V111, Waltham, MA) was bonded to one face of the stainless-steel cylinder using a thin, uniform layer of vacuum grease and held in contact with a plastic (Delrin™) fixture, as illustrated in Figure 2-1. This created a watertight seal and enabled the contact transducer-delay line assembly to be submerged into a water tank for hydrophone characterization of the transmitted ultrasonic field.

The first ultrasonic frequency (7 MHz) used in this investigation was chosen such that the ultrasonic beam's diffraction pattern would be entering the natural focus as the pulse exited the delay line apparatus. This frequency was determined using the formula for the near field distance, given by

$$\text{Near Field Distance} = \frac{D^2}{4\lambda}\left[1-\left(\frac{\lambda}{D}\right)^2\right], \tag{2-1}$$

where D is the diameter of the source transducer and $\lambda = c_0 / f$ is the ultrasonic wavelength.[13] The speed of sound in the stainless-steel, c_0, was experimentally determined to be 5.73 mm/μs using a contact transducer in a pulse echo mode to measure the round-trip time of flight inside the stainless-steel delay line. To position the natural focus of the ultrasonic field just after emerging from the stainless-steel delay line, as

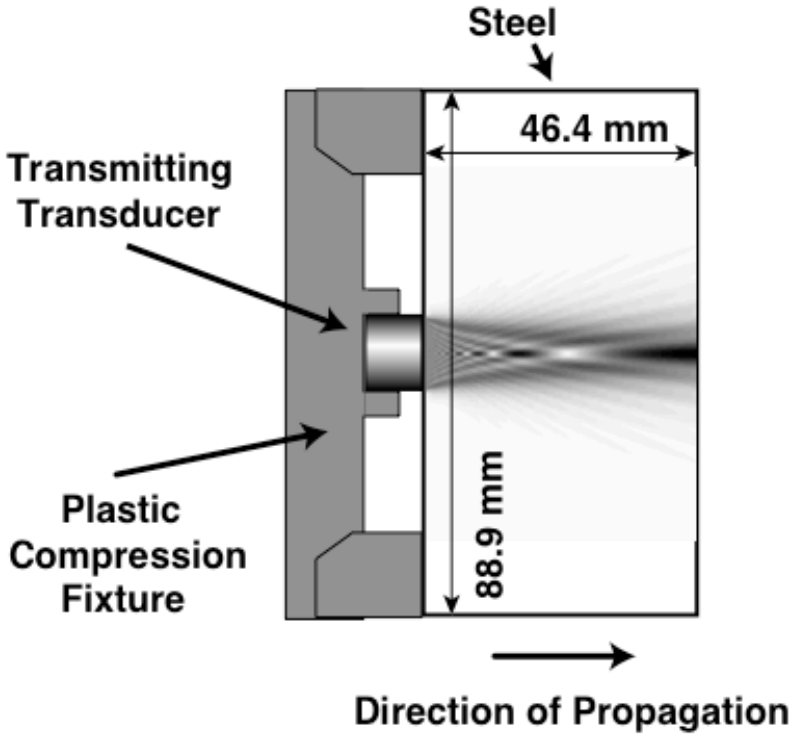

Figure 2-1: Diagram of the stainless-steel delay line apparatus. The transducer is a 12.7 mm diameter contact transducer, held in place with a plastic fixture to the face of the steel cylinder. Simulation of the 7 MHz fundamental (1f) field component is shown inside the delay line.

defined by equation 2-1, a center frequency of 7.0 MHz was chosen for the narrowband transmitted signal. For this study, the transmit transducer was driven with a 4.0 μs duration tone burst gated from a 7.0 MHz continuous-wave signal oscillator (Hewlett-Packard 606B, Palo Alto, CA) and amplified with a 50 dB amplifier (ENI 240L, Rochester, NY). The gating was accomplished with a pulse generator (Hewlett-Packard 8112A) in conjunction with two mixer/modulators in series (Hewlett-Packard 33125).

In addition, a lower frequency, 4 MHz, was chosen to test the applicability of this specific delay line for making measurements within the focal zone to far field transition regime of the ultrasonic field. In this case, a 12.7 mm diameter, broadband, 5 MHz

center frequency contact transducer (Panametrics V109) was utilized. The transducer was driven by a 4.0 μs tone burst at 4.0 MHz from a function generator (Hewlett-Packard 8116A) in conjunction with a 50 dB radiofrequency amplifier (ENI 240L) and a passive 6.4 MHz low pass filter.

Measurements of the Ultrasonic Field

To characterize the ultrasonic pressure field of the system, the transducer and delay line were positioned in a water tank with the ultrasonic beam aligned along the *X*-axis of a motion control system (Aerotech Unidex 511, Pittsburgh, PA). The temperature of the water was monitored using a thermistor (Omega OL-710, Stamford, CT) connected to a thermometer (Omega 5831A). The temperature of the water tank was maintained at 23.8°C ± 0.1°C and 21.5°C ± 0.5°C during the measurements of the 7 MHz and 4 MHz signals, respectively. A membrane hydrophone (Sonic Industries, Model 804, now Sonora Medical Systems, Longmont, CO) was scanned in a rectangular, 81 by 57 pseudo-array using a uniform step size of 0.25 mm (20 mm by 14 mm total grid size) to map out the ultrasonic field in the meridian *(X-Y)* plane. The hydrophone calibration was performed by the manufacturer, using a reference hydrophone that had been calibrated at the National Physical Laboratory in the United Kingdom. The resulting radiofrequency signals output from the hydrophone preamplifier were digitized with an eight-bit resolution oscilloscope (Tek 2440, Beaverton, OR for the 7.0 MHz acquisitions, and a Tektronix 5052B for the 4.0 MHz acquisitions). Data could be acquired with the membrane hydrophone positioned as close as 4.0 mm to the face of the steel cylinder while avoiding reverberations between the steel cylinder and the hydrophone. The

received waveforms were signal averaged in the time domain to improve the signal-to-noise ratio for data acquired for both the 7.0 MHz and 4.0 MHz systems. The values of the acoustic pressure at the fundamental and harmonic frequencies were determined by determining the voltage amplitude of each spectral component of the signal averaged waveform and referring to the pressure-voltage calibration data provided by the hydrophone manufacturer.

Simulations

Simulations were carried out using a Burgers' equation enhanced angular spectrum approach.[14-16] This approach permits the modeling of the propagation and the harmonic distortion of a diffracting ultrasonic signal as it propagates through the different propagation media (steel and water). Simulations were performed for the two fundamental frequencies employed experimentally (4 MHz and 7 MHz). Effects of attenuation were taken to be negligible for both the steel and water at these frequencies. The nonlinear parameter β was taken to be 3.5 for both water and stainless-steel. (A literature search for similar metals yielded values for β ranging from 2 to 4.5 and thus the nonlinear parameter for stainless-steel was taken to be 3.5 for this simulation).[17]

The predictions from simulation for the normalized particle velocity amplitudes of the 7 MHz fundamental (*1f*) component are depicted in Figure 2-2 (a). A grayscale image of the magnitude for the meridian plane slice is shown in the top panel and the profile corresponding to the values of the field on the beam axis is shown in the bottom panel. As depicted in Figure 2-2 (a), the beam is propagating from left to right, first

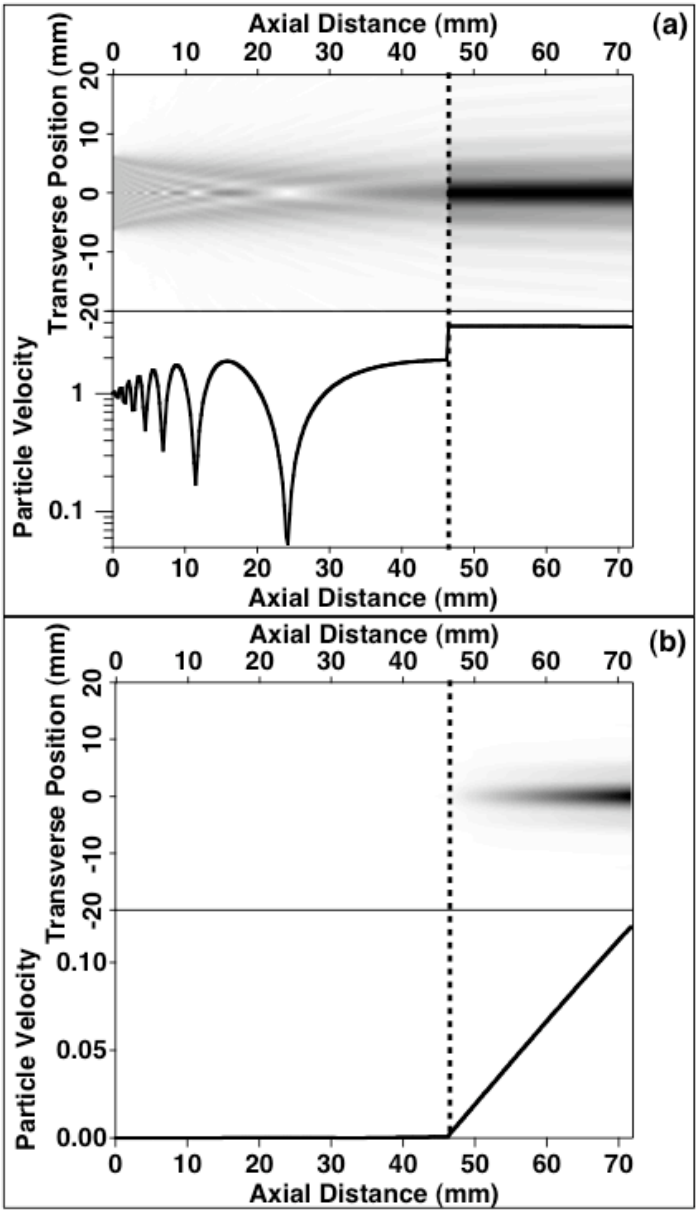

Figure 2-2: Simulation of the diffraction pattern through a 304-stainless steel delay line into lossless water medium, for (a) the 7 MHz fundamental component, and (b) the 14 MHz second harmonic. The top portion of each figure component illustrates the magnitude of the meridian plane slice of the field (black is the maximum amplitude and white is zero). The bottom portion of each component shows the amplitude along the propagation axis of the beam. The phase velocity used in the simulation corresponds to measured values of 5.73 mm/μs in steel and 1.48 mm/μs in water. The particle velocity amplitudes are normalized to that of the fundamental component at zero axial distance.

through the stainless steel delay line and then through 25 mm of water. The vertical dashed line indicates the boundary between steel and water. Similarly, the nonlinearly generated 14 MHz second harmonic (*2f*) component of the particle velocity obtained from simulation is displayed in Figure 2-2 (b). In both cases, the pressure has been normalized to the initial fundamental pressure at the face of the transducer.

Figure 2-3 presents the corresponding results for the 4 MHz simulation. For both simulations the second harmonic amplitude along the propagation axis is observed to grow linearly as a function of propagation distance in the water region. This is consistent with the second order (weakly nonlinear) approximate form of the Fubini solution.[18]

Experimental Results and Comparisons

7 MHz Study

Figure 2-4 shows the measured amplitudes of the 7 MHz fundamental *(1f)* and 14 MHz harmonic *(2f)* components in the meridian plane pseudo-array scan for the identical waterpath region shown in the simulations presented in Figure 2-2 (a) and (b). The grayscale is normalized in each image such that black represents the maximum amplitude and white is zero. Because one goal of this work is to produce a valid approximation to a plane wave over an experimentally useful area, the size of a 3 mm diameter receiving transducer is represented by hash marks on the right hand side of each of the four images in Figure 2-4.

Figure 2-5 (a) illustrates the power along the axis of propagation as a function of distance for each of the four panels in Figure 2-4. The curves represent the measured power relative to the fundamental at the left edge of the plot (axial distance of 50 mm).

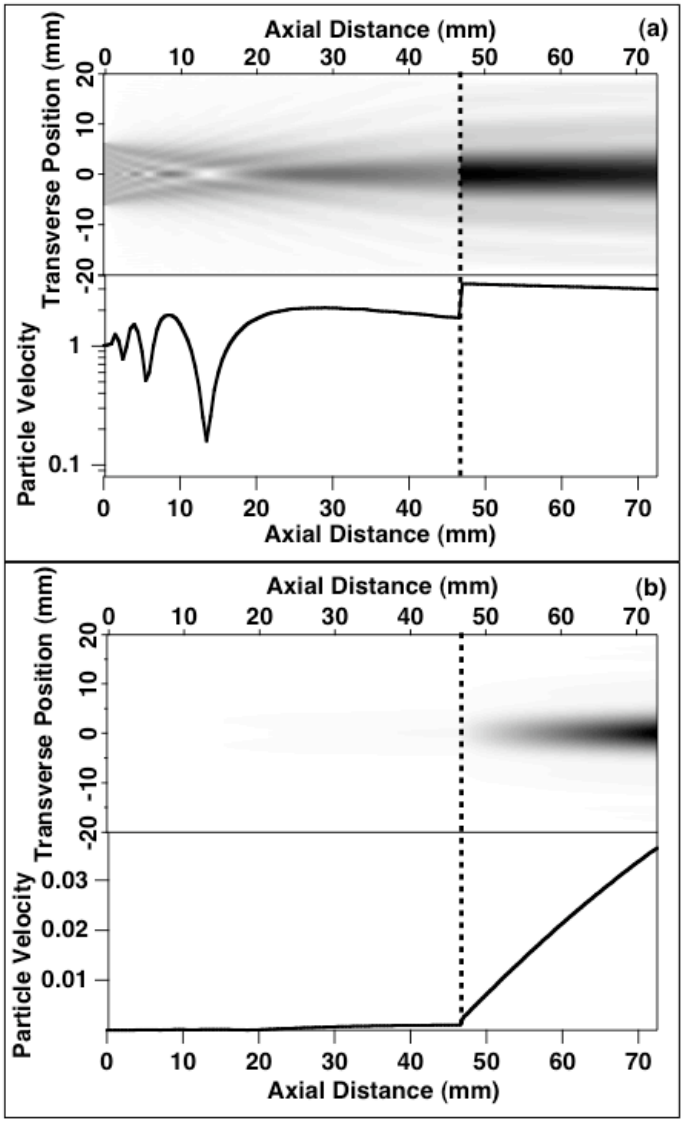

Figure 2-3: Simulation of the diffraction pattern through a 304-stainless steel delay line into lossless water medium, for (a) the 4 MHz fundamental component, and (b) the 8 MHz second harmonic, in a manner analogous to Figure 2-2.

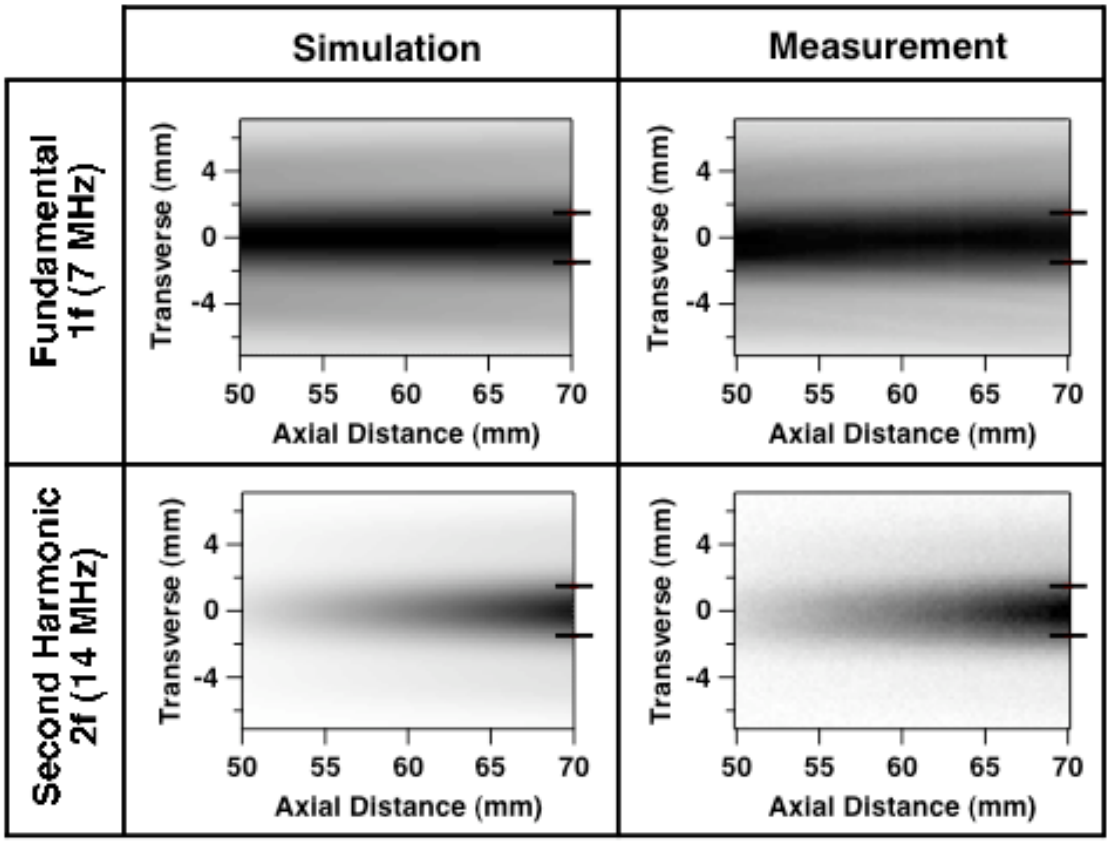

Figure 2-4: Comparison of expected beam pattern from simulation (left) with hydrophone measurement of the field (right) in a meridian plane beginning 4 mm beyond the steel-water interface, for a 7 MHz fundamental signal. The separation between the hash marks on the right side of each graph corresponds to the 3 mm diameter of a receiving transducer.

The measured pressure values for the fundamental and second harmonic at an axial distance of 70 mm were 53.2 kPa and 2.2 kPa, respectively. Figure 2-5 (b) illustrates the predicted and measured transverse profiles of the power in the fundamental frequency at an axial distance of 70 mm. Figure 2-5 (c) shows this comparison for the second harmonic portion of the signal.

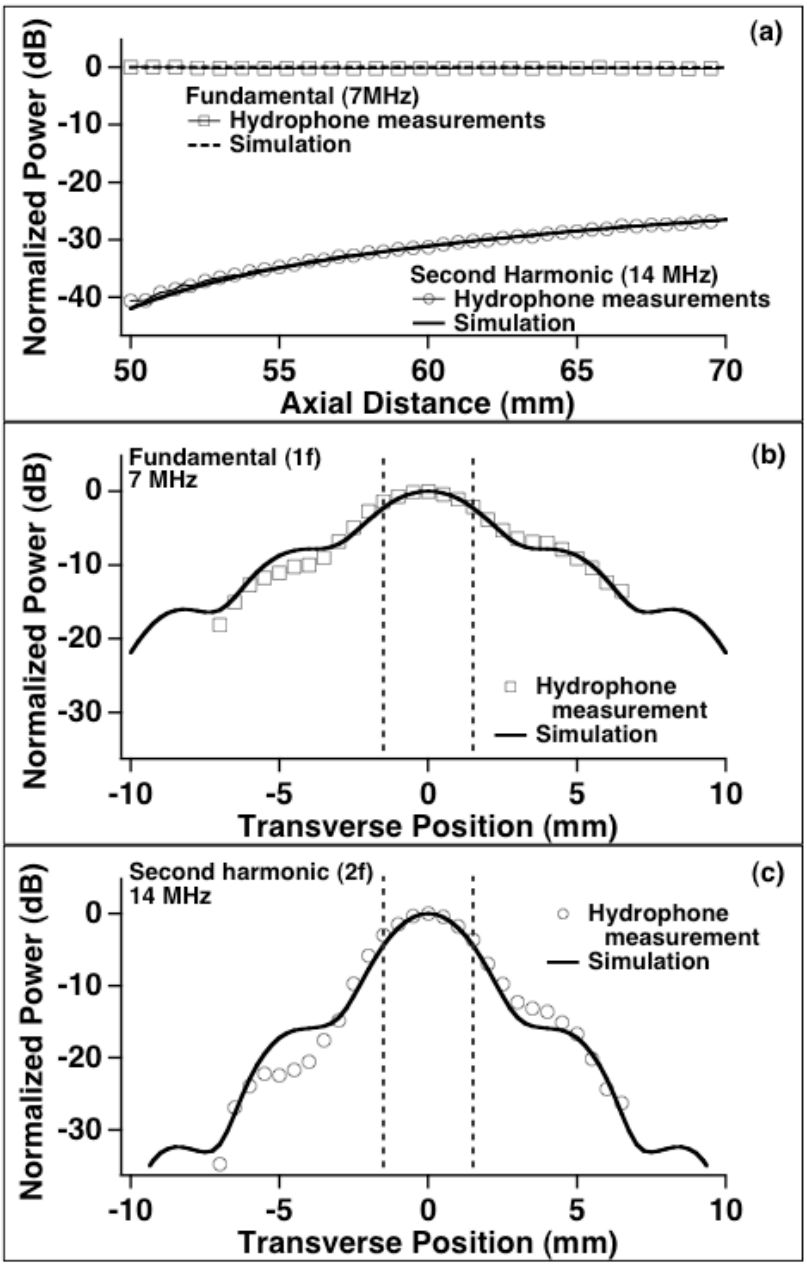

Figure 2-5: (a) Comparison of hydrophone measurements and simulation results, for both the fundamental and second harmonic, in the axial direction. (b) The normalized transverse profile for the 7 MHz fundamental, 70 mm away from a 12.7 mm diameter piston source, propagating through 46.4 mm of stainless steel and 23.7 mm of water. (c) Normalized transverse profile of the second harmonic amplitude at the same location as (b).

4 MHz Study

Figure 2-6 shows the measured amplitudes of the 4 MHz fundamental (1*f*) and the 8 MHz second harmonic (2*f*) components of the transmitted ultrasonic beam in the meridian plane. These are displayed along with the simulation results of Figure 2-3 (a) and (b). For each panel, the image is normalized so that black represents the maximum amplitude and white represents zero. Again, hash marks are present on the right side of each panel to indicate the receiving size of a 3 mm diameter transducer.

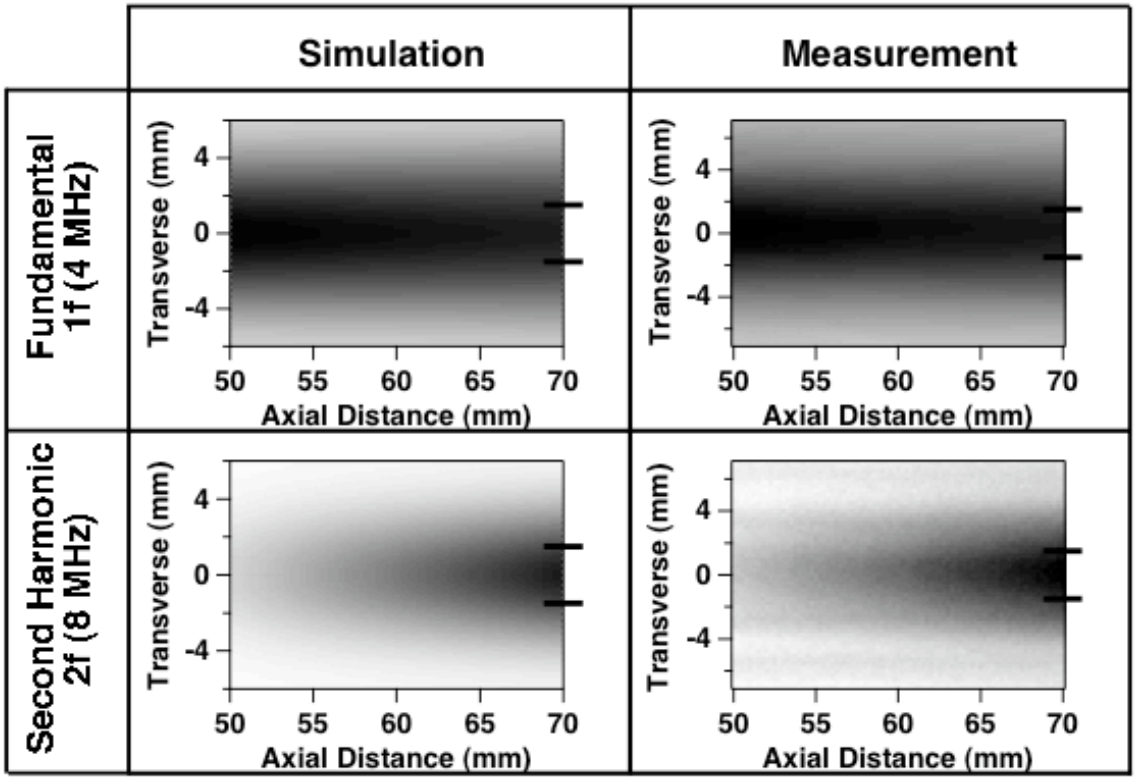

Figure 2-6: Comparison of expected beam pattern from simulation (left) with hydrophone measurement of the field (right) in a meridian plane beginning 4 mm beyond the steel-water interface, for a 4 MHz fundamental signal. The separation between the hash marks on the right side of each graph corresponds to the 3 mm diameter of a receiving transducer.

Figure 2-7 shows orthogonal one-dimensional slices of the measured and simulated ultrasonic beams detailed in Figure 2-6. In Figure 2-7 (a), the power along the axis of propagation is shown as a function of axial distance for each of the four panels found in Figure 2-6. Each curve is normalized to the measured power of the fundamental at the left edge of the plot, which is at 50 mm from the source transducer. The values of the pressure for the fundamental and second harmonic were measured at a distance of 70 mm from the transducer, and were 23.6 kPa and 228 Pa, respectively. Figure 2-7 (b) and (c) illustrates a comparison of the simulation with the measured results for a transverse profile taken at an axial distance of 70 mm for the fundamental and second harmonic, respectively.

Discussion

Overall, good agreement is observed between the measured and simulated cross sections of the ultrasonic fields. For the 7 MHz case, the measured magnitude and features of the transverse cross sections for the fundamental (*1f*) component appear to be relatively constant over the 20 mm range of axial propagation distances investigated. This agrees with the simulation (Figure 2-2), where the amplitude of the 7 MHz fundamental is observed to vary by only 0.13 dB along the axis in the region of the water filled sample chamber. The hydrophone measurements of the on-axis power, for both the fundamental (7 MHz) and second harmonic (14 MHz) components, are in good agreement with predictions from the simulation, as can be seen from Figure 2-5 (a). Figure 2-5 (b) and (c) indicate that the field varies by less than 3 dB for the fundamental and less than 6 dB for the second harmonic across a 3 mm diameter. The relatively good

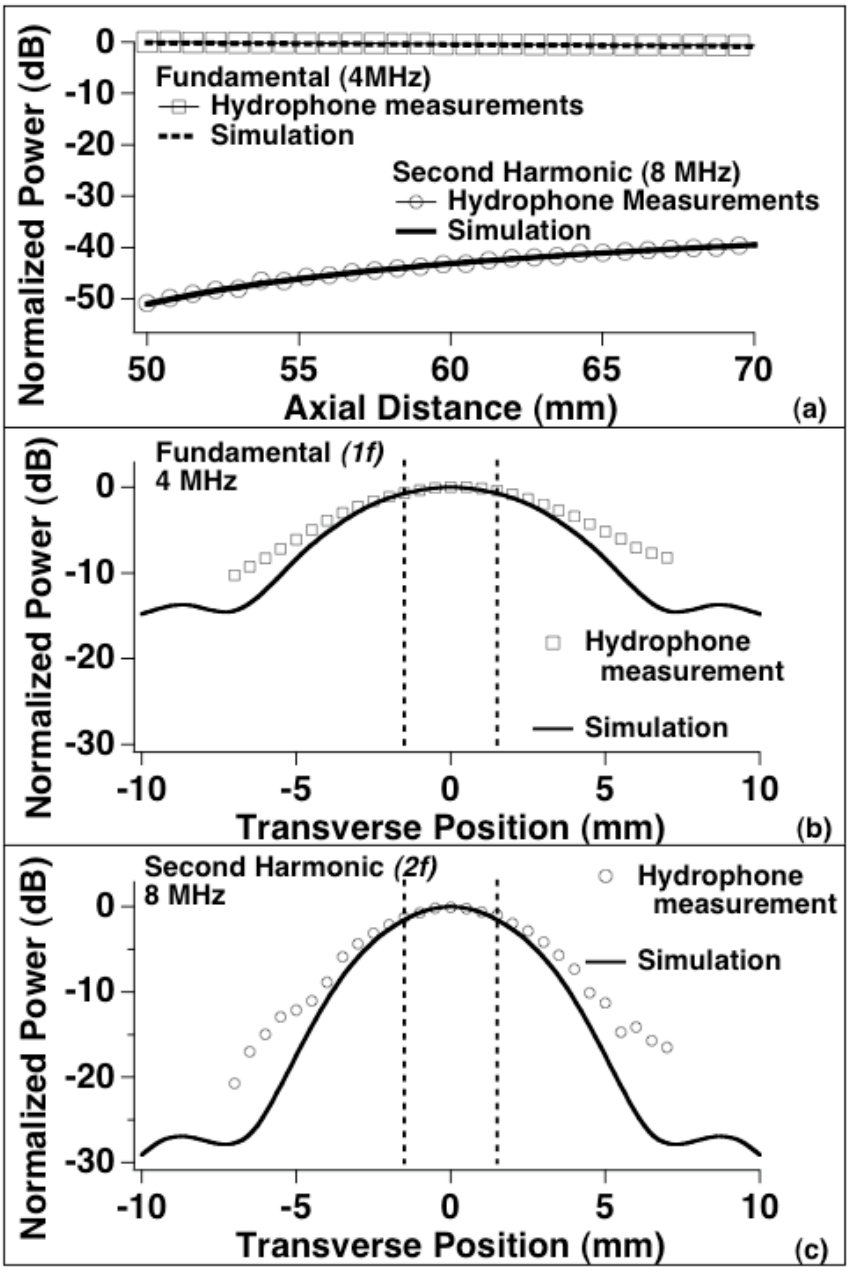

Figure 2-7: (a) Comparison of hydrophone measurements and simulation results, for both the fundamental and second harmonic, in the axial direction. (b) The normalized transverse profile for the 4 MHz fundamental, 70 mm away from a 12.7 mm diameter piston source, propagating through 46.4 mm of stainless steel and 23.6 mm of water. (c) Normalized transverse profile of the second harmonic amplitude at the same location as (b).

agreement between the experimental measurements and predictions from the simulation support the validity of a plane wave approximation to the field.

Transmission of a narrowband 4 MHz signal yielded similar results. The fundamental component of the signal remains relatively constant across the measured range of axial propagation. As seen in Figure 2-3, the amplitude of the fundamental component decreases by only 0.9 dB over the 20 mm axial range of the figure. Examination of Figure 2-7 (b) and (c) indicates that the ultrasonic power varies by less than 0.75 dB for the fundamental and less than 1.5 dB for the second harmonic across the 3 mm diameter that is marked by the vertical dashed lines. In comparison with the 7 MHz case, where the 3 dB width of the ultrasonic beam was only 3 mm, the 3 dB width for the 4 MHz case has increased to over 6 mm. This indicates a wider region over which a plane wave approximation is valid.

There is, however, a drawback to using the far field region of the ultrasonic beam to generate a wider plane wave region. Due to the nature of the far field, the ultrasonic amplitude of the fundamental signal will not be as large as what is found in the focal zone, so there will be a correspondingly lower rate of harmonic generation. In comparison with the 7 MHz study illustrated in Figures 2-2 and 2-3, the final amplitude after 25 mm of propagation in water is smaller for the 4 MHz case, although in both cases the initial harmonic is negligible. Additionally, the nonlinear generation of the second harmonic is linearly dependent upon the frequency in the weakly nonlinear regime, and thus using a lower frequency reduces the rate of generation of the second harmonic distortion.[11] The decrease in the signal–to-noise ratio for the second harmonic can be seen in Figure 2-6, with a less well-confined and weaker main lobe. Nevertheless the far field

approach does allow for a certain amount of flexibility because an experiment can be adjusted to give a plane wave over the field depth needed for propagation through a sample while maintaining the necessary signal to noise ratio needed for measuring the harmonic distortion of a pulse.

An additional benefit of the delay line lies in the lack of nonlinear generation within the steel, compared to propagation in water. To understand this, consider the shock formation distance for plane wave propagation, which represents the propagation distance required to form a complete shock wave, neglecting the effects of attenuation:

$$\bar{x} = \frac{\rho_0 c_0^3}{\beta \omega_0 p_0} \tag{2-2}$$

where ρ_0 is the density, c_0 is the sound speed, β is the coefficient of nonlinearity of the medium, and ω_0 and p_0 are the angular frequency and pressure of the incident pulse, respectively. The density of steel is roughly eight times that of water, and the sound velocity is about four times that of water. The nonlinear parameters of steel and water are approximately the same, as discussed earlier. Thus, calculation of the ratio of shock formation distances for steel and water reveals that the shock formation distance in steel is much larger than that for water. Therefore, the relative amount of nonlinear distortion is significantly less in steel. In addition, propagation to a given portion of the diffraction field in steel is accomplished in one-quarter the propagation distance in water; nonlinear generation is reduced further by this reduction in path length. Thus, the distortion in a typical length delay line is negligible compared to the distortion in the same diffractive region in a water path. This is illustrated in both Figure 2-2 and 2-3, which indicate that the simulations predict that the ultrasonic signal has virtually no amplitude in the second

harmonic while the fundamental propagates through the steel. This is also affirmed in the experimental work, in which a very small amount of distortion is measured in the signal when measured as close to the face of the delay line as possible. For the 7 MHz study, the measured amplitude in the second harmonic was 40 dB down from the amplitude in the fundamental signal, and for the 4 MHz study this difference increased to 50 dB.

The use of this delay line apparatus has other practical advantages. One primary benefit is that the absence of transmitted harmonics obviates the need to employ physical means of attenuation to reduce unwanted harmonic signals. The introduction of such materials, such as attenuating media and quarter-wave plates, can cause signal loss in the fundamental frequency.[6, 19] Another benefit of the delay line is that it can be used in other types of nonlinearity experiments. If the whole assembly is oriented vertically and a chamber wall for containing fluid samples is attached, measurements of the nonlinearity parameter based on a pullback approach can be performed.[1-4] Such a setup benefits from the plane waves generated as well as the lack of transmitted harmonics, but permits the receiving transducer to be manually translated in the fluid medium of interest.[4]

In summary, a method of physically generating approximate plane waves has been examined. The validity of the approximation of a plane wave source has been studied with both simulation and physical measurements using a point-like receiver, for two transmitted frequencies. Over a narrow lateral range but a substantial axial range, this approximation appears to be valid. The use of the delay line method as illustrated above seems to be appropriate for further studies involving the measurement of the coefficient of nonlinearity of materials of interest.

References

1. Law, W.K., L.A. Frizzell, and F. Dunn, Ultrasonic determination of the nonlinearity parameter B/A for biological media. Journal of the Acoustical Society of America 1981;69:1210-12.
2. Law, W.K., L.A. Frizzell, and F. Dunn, Determination of the nonlinearity parameter B/A of biological media. Ultrasound in Medicine and Biology 1985;11:307-18.
3. Wallace, K.D., M.R. Holland, and J.G. Miller, Novel approach for overcoming effects of diffraction in measurements of the nonlinear B/A parameter in liquidlike media. The Journal of the Acoustical Society of America 2004;116(4):2566.
4. Wallace, K.D., C.W. Lloyd, M.R. Holland, and J.G. Miller, Finite Amplitude Measurements of the Nonlinear Parameter B/A for Liquid Mixtures Spanning a Range Relevant to Tissue Harmonic Mode. Ultrasound in Medicine and Biology 2006;(in press).
5. Germain, L., R. Jacques, and J.D. Cheeke, Acoustic microscopy applied to nonlinear characterization of biological media. Journal of the Acoustical Society of America 1989;86:1560-5.
6. Dong, F., E. Madsen, M. MacDonald, and J. Zagzebski, Nonlinearity parameter for tissue-mimicking materials. Ultrasound in Medicine and Biology 1999;25:831-838.
7. Bjorno, L., Characterization of biological media by means of their non-linearity. Ultrasonics 1986;24:254-9.

8. Gong, X.-F., F. Ruo, Z. Cheng-ya, and S. Tao, Ultrasonic investigation of the nonlinearity parameter B/A in biological media. Journal of the Acoustical Society of America 1984;76:949-50.

9. Gong, X.-F., Z.-M. Zhu, T. Shi, and J.-H. Huang, Determination of the acoustic nonlinearity parameter in biological media using FAIS and ITD methods. Journal of the Acoustical Society of America 1989;86:1-5.

10. Saito, S., A. Yamamoto, and K. Nakamura, B/A Measurement for Liquid Media Using an LN Transducer with Inverted-Domain Layer. Japanese Journal of Applied Physics 2005;44:4431-4435.

11. Shklovskaya-Kordi, V.V., An acoustic method of determining the internal pressure in a liquid. Soviet Physics - Acoustics 1963;9:82-85.

12. Wu, J. and J. Tong, Measurements of the nonlinearity parameter B/A of contrast agents. Ultrasound in Medicine and Biology 1998;24:153-9.

13. Kinsler, L.E., A.R. Frey, A.B. Coppens, and J.V. Sanders, *Fundamentals of Acoustics, 4th ed.* 2000, New York: John Wiley and Sons, Inc. 179-184.

14. Fedewa, R.J., K.D. Wallace, M.R. Holland, J.R. Jago, G.C. Ng, M.R. Rielly, et al. *Effect of Changing the Transmit Aperture on the Spatial Coherence of Backscatter for the Nonlinearly Generated Second Harmonic*. in *Proc. IEEE Ultrasonics Symposium*. October 2002, Munich, Germany, 1624-1627.

15. Christopher, P.T. and K.J. Parker, New approaches to nonlinear diffractive field propagation. Journal of the Acoustical Society of America 1991;90:488-499.

16. Vecchio, C.J. and P.A. Lewin, Finite Amplitude Acoustic Propagation Modeling Using the Extended Angular Spectrum Method. Journal of the Acoustical Society of America 1994;95(5):2399-2408.

17. Breazeale, M.A., *Finite-Amplitude Waves in Solids*, in *Handbook of Acoustics*, M.J. Crocker, Editor. 1998, J. Wiley: New York. p. 211-219.

18. Blackstock, D.T., M.F. Hamilton, and A.D. Pierce, *Progressive Waves in Lossless and Lossy Fluids*, in *Nonlinear Acoustics*, M.F. Hamilton and D.T. Blackstock, Editors. 1998, Academic Press: San Diego, CA. p. 65-150.

19. Wallace, K.D., Ph.D. thesis, Washington University in Saint Louis (2001).

Chapter 3: Exploring a Through-Transmission Approach For the Measurement of the Nonlinear Parameter of Materials

List of Parameters used in this Chapter:

$\alpha(f)$ - attenuation coefficient of the material at a given frequency

$\frac{B}{A}$ - nonlinear parameter of the material

c - small-signal speed of sound of the material

d - thickness of a sample

D' - amplitude transmission coefficient, from a sample to the reference material

D'' - amplitude transmission coefficient, from the reference to a sample material

f - frequency of the ultrasonic signal

h - a lumped local nonlinear parameter

I - a lumped exponential attenuation term

L - total path length of a through-transmission experiment

λ - wavelength of the ultrasonic signal

p - pressure of the ultrasonic signal (subscripted to indicate a fundamental (1) or second harmonic (2) pressure)

ρ - mass density of a material

T^I - pressure intensity transmission coefficient

$V(f)$ - received voltage amplitude spectrum

x - position along the central axis of a transmitting transducer

$\bar{x}$ - shock formation distance in a material

Introduction

In Chapter 2, a method of generating approximately planar ultrasonic waves was validated for two different frequencies, in order to determine the range of validity for the plane wave approximation utilized in several different types of measurements. For example, the apparatus described therein was used in a pullback experiment to determine the nonlinear parameter in liquids. This type of experiment has already been discussed in detail by Wallace.[1, 2] There are, however, other methods of measurement that utilize the delay line method to generate planar waves. The measurement method that is of current interest for this Chapter is that of an insert-substitution method. In this method, a pressure measurement is obtained for two scenarios, one where the ultrasonic signal propagates only through a reference material, and one where a sample of fixed thickness is interposed in the propagation path.

The purpose of this Chapter is two-fold. As a consequence of an unfortunate typographical error, the published description of the aforementioned insert-substitution method is described in the literature in a way that is incorrect.[3] The first portion of this chapter will be devoted to the detailed derivation of the underlying formulae required for the correct measurement of the nonlinear parameter. After this has been established, the second portion of the Chapter will be used to convey the results of using this method (and some variations therein) to measure the nonlinear parameter of two specific liquids, ethylene glycol and isopropanol (or 2-propanol).

Derivation of the nonlinear parameter in a substitution experiment

A proper derivation of the insert-substitution methods will facilitate the measurement of the nonlinear parameter in sample materials that can be insonified using a through-transmission measurement. The derivation contained here can be traced through a progression of work by Gong *et. al.*,[4] which introduced the finite amplitude insert substitution (FAIS) method, and the work of Dong *et. al.*,[3] which produced the simplified finite amplitude insert substitution (SFAIS) method. One distinction between the present work and the methods to be discussed is that the generation of ultrasonic plane waves in the current experiment can be done using the steel delay line method from Chapter 2 as an alternative to the assumed transmission over large distances. For all of these methods, the experimental conditions needed to justify the assumptions in the theory are that the sample is interrogated with a beam that has no harmonic distortion at some origin point in the field, and that the field looks like a plane wave over the fixed region used for the propagation of the ultrasonic signal and the concomitant nonlinear distortion of that field. The latter condition can potentially be relaxed if the theoretical derivations include a treatment of the diffraction of the ultrasonic beam as this beam propagates through the experiment.

The derivation for these experiments starts with the work from Gong *et. al.*,[4] which is limited to media whose attenuation coefficients increase linearly with frequency. This limitation, which is stated in the original publication, might be an unnecessary limitation used to facilitate a solution to the driving equation. This theoretical derivation of the nonlinear buildup of the second harmonic component of the ultrasonic field eventually leads to a formula for the nonlinear parameter in the sample, expressed

relative to the nonlinear parameter in a host material (such as a sample in a water tank immersion experiment). This derivation is based on a well-known formula (attributable to Shklovskaya-Kordi[5]) that describes the generation of the second harmonic based on several factors,

$$p_2(x) = \left(\frac{B}{A} + 2\right) \cdot p_1^2 \frac{\pi f}{2\rho_0 c_0^3} \cdot x \tag{3-1}$$

This formula describes the buildup of the second harmonic pressure p_2, in terms of contributing factors (but does not include effects arising from diffraction or attenuation). The parameter (B/A) is the nonlinear parameter. The frequency f, the propagation distance x (from some initial plane, x=0), the fundamental pressure p_1, the fluid density ρ, and the speed of sound c are all parameters that influence how much harmonic pressure has been generated. Note that in this form, the buildup of the second harmonic pressure is explicitly a linear function of distance, as well as a squared function of the generating fundamental pressure. Since equation 3-1 is a generalization that assumes negligible loss, the underlying ordinary differential equation (ODE) needs to be solved in the presence of attenuation. The ODE governing this process is

$$\frac{dp_2(x)}{dx} = p_1^2(x) \cdot h(x) - p_2(x) \cdot \alpha(2f, x) \tag{3-2}$$

where the parameter h(x),

$$h(x) = \left(\frac{B}{A} + 2\right) \cdot \frac{\pi f}{2\rho c^3} \tag{3-3}$$

is a (more convenient) local lumped nonlinear parameter. Both the attenuation α and this nonlinear parameter h are listed with spatial dependence, as a reminder that this can (and should) be derived rigorously with spatial dependences. The immediate derivational

issue will be integrals that don't neatly collapse. Additionally, the attenuation coefficient is listed with a frequency dependence, and is usually denoted as the attenuation coefficient for either the fundamental (1f) or second harmonic (2f) frequency. The solution of equation 3-2 can be found using the method of an integrating factor,

$$\frac{dp_2(x)}{dx}e^{\int_0^x \alpha(2f,x')dx'} + p_2(x)\cdot\alpha(2f,x)e^{\int_0^x \alpha(2f,x')dx'} = p_1^2(x)\cdot h(x)e^{\int_0^x \alpha(2f,x')dx'} \tag{3-4}$$

The formalism can be simplified by considering regions that are homogeneous, so that the attenuation coefficients and the lumped nonlinear parameters do not have a continuous spatial dependence,

$$\frac{dp_2(x)}{dx}e^{\alpha(2f)x} + p_2(x)\cdot\alpha(2f)e^{\alpha(2f)x} = p_1^2(x)\cdot h\cdot e^{\alpha(2f)x} \tag{3-5}$$

$$\frac{d}{dx}\left(p_2(x)\cdot e^{\alpha(2f)x}\right) = p_1^2(x)\cdot h\cdot e^{\alpha(2f)x} \tag{3-6}$$

The region boundaries between the sample and the reference materials are a special case to be handled later. If the fundamental pressure has only an attenuation component of dependence (and no diffractive component along the axis of propagation), then the form of the fundamental pressure has the form of an amplitude modified by an exponential term representing the attenuation loss,

$$p_1(x) = p_1(0)e^{-\alpha(1f)x} \tag{3-7}$$

$$\frac{d}{dx}\left(p_2(x)\cdot e^{\alpha(2f)x}\right) = \left(p_1^2(0)e^{-2\alpha(1f)x}\right)\cdot h\cdot e^{\alpha(2f)x} \tag{3-8}$$

This equation can then integrated exactly with respect to x and solved for the second harmonic pressure,

$$p_2(x)\cdot e^{\alpha(2f)x} - p_2(0) = p_1^2(0)\cdot h\cdot \int_{x'=0}^{x} e^{\left(\alpha(2f)-2\alpha(1f)\right)x'}\,dx' \tag{3-9}$$

$$p_2(x)\cdot e^{\alpha(2f)x} - p_2(0) = p_1^2(0)\cdot h\cdot \left(\frac{e^{\left(\alpha(2f)-2\alpha(1f)\right)x} - 1}{\alpha(2f)-2\alpha(1f)} \right) \tag{3-10}$$

$$p_2(x) = p_2(0)e^{-\alpha(2f)x} + p_1^2(0)\cdot h\cdot \left(\frac{e^{-2\alpha(1f)x} - e^{-\alpha(2f)x}}{\alpha(2f)-2\alpha(1f)} \right) \tag{3-11}$$

There are two terms present in this expression for the second harmonic pressure. The leading term represents the harmonic pressure located at a source plane (x=0), and is a reminder that any initial harmonic pressure present must be properly accounted for when measuring the harmonic pressure at some distance from the source plane. This is an important distinction to remember for the derivation of the SFAIS method, but in a simple measurement using the weakly nonlinear model, this pressure merely attenuates away exponentially. The second term is a modification of the Shklovskaya-Kordi equation (equation 3-1) where, instead of having a buildup of the nonlinear pressure proportional to the propagation distance x, this buildup is related to a more complicated function of the attenuation and the propagation distance. In the limit of negligible attenuation, the term in parentheses in equation 3-11 reduces to only the propagation distance x, because the exponentials can be approximated by their first two terms in the Taylor series for the exponential (i.e. 1 + (argument)). Additionally, in cases where the attenuation of the medium is non-negligible but rises linearly with frequency (i.e. $\alpha(2f) = 2 * \alpha(1f)$), the argument of the exponential in equation 3-9 goes to zero, and the integral evaluates to simply x. This simplifying case yields a term that is reminiscent of the

Shklovskaya-Kordi equation of nonlinear generation, but with an addition term dealing with the attenuation of the second harmonic,

$$p_2(x) = p_2(0)e^{-\alpha(2f)x} + p_1^2(0)\cdot h\cdot x\cdot e^{-\alpha(2f)x} \tag{3-12}$$

Equation 3-11 establishes the expected amount of harmonic pressure that is generated by a plane wave with finite (as opposed to infinitesimal) amplitude. One setup for an experiment to exploit this relationship is a substitution method that measures the generated harmonic pressure for two different experimental scenarios. This method, as stated above, uses the steel delay line method of Wallace *et. al.*[2] to produce a plane wave which is approximately free from any generated second harmonic signal after transmission into water. The two different experiments differ in what is present in the field following the delay line, as seen in Figure 3-1.

In one measurement, the only material present in the fixed distance L is water, and the measured harmonic pressure can be labeled as a reference harmonic pressure. With the assumption that the attenuation in water is small, and the approximation of a plane wave is satisfied, the harmonic pressure measured at a distance L from the delay line can be determined from equation 3-11 and the discussion that follows,

$$p_{2,O} = p_1^2(0)\cdot\left(\frac{B}{A}+2\right)_O\cdot\frac{\pi f}{2\rho_O c_O^3}\cdot L \tag{3-13}$$

The second measurement performed is on a sample of interest, of thickness d. Here, the total path length is still L, such that the plane wave passes first through a distance (L – d) composed of water, with known material parameters. The wave then is transmitted into the sample, with amplitude transmission coefficient D'', which is related to the material parameters of both the sample (using the subscript X) and the water (with the subscript

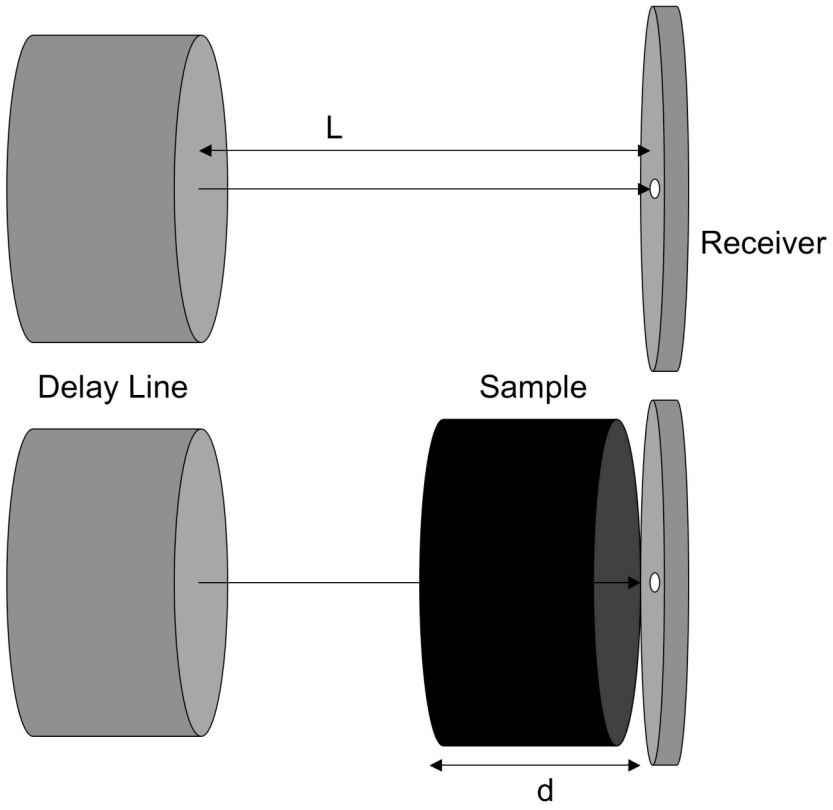

Figure 3-1: Two experimental configurations to determine the nonlinear parameter B/A for a sample. Above: an ultrasonic signal passes from a delay line through a water path to a receiving transducer after propagating a distance L. Below: the same signal passes through a sample of thickness d that displaces an equal thickness of water before being received.

O),

$$D'' = \frac{2 \cdot \rho_X c_X}{\rho_X c_X + \rho_O c_O} \tag{3-14}$$

Further harmonic pressure is generated as the wave propagates, governed by the sample material parameters (including the unknown parameter of interest B/A that is being measured). At the interface of the sample with the water, there is a further loss described by an amplitude transmission coefficient D',

$$D' = \frac{2 \cdot \rho_O c_O}{\rho_X c_X + \rho_O c_O} \tag{3-15}$$

After the transmission of the plane wave back into the reference material, the pressure is detected with a receiver placed as close as possible to the sample-reference interface, to minimize further harmonic pressure generation in the reference material.

Using equation 3-11, which illustrates that generated harmonic pressures attenuate away when passing through a material with non-zero attenuation, the measured pressure in this experiment can be expressed as

$$p_{2,X} = \left[\begin{array}{l} \left[p_1^2(0) \cdot \left(\frac{B}{A} + 2 \right)_O \cdot \frac{\pi f}{2\rho_O c_O^3} \cdot (L-d) \right] \cdot D'' e^{-\alpha(2f)d} \\ + p_1^2(0)(D'')^2 \cdot \left(\frac{B}{A} + 2 \right)_X \cdot \frac{\pi f}{2\rho_X c_X^3} \cdot \frac{e^{-2\alpha(f)d} - e^{-\alpha(2f)d}}{\alpha(2f) - 2\alpha(1f)} \end{array} \right] \cdot D' \qquad (3\text{-}16)$$

The grouping of terms in equation 3-16 is meant to aid in the identification of the origin of the particular terms. The first term consists of the generation of harmonic pressure through the water path, which is then transmitted into a sample (D'') and then attenuated, while the second term is the analogous generation of pressure in the sample, again using equation 3-11. Further, a transmission factor has to be applied (D') to the sum of these pressures at the sample-reference interface. A ratio of equations 3-16 to 3-13 can be determined, and by simplification of this ratio a working equation for the nonlinear parameter in the sample can be found,

$$\frac{p_{2,X}}{p_{2,O}} = \left(1 - \frac{d}{L} \right) \cdot D' D'' I_2^2 + \frac{D' D''^2}{L} \cdot \frac{\left(\frac{B}{A} + 2 \right)_X}{\left(\frac{B}{A} + 2 \right)_O} \cdot \frac{\rho_O c_O^3}{\rho_X c_X^3} \cdot \frac{I_1^2 - I_2^2}{\alpha(2f) - 2\alpha(1f)} \qquad (3\text{-}17)$$

where the attenuation terms have been condensed by substituting a lumped attenuation factor,

$$I_1 = \exp(-\alpha(1f)d) \qquad (3\text{-}18)$$

$$I_2 = \exp(-\frac{1}{2}\alpha(2f)d) \tag{3-19}$$

Equation 3-17 can be solved to find the ratio of the nonlinear parameters

$$\frac{\left(\frac{B}{A}+2\right)_X}{\left(\frac{B}{A}+2\right)_O} \cdot \frac{D'D''^2}{L} \cdot \frac{\rho_O c_O^3}{\rho_X c_X^3} \cdot \frac{I_1^2 - I_2^2}{\alpha(2f) - 2\alpha(1f)} = \frac{p_{2,X}}{p_{2,O}} - \left(1 - \frac{d}{L}\right) \cdot D'D''I_2^2 \tag{3-20}$$

$$\frac{\left(\frac{B}{A}+2\right)_X}{\left(\frac{B}{A}+2\right)_O} = \left[\frac{p_{2,X}}{p_{2,O}}\frac{L}{d} - \left(\frac{L}{d}-1\right)I_2^2 D'D''\right] \cdot \frac{\rho_X c_X^3}{\rho_O c_O^3} \frac{d}{D''^2 D'} \frac{2\alpha(1f) - \alpha(2f)}{I_2^2 - I_1^2} \tag{3-21}$$

The rearrangement presented in equation 3-21 is done to mirror equation 3-1 of Dong *et. al.*[3] Here it is important to note that in the manuscript by Dong, the exponential attenuation term for the second harmonic, I_2, is missing the factor of ½ that is seen in equation 3-19. The absence of this factor has been confirmed through private communication with Dr. Dong to be a printing error from the journal publishing process.[†]

Choices for the experimental configuration to measure the nonlinear parameter

The derivation leading to equation 3-21 is a valid method of determining the ratio of nonlinear parameters (isolated on the left side of the equality) for a specific set of experimental constraints. These constraints include: an axial distance (designated x=0 in the derivation) at which the nonlinear distortion of the ultrasonic signal is negligible, an approximate plane wave over the propagation length of the experiment, and an axially

[†] Excerpt from e-mail from Dr. Dong, dated April 9, 2007: "Hi, Chris, this is a print error. In my original script I submitted to UMB, the "1/2" was in the equation, but in the published paper, it was missing. I think I already sent a letter to the editor, tried to correct this one. But it may be delayed, somehow. […]"

homogeneous sample (such that the material parameters are not functions of depth in the sample, at a particular beam location in the sample). However, in the context of these approximations, there are a number of ways to configure the experimental setup to study the nonlinear parameter in a qualifying sample material, which usually hinges on the generation of a distortion-free plane wave at a location deep into the far field of the diffraction pattern of the generating transducer. In the study of this finite amplitude method, two such methods of generating this pressure have been utilized.

One method of accomplishing this pressure field was studied first by Dong *et. al*.[3] In that manuscript, the goal was to measure the ultrasonic parameters (including the nonlinear parameter) of both tissue-mimicking phantoms and reference materials, one of which was ethylene glycol (which was one of the materials studied in the present study). The setups for the two different measurements required for the determination of the nonlinear parameter are shown in Figure 3-2. This setup utilizes the far field of a transmitting transducer along with the insertion of a glycerol sample chamber. The far field of the transducer is realized by utilizing a very long path length for the 2.25 MHz ultrasonic signal (in their case, 48 cm). By comparison, the near field distance of the ½" diameter transducer employed,

$$\text{Near Field Distance} = \frac{D^2}{4\lambda}\left[1-\left(\frac{\lambda}{D}\right)^2\right] \sim \frac{D^2}{4\lambda} = \frac{D^2 f}{4c} \qquad (3\text{-}22)$$

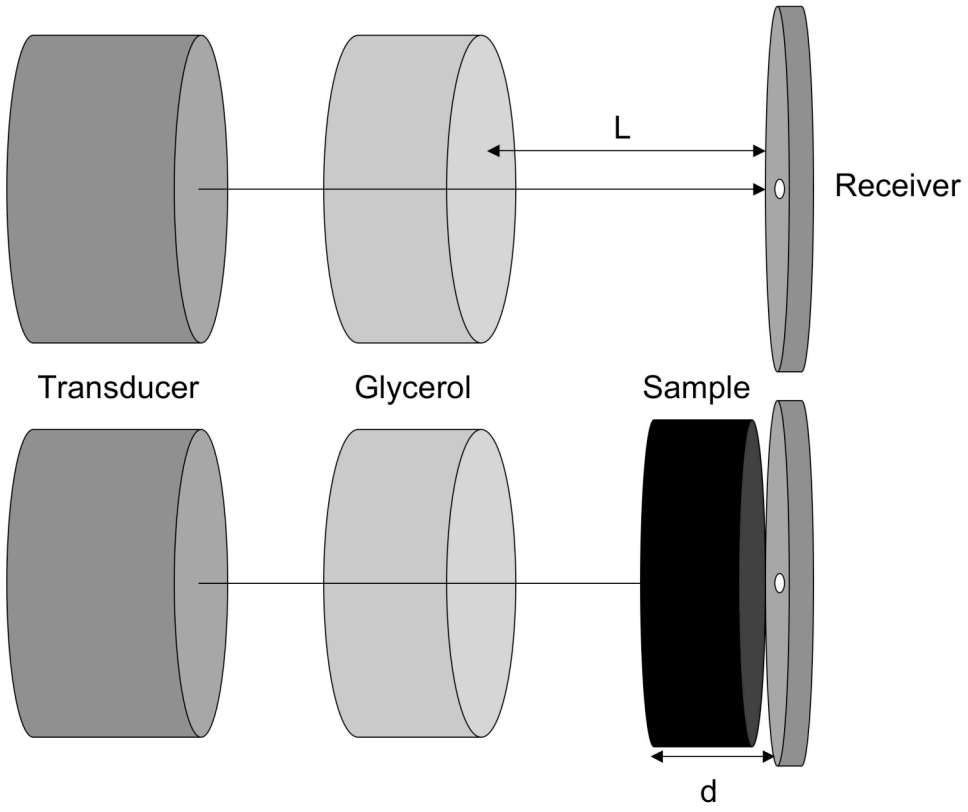

Figure 3-2: Two experimental configurations to determine the nonlinear parameter B/A for a sample. Above: A transmitting transducer propagates a signal through an attenuating chamber of glycerol before traveling a distance L in the reference material. Below: the same experiment as the reference measurement, but with the addition of a sample of thickness d displacing an equal thickness of reference material in front of the ultrasonic receiver.

is approximately 6 cm in this case. Thus 48 cm is well beyond the near field distance and the focal zone of the transducer. In this regard, note that the drawing of Figure 3-2 is not to scale. After propagation of the signal through this large distance, a glycerol chamber is introduced to attenuate the signal. The attenuation coefficient of glycerol exhibits a frequency-squared dependence. As a result, for a given amount of loss for the fundamental frequency signal, four times as much loss is incurred at the second harmonic frequency. The effect of this glycerol attenuator, then, is to remove the harmonic distortion in the propagating signal by causing preferentially greater loss at the higher frequencies.

An alternate method proposed for the measurement of the nonlinear parameter draws upon our laboratory's use of stainless steel delay lines to satisfy both of the approximations required for the validity of the theory presented above. As presented in Chapter 2, the effect that the steel delay line has on diffraction is to reduce the near field distance for a given frequency (as seen from equation 3-22), so that for a given distance in steel the ultrasonic signal will appear to have propagated farther than in the same distance in water. The use of stainless steel as a propagation medium also has an effect on the total nonlinear distortion in the ultrasonic signal. Again, consider the shock formation distance in a material,

$$\bar{x} = \frac{\rho_0 c_0^3}{\beta \omega_0 p_0} \tag{3-23}$$

where this distance represents the propagation length from an ultrasonic source at which a shock wave will form (for a lossless medium). Thus, this is a simplistic measure of the rapidity of nonlinear distortion in the medium, since a large shock formation distance implies that the level of distortion in the ultrasonic field is small at distances much less than this shock distance. The coefficient of nonlinearity for steel is not appreciably different from that of water, but the density and speed of sound are eight times and four times larger in steel than in water. For an ultrasonic signal of a given frequency and pressure, the shock formation distance is 512 times longer in steel than in water. So, the required propagation length to get to a given portion of the diffraction field is reduced with steel, and the nonlinear distortion that the signal incurs as it travels is negligible.

Upon transmission into water, the ultrasonic signal has propagated into the far field without a significant amount of distortion, which eliminates the need for a glycerol attenuation chamber. There is an insertion loss for the transmission of the ultrasonic

signal from the steel into water, which does attenuate the fundamental signal. However, it is possible to improve the transmission characteristics of the steel delay line through the use of matching layers. These matched layers provide an intermediary impedance level between the high impedance of steel and the relatively modest impedance of the water. Matching layers were not employed in the current study but remain an option for future use, should there exist a need for a stronger transmitted fundamental frequency signal in an experiment of this nature.

Further design factors in the experiment to measure the nonlinear parameter

Above and beyond the use of a delay line (as opposed to a long propagation path coupled with an attenuator), there are other factors, common to both of these designs, which require consideration for the implementation of the experiment. These include

- The design of a sample chamber, if one is required to contain the sample
- The measurement of the relevant ultrasonic parameters of the sample, and
- The characteristics of the ultrasonic pulse.

Each of these factors will be discussed to weigh the relevant issues therein. After these considerations are discussed, the results of the experiment will be discussed, especially against the backdrop of the previously discussed experimental factors.

Experimental chamber utilized for liquid samples

The specific samples used for this study were ethylene glycol (an organic liquid) and isopropanol (an alcohol). Because both of these liquids needed to be contained

within a water bath for this experiment, a sample chamber was utilized. To accomplish this, a chamber was constructed using the combination of Delrin plastic rings as well as Saran Wrap, as indicated in Figure 3-3. The rings have a large inner diameter (4") to permit the transmission of the ultrasonic beam (which has a much smaller footprint) without causing additional diffractive effects. The transmission of the signal passes through a three-material interface (water-Saran-sample), which requires the use of more complex transmission coefficients[6] or the use of a water-filled sample chamber during the "reference only" measurement to approximate the conditions under which the simpler coefficients are valid. These chambers are filled via a small sealable port in the side of the Delrin ring.

One drawback of this setup is that the transmission interface is constructed from a large, drawn sheet of Saran Wrap. The size of the transmission window, coupled with the flexibility of a plastic wrap, makes the local thickness of the sample liquid somewhat variable as a result of deflections of the Saran Wrap away from an optimally smooth position. This could affect the measurement of the material parameters of the sample via errors in an assumed thickness (discussed in more detail below), but could also affect measurements of the transmitted ultrasonic amplitude as a result of beam steering. Incident ultrasonic waves can be steered at an interface with a medium of different phase velocity that is not perpendicular to the propagating field. This refraction would steer the propagating ultrasonic signal in an unexpected direction, and the received pressure on the beam axis (where the maximum signal is expected) would be erroneously decreased as a result.

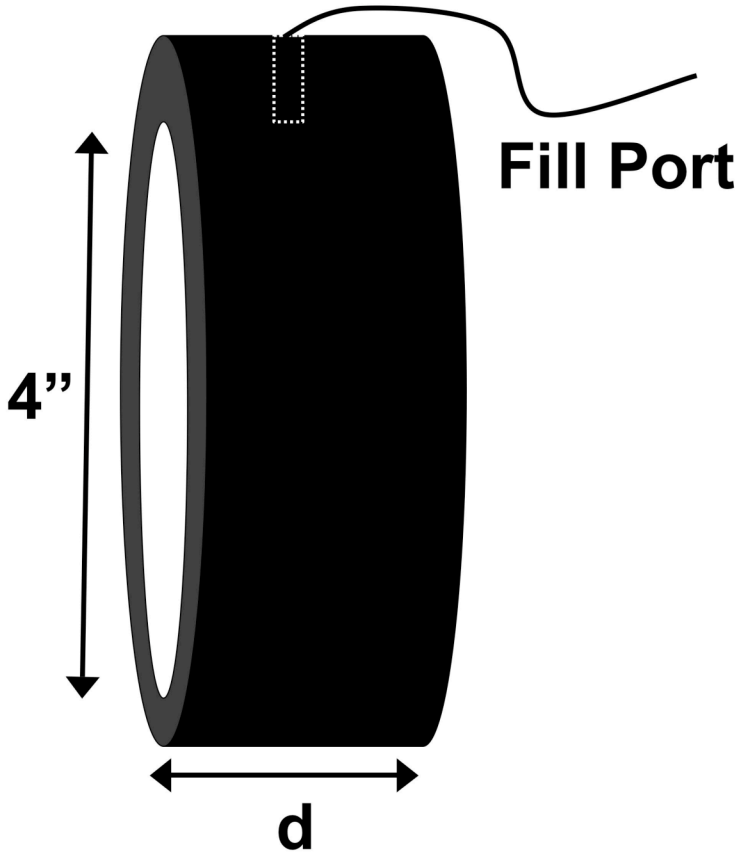

Figure 3-3: A basic representation of the sample chambers used in this experiment. Shown is the “donut” Delrin ring, of fixed inner diameter (4”) and thickness d. Not shown is the Saran Wrap that forms the rest of the chamber, which would extend over the interior diameter on both sides of the ring. This chamber is filled using a sealable fill port through the side of the Delrin ring.

The most noticeable cause of this deflection in the membranes of the sample chamber occurred due to the pressure of the sample liquid pushing outwards on the membrane (stretching it). One approach employed to counteract this stretching was to fill the sample chamber while the chamber was partially submerged in a small water bath. By gradually raising the water bath level to match the fluid level inside of the chamber, a pressure balance was maintained on the membranes. Further, because the total volume of the sample chambers was known by direct measurement of the cylinder dimensions, the total amount of sample fluid to insert into the chamber could be calculated to avoid over-

filling of the chamber. This amount of fluid was inserted using a graduated syringe, to ensure that the correct amount of sample material was utilized.

Measurement of material parameters of the sample

Before equation 3-21 can be applied to determine the nonlinear parameter of the sample liquid, several material parameters need to be determined. These parameters are

- The mass density of the sample and reference materials
- The thickness of the sample chamber
- The speed of sound of the sample and reference materials, and
- The attenuation of the sample and reference materials.

Values of these parameters are ultimately either directly inserted into equation 3-21 or necessary in the calculation of other parameters that are directly used (or both, in some cases). The accurate determination of these parameters is necessary for the subsequent accurate determination of the nonlinear parameter of the sample.

Some of these parameters were known *a priori* from literature searches and, while validated internally, did not differ from the reported values. The nonlinear parameter of the reference (water) was taken to be 5.2, for example.[7] The known mass densities of the three materials was: 1000 kg/m^3 for water, 1113.2 kg/m^3 for ethylene glycol[3], and 871 kg/m^3 for isopropanol.[8] Similarly, the velocity of sound in the reference was known by application of a known polynomial functional form[9] of the velocity as a function of temperature, using the temperature of the water tank provided by a thermistor system (Omega OL-710 and Omega 5831A, Stamford, CT). In the same way the attenuation

coefficient of water was calculated from a known function of temperature and frequency[10] although the attenuation can sometimes be neglected as a small correction.

For the remaining parameters, a direct measurement was necessary to ascertain their values. The first measurements performed were designed to measure the velocity of the sample and the thickness of the sample simultaneously.[11] This method (referred to as the Sollish method) has been thoroughly reviewed,[12] so the methodology is only briefly described here. Two measurements are performed in a pulse-echo arrangement: one with, and one without, the sample of interest interposed between the transmitting transducer and a reflecting surface. By measuring the time-of-flight for a transmitted ultrasonic signal to the boundaries present in the experiment, and by considering the resulting time-of-flight alterations due to the sample's presence, the thickness and speed of sound of the sample can be determined. This solution exists because there are two independent time-of-flight equations to consider for the two unknown parameters.

The measurement of the attenuation of the sample was performed using a through-transmission method[13] that has been discussed in detail.[12] In brief, this determination of the attenuation also makes use of two measurements, one with, and one without, a sample present between a transmitting and receiving transducer pair. The attenuation coefficient of the sample can be determined from the signal loss due to the sample through the equation

$$\alpha_s(f) - \alpha_h(f) = \frac{\ln(10)}{2d}\left[\log\left(\frac{\left|V_{ref}(f)\right|^2 T^I_{h\to s} T^I_{s\to h}}{\left|V_{samp}(f)\right|^2}\right)\right] \tag{3-24}$$

where h and s represent host (water) or sample parameters, T^I is the appropriate transmission coefficient from one material to another, d is the thickness of the sample,

and V(f) represent the received amplitude spectra for the reference-only and sample-present measurements. This experiment can be performed either with narrowband signals (such that the received amplitude spectra are essentially one frequency) or with a broadband signal (to look at both the fundamental and second harmonic frequencies with one experiment). Often the host attenuation can be negligible. However, it is explicitly treated here because the attenuation at 2.25 MHz for water ($1.22 * 10^{-3}$ cm^{-1}) is from 3 to 10 percent of the value for the sample liquids used. If the attenuation of water had been neglected, the true attenuation of the liquids would have been underestimated. The through-transmission measurement also is amenable to the correction for axial diffraction effects, as discussed in Appendix 1. This is can be important as a result of subtle errors caused by the difference in sound velocity between the liquid samples used in these studies and the water used as a reference.

Considerations for the ultrasonic pulse employed

The ultrasonic signal employed for the measurement of the nonlinear parameter of a sample is a narrowband tone-burst. Several issues must be addressed regarding concerning the determination of an optimal number of cycles and amplitude of a narrowband signal to use. Because power delivered to the transmitting transducer has to be limited to avoid damaging the transducer, there is a tradeoff between the length of the narrowband pulse train, which increases the spectral purity of the pulse, and the need to have higher amplitude signals, which result in a higher signal-to-noise ratio as well as a more distorted nonlinear response (which is governed by the square of the ultrasonic pressure).

Another issue regarding the ultrasonic pulse employed is the narrowband fundamental frequency that is used throughout the experiments. The choice of frequency affects many ultrasonic phenomena of interest here,

- the nonlinear distortion of a pulse (equation 3-3)
- the attenuation of both the sample and reference
- the diffraction field (as seen from the shock distance, equation 3-23), and
- the pulse characteristics.

Over the course of the study, fundamental frequencies of both 7 MHz and 2.25 MHz were employed. The 7 MHz approach was employed when using the stainless steel delay line method. The 2.25 MHz approach was used when employing the method of Dong *et. al.*[3] for measuring the nonlinear parameter. The 2.25 MHz frequency method necessitated the use of the longest possible beam path that the laboratory water tanks could accommodate, as well as a weaker pressure pulse, which decreased the overall signal-to-noise ratio throughout the experiment.

Methods and results for the measurement of the nonlinear parameter

Under the assumption that the thickness, attenuation, density, speed of sound, and transmission properties of the sample can be accurately determined, the nonlinear parameter can be calculated through equation 3-21, which is reprinted here for convenience.

$$\frac{\left(\frac{B}{A}+2\right)_X}{\left(\frac{B}{A}+2\right)_O}=\left[\frac{p_{2,X}}{p_{2,O}}\frac{L}{d}-\left(\frac{L}{d}-1\right)I_2^2D'D''\right]\cdot\frac{\rho_X c_X^3}{\rho_O c_O^3}\frac{d}{D''^2D'}\frac{2\alpha(1f)-\alpha(2f)}{I_2^2-I_1^2} \qquad (3\text{-}21)$$

The series of steps necessary to implement the long-path, glycerol attenuator method of Dong *et. al*. are outlined here. Chambers for the liquids of interest as well as for glycerol are prepared. Ideally, the thickness of these chambers would be constant over the area of the acoustic window. The transmitting transducer is a Panametrics V309, 5 MHz, ½" diameter planar or a V306, 2.25 MHz, ½" diameter planar transducer. The receiving transducer is a Sonic Industries model 804 bilaminar hydrophone, with a 0.6 mm effective element diameter. The transmitting transducer is mounted in the water tank using plastic fixtures that can be aligned manually, whereas the receiving transducer is mounted on a motion control stage in order to act as a receiver for multiple measurements. The narrowband signals are generated using a HP 8116A function generator and amplified with an ENI 204L broadband amplifier connected to the transmitting transducer. Broadband signals are generated using a Panametrics 5800 pulser/receiver. Received signals from the hydrophone are passed through a pre-amplifier before being routed to a Tektronix 5052B oscilloscope for off-line analysis of the signal.

The mass density of the sample was determined using mass and volume measurements, or alternately by employing Archimedes' principle to determine the density of the sample. The Sollish experiment described above is used to ascertain the velocity and thickness of the sample. Subsequently, the attenuation of the sample at both the fundamental and second harmonic frequencies is determined via narrowband and broadband substitution experiments, as described in brief above. Finally, the nonlinear parameter is determined by measuring the nonlinear distortion of a pressure signal both

with and without a sample present using equation 3-21 and the parameters measured previously.

In spite of repeated efforts to reduce uncertainties arising from a number of experimental factors (which are elucidated below), the results of these determinations of the nonlinearity parameter were unsatisfying. Although the average value obtained for the nonlinearity parameter of ethylene glycol was 9.7 ± 1.6, which matches the Dong *et. al.* value of 9.8, the standard deviation of 1.6 represents an unacceptably large uncertainty. Even less satisfying were the results for the nonlinear parameter of isopropanol. Although an average value of 11.9 ± 4.8 was obtained for one set of measurements (to be compared with an accepted value of 11.8), another set of measurements yielded 6.0 ± 1.7.

Discussion

A systematic series of studies were carried out to assess the relative importance of factor believed to be responsible for the unsatisfying outcome of these very time consuming experiments. Although a number of factors are worthy of note, the dominant factor limiting the reproducibility of measurements of the nonlinear parameter was the attenuation coefficient of the material of interest. This error was exacerbated by the particular choice of sample materials, because the true value of the attenuation is small, to the point where the attenuation of the "lossless" water is on the order of 5 to 10 percent of the attenuation of these sample liquids. Because the terms involving the attenuation coefficient are loss terms and thus appear in exponentials, error in the measurement of the attenuation coefficient affects the error in the nonlinear parameter in an exponential

manner. Ethylene glycol and isopropanol were chosen because their nonlinearity parameters were known, thus permitting comparison between the results of these studies and accepted values. However, for biomedical applications of nonlinear ultrasound, the material of interest, soft tissue, exhibits attenuation coefficients that are substantially larger in value than those of ethylene glycol and isopropanol. As a consequence, it is likely that the major stumbling block encountered in these investigations will play a relatively minor role in application of these techniques to studies of soft tissue.

Beyond the effects governed by errors in the determination of the attenuation coefficient, the dominant remaining sources of variability were random errors in the measurement of the second harmonic pressure. The signal-to-noise ratio was consistently poor in these experiments because the pressures are small. Because these pressures are so weak, a substantial amount of signal averaging was used to reduce the effects of noise (typically 4096 traces were averaged). Unfortunately, tiny variations in sample thickness that appeared be associated with small liquid currents in the tank somewhat compromised the benefits of signal averaging.

The second harmonic pressure was increased as much as possible by increasing the amplitude of the drive level, which required reducing to 8 the number of cycles transmitted, resulting in somewhat reduced spectral purity. Subtle misalignment of the sample chamber, along with beam steering caused by the chamber, is another challenging experimental limitation. At the expense of a substantial amount of time and effort, mapping the beam with the membrane hydrophone could identify the resulting shift in the ultrasonic beam. Yet another factor centers on the difficulties involved with containing liquid samples in a water bath. The challenge lies in the amorphous nature of the liquids

and the difficulties in achieving a sample thickness that is constant (especially as the disparity between the sample and host mass densities grows large). This affects the determination of the nonlinear parameter directly by changing the thickness that is inserted into equation 3-21. Moreover, variations in sample thickness result in significant errors in estimates of the attenuation coefficient, as well as more modest errors in measurements of phase velocity.

In summary, a previously published method for the measurement of the nonlinear parameter and some alternate methods have been explored. This type of finite-amplitude method may be of value as a potential standard against which to evaluate other techniques that estimate the nonlinear parameter. Although the results acquired here proved unsatisfactory for that purpose, the methods described may provide a starting point for future refinement and eventual success in the accurate and precise measurement of the nonlinear parameter.

References

1. Wallace, K.D., Ph.D. thesis, Washington University in Saint Louis (2001).
2. Wallace, K.D., C.W. Lloyd, M.R. Holland, and J.G. Miller, Finite amplitude measurements of the nonlinear parameter B/A for liquid mixtures spanning a range relevant to tissue harmonic mode. Ultrasound in Medicine and Biology, Ultrasound Med Biol 2007;33(4):620-9.
3. Dong, F., E. Madsen, M. MacDonald, and J. Zagzebski, Nonlinearity parameter for tissue-mimicking materials. Ultrasound in Medicine and Biology 1999;25:831-838.
4. Gong, X.-F., F. Ruo, Z. Cheng-ya, and S. Tao, Ultrasonic investigation of the nonlinearity parameter B/A in biological media. Journal of the Acoustical Society of America 1984;76:949-50.
5. Shklovskaya-Kordi, V.V., An acoustic method of determining the internal pressure in a liquid. Soviet Physics - Acoustics 1963;9:82-85.
6. Kinsler, L.E., A.R. Frey, A.B. Coppens, and J.V. Sanders, *Fundamentals of Acoustics, 4th ed.* 2000, New York: John Wiley and Sons, Inc. 179-184.
7. Gong, X.-F., Z.-M. Zhu, T. Shi, and J.-H. Huang, Determination of the acoustic nonlinearity parameter in biological media using FAIS and ITD methods. Journal of the Acoustical Society of America 1989;86:1-5.
8. Wallace, K.D., C.W. Lloyd, M.R. Holland, and J.G. Miller, Finite Amplitude Measurements of the Nonlinear Parameter B/A for Liquid Mixtures Spanning a Range Relevant to Tissue Harmonic Mode. Ultrasound in Medicine & Biology 2007;33(4):620-629.

9. Del Grosso, V.A. and C.W. Mader, Speed of Sound in Pure Water. The Journal of the Acoustical Society of America 1972;52(5B):1442-1446.

10. Herman, B.A. and G.R. Harris, Calibration of miniature ultrasonic receivers using a planar scanning technique. The Journal of the Acoustical Society of America 1982;72(5):1357-1363.

11. Sollish, B.D., "A device for measuring ultrasonic propagation velocity in tissue," Ultrasonic Tissue Characterization II **Spec. Publ. 525**, 53-56 (1979).

12. Trousil, R.L., Ph.D. thesis, Washington University in Saint Louis (2002).

13. Ophir, J., T.H. Shawker, N.F. Maklad, J.G. Miller, S.W. Flax, P.A. Narayana, et al., Attenuation estimation in reflection: Progress and prospects. Ultrasonic Imaging 1984;6(4):349-395.

Chapter 4: Methods for Determining the Nonlinear Parameter B/A from Backscattered Signals

List of Parameters used in this Chapter:

$A_0(2f_0)$ - transmitted amplitude of a harmonic signal, centered at $2f_0$, as defined by Fujii *et. al.*

$A_2(x)$ - received backscatter at $2f$ for the $1f$-transmitted case (harmonic imaging at $2f$)

$A_{II}(x)$ - received backscatter at $2f$ for the $2f$-transmitted case (fundamental imaging at $2f$)

$\alpha(f,x)$ - local (i.e. at x) attenuation of the material at a frequency f

$\frac{B}{A}$ - nonlinear parameter

c_0 - speed of sound of the material

$F(x)$ - diffraction functional form for the $1f$-transmitted case (harmonic imaging at $2f$)

$F'(x)$ - diffraction functional form for the $2f$-transmitted case (fundamental imaging at $2f$)

f - frequency ($1f$ or f_0 are explicitly meant to mean a fundamental frequency)

$\gamma(f,x)$ - local (i.e. at x) backscattering parameter

$h = \left(\frac{B}{A} + 2\right) \bullet \frac{\pi f}{2\rho_0 c_0^3}$ - a lumped local nonlinear parameter

$P_0(f_0)$ - transmitted pressure amplitude (or power – this is not clearly defined initially) of a fundamental signal, centered at f_0, as defined by Fujii *et. al.*

p_1 - pressure amplitude at the fundamental frequency

$p_{1,m}(x)$ - axial, measured transmitted fundamental pressure

p_2 - pressure amplitude at the second harmonic frequency

$p_{2,m}(x)$ - axial, measured transmitted second harmonic pressure

ρ_0 - mass density of the material

x - axial distance from a transmitting transducer

Introduction

The reason for the inclusion of this Chapter is to consider the merits of being able to measure the nonlinear parameter B/A of a sample material using pulse-echo methods, instead of the familiar and more well-known through-transmission methods. This Chapter was inspired by (and is both an extension and a reformulation of) a manuscript published by Fujii *et. al.*[1] in 2004, which in turn was based on methods that were proposed by both Akiyama[2] and Bjørnø[3].

The determination of the nonlinear parameter B/A can be performed in two fundamentally different ways:[3, 4] the thermodynamic method (which uses the change in either the speed of sound or phase of a signal as a function of pressure to directly determine B/A) or the finite amplitude method (which utilizes the generation of harmonic distortion as an ultrasonic wave of finite amplitude, as opposed to infinitesimally small, propagates through a sample). Use of either the thermodynamic method or a through-transmission translation of the finite amplitude method can be impractical in a clinical setting. In the case of the thermodynamic method, the tissue of interest cannot be removed for *in vitro* study. In this case alternate measurement methods are necessary, which for example may implement two intersecting ultrasonic beams to study the tissue.[5,

[6] In this method, a high intensity ultrasound pumping beam (which is limited in intensity to avoid biological effects) is applied to the tissue of interest. A second ultrasonic beam then probes the region of interest, and the pressure fluctuations of the pumping beam modulate the phase of the probing beam in the region where they intersect. This phase modulation is related to the nonlinear parameter of the tissue. However, overlying tissue can interfere with the determination of B/A, and the generation of spatial information for B/A is affected by factors that disrupt standard image formation, such as beam aberration and steering, as well as phase cancellation across the face of a finite-sized receiver.

The use of the finite-amplitude method using through-transmission is another example of a method of study that works well *in vitro*, but not in studies conducted *in vivo*. The use of two transducers (one for the transmission of ultrasound, and one for the subsequent receiving of ultrasound) may be impractical in a clinical setting since access to both sides of the tissue of interest may not be available. For some cases in which access to both sides is available, such as in some regions of the torso, the signal loss through the torso is too large for the transmission of an ultrasonic signal. It is these tissue types (internal organs) that would potentially benefit from the determination of the nonlinear parameter present for the determination of pathology.[1, 7, 8] The use of this type of measurement for smaller propagation thicknesses, such as limbs and for individual muscles, might be more amenable to this arrangement.

Alternatively, the employment of a finite-amplitude method that utilizes a pulse-echo measurement (one transducer both sends and receives the ultrasonic signal) would bypass many of the aforementioned issues, but additionally would leverage a well-established body of knowledge, because the processing of backscattered ultrasonic

signals has been central to many ultrasonic imaging systems. Accordingly, Fujii *et. al.*[1] proposed an experimental setup for measuring this nonlinear parameter *in vivo*, by considering the ratio of the amplitudes of two backscattered signals, both of which were at the second harmonic (2*f*) frequency compared to an established fundamental (1*f)* frequency. These backscattered amplitudes were generated in two different scenarios: the backscatter of the harmonic (2*f*) pressure component of a fundamental (1*f*) pressure wave, and the backscatter of the fundamental (2*f*) pressure component of a fundamental (2*f*) pressure wave. These measurements are illustrated in Figure 4-1, which depicts schematically the two scenarios. The result of the derivation, as found in Fujii *et. al.,* is that the local nonlinear lumped parameter h(x) can be found through the measurement of four factors,

$$h \equiv \left(\frac{B}{A}+2\right)\cdot\frac{\pi f}{2\rho_0 c_0^3} = \frac{A_0(2f_0)}{P_0(f_0)}\frac{d}{dx}\left[\frac{A_2(x)}{A_{II}(x)}\right] \tag{4-1}$$

Here, the lumped parameter h is defined in terms of the nonlinear parameter (B/A), the fundamental frequency of interest (*f*), the density of the sample (ρ), and the speed of sound of the sample (c). The second part of this equality states that the local nonlinear parameter can be determined from the initial pressure amplitudes of two different propagated beams (A_0, P_0) as well as the rate of change of the ratio of backscattered signals at the second harmonic frequency (A_2, A_{II}).

The purpose of this Chapter is to explore the derivation of the nonlinear parameter equation of Fujii *et. al.*[1] (equation 6 in the manuscript, reproduced as equation 4-1 above), in the context of studying nonlinear ultrasound and its potential for ultrasonic tissue

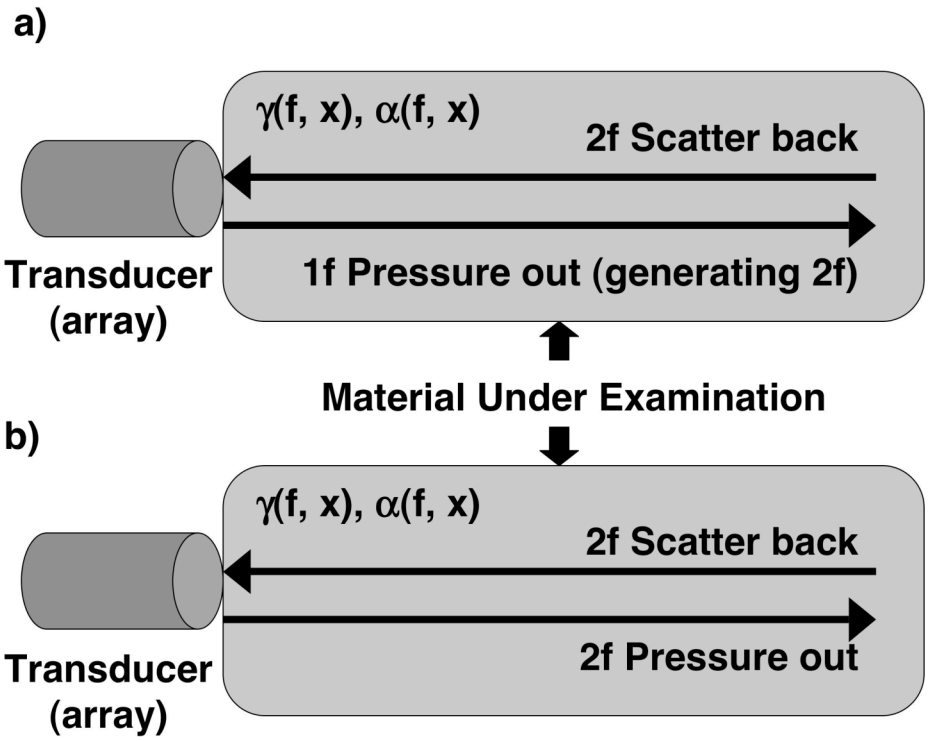

Figure 4-1: Illustration of the two data collection methods required for the determination of the nonlinear parameter of a material using backscattered sound. a) One measurement utilizes the harmonic (2f) signal generated by the propagation of a fundamental pressure (1f) through the material under examination. b) Another measurement uses a fundamental signal (at the harmonic frequency 2f) as the propagated pressure for which some signal will be scattered backwards.

characterization in pulse-echo imaging. The immediate issue is an apparent discrepancy in equation 4-1: if P_0 is a pressure amplitude (as explicitly stated in the manuscript), then the right-hand side of equation 4-1 is dimensionally inconsistent with the definition of h(x). To address this matter, in this Chapter the formalism will be re-derived from a more general perspective, and consequences arising from the subsequent formalism for the potential measurement of the nonlinear parameter in tissue will be examined. However, these consequences have not been directly tested via experiment as of yet.

Theory

The underlying theory for an experiment of this type regards the promotion of energy from a fundamental frequency (*f*) to the second harmonic frequency (2*f*). An early treatment of the subject was given by Thuras *et. al.*[9], who summarized the contributions of Rayleigh, Lamb, and Rocard on the topic. This body of work was revisited by Shklovskaya-Kordi[10] as well as Gong *et. al.*[8] The relevant equation of interest is for the determination of the harmonic pressure for a finite amplitude plane wave, as a function of propagation distance,

$$p_2 = p_1^2 \cdot x \cdot \left(1 + B/2A\right) \cdot \frac{\pi f}{\rho_0 c_0^3} \tag{4-2}$$

With these constraints, the generation of the harmonic pressure p_2 is dependent upon several factors: the square of the fundamental pressure, the propagation distance, the coefficient of nonlinearity (1 + B/(2A)) that governs the nonlinear process, and a collection of constants and material parameters. Additionally, because an approximation applied here is that of a plane wave, the derivative of the second harmonic (the rate of growth) reduces to a simple factor,

$$\frac{dp_2}{dx} = p_1^2 \cdot \left(1 + B/2A\right) \cdot \frac{\pi f}{\rho_0 c_0^3} = p_1^2 \cdot h \tag{4-3}$$

At this point, the loss due to attenuation can be inserted for both the fundamental and second harmonic pressures. The latter is achieved by considering the derivative of an exponential,

$$\frac{d}{dx} e^{-\alpha x} = -\alpha \cdot e^{-\alpha x} \tag{4-4}$$

The former is achieved by explicitly including the functional form of the attenuation coefficient with the fundamental pressure, leaving a differential equation of

$$\frac{dp_2}{dx} = \left[p_1(0) e^{-\alpha(f)x} \right]^2 \cdot h - \alpha(2f) p_2(x) \tag{4-5}$$

The solution proposed by Gong *et. al.*[8] for this equation is

$$p_2(x) = \left[p_1(0) \right]^2 \cdot x \cdot h \cdot e^{-\left(\alpha(f)+\alpha(2f)/2\right)x} \tag{4-6}$$

Equation 4-6 (which is equation 3 in the Gong study) is constrained to the case when the attenuation coefficient of the material increases approximately linearly with frequency (i.e. $\alpha(2f) \approx 2 \cdot \alpha(f)$), although the reason for this constraint is not obvious.

As an alternative to this approach, a more general case can be considered that allows for diffraction. Because the generation of harmonic signals is dependent upon the pressure of the fundamental ultrasonic signal, any fluctuation due to axial or lateral diffraction will have an effect on the subsequent generation of signal. For a pressure measurement that is performed on the beam axis of an axisymmetric source at some axial distance x, the received pressure will change as a function of axial distance due to the changing diffractive field. Yet, as long as the measurements are performed on the beam axis, the change in the received pressure can either be measured or simulated to determine the physical diffractive field. As a result, the expression for the fundamental pressure is an explicit function of distance and attenuation,

$$p_1(x) = p_{1,m}(x) e^{-\int_0^x \alpha(f,x')dx'} \tag{4-7}$$

If this is considered, then the method of Gong *et. al.*[8] can be recast in the following way. The rate of change of the second harmonic component of the pressure is

related to two competing factors, namely the gain due to the nonlinear generation of the second harmonic from the fundamental signal that is present, and the loss due to the attenuation of the harmonic signal. Further, to account for the potential for inhomogeneities in the medium, the possibility of a spatial dependence of the lumped nonlinear parameter and the attenuation coefficient will be explicitly added here. After the upcoming derivation of the lumped nonlinear parameter, a subsequent approximation of homogeneity should result in agreement with earlier published theory. Equation 4-5 can then be rewritten as

$$\frac{dp_2}{dx} = \left(p_1(x)\right)^2 \cdot h(x) - \alpha(2f,x)\, p_2(x) \tag{4-8}$$

This can be rearranged to yield a more familiar type of equation in the variable p_2,

$$\frac{dp_2}{dx} + \alpha(2f,x)\, p_2(x) = \left(p_1(x)\right)^2 \cdot h(x) \tag{4-9}$$

The resulting equation is a first-order, inhomogeneous, ordinary differential equation, which can be solved using the integrating factor method,

$$\frac{\partial p_2}{\partial x} e^{\int_0^x \alpha(2f,x')dx'} + \alpha(2f,x)\, p_2(x) e^{\int_0^x \alpha(2f,x')dx'} = \left(p_1(x)\right)^2 \cdot h(x) e^{\int_0^x \alpha(2f,x')dx'} \tag{4-10}$$

$$\frac{d}{dx}\left[p_2(x) e^{\int_0^x \alpha(2f,x')dx'} \right] = \left(p_1(x)\right)^2 \cdot h(x) e^{\int_0^x \alpha(2f,x')dx'} \tag{4-11}$$

$$\left[p_2(x') e^{\int_0^{x'} \alpha(2f,x'')dx''} \right]_{x'=0}^{x} = \int_0^x \left(p_1(x')\right)^2 \cdot h(x') e^{\int_0^{x'} \alpha(2f,x'')dx''} dx' \tag{4-12}$$

$$p_2(x)e^{\int_0^x \alpha(2f,x')dx'} - p_2(0) = \int_0^x \left(p_1(x')\right)^2 \cdot h(x') e^{\int_0^{x'} \alpha(2f,x'')dx''} dx' \qquad (4\text{-}13)$$

$$p_2(x) = e^{-\int_0^x \alpha(2f,x')dx'} \cdot \left[p_2(0) + \int_0^x \left(p_1(x')\right)^2 \cdot h(x') e^{\int_0^{x'} \alpha(2f,x'')dx''} dx' \right] \qquad (4\text{-}14)$$

Equation 4-14, although comparatively messy, is a restatement of how much second harmonic pressure is generated for a distance x away from the ultrasonic source. Here, there are once again two terms present, but with different interpretations. The first is an initial second harmonic pressure that is present at the source plane (x=0) that might represent the nonlinear pressure at the source plane that is present, for example, because the ultrasonic source emitted unwanted higher harmonics. The second term is the continuously evolving second harmonic pressure that is both simultaneously increasing due to harmonic generation and decreasing due to attenuation. For a fundamental pressure of the form found in equation 4-7, equation 4-14 can be rewritten as

$$p_2(x) = e^{-\int_0^x \alpha(2f,x')dx'} \cdot \left[p_2(0) + \int_0^x \left(p_{1,m}(x')\right)^2 \cdot h(x') e^{\int_0^{x'} -2\alpha(f,x'')+\alpha(2f,x'')dx''} dx' \right] \qquad (4\text{-}15)$$

With the nonlinearly generated pressure in the field derived, the experimental setup proposed by Fujii *et. al.*[1] can now be considered, in which the lumped nonlinear parameter h is measured using two experiments. The first measurement samples the backscattered field from a specimen in order to determine the nonlinearly generated harmonic component of the beam. The interaction of sound here is such that equation 4-15 describes the evolution of the nonlinear pressure in the field as it propagates to a scattering site. Once at the site, the wave will scatter according to the local scattering

properties, $\gamma(2f, x)$, and the scattered wave then propagates back to the source, although this signal will also be attenuated. This process, and the resulting received backscattered nonlinear pressure at the source plane, $A_2(x)$, can be expressed as

$$A_2(x) = \left\{ e^{-\int_0^x \alpha(2f,x')dx'} \cdot \left[p_2(0) + \int_0^x \left(p_{1,m}(x')\right)^2 \cdot h(x') e^{\int_0^{x'} -2\alpha(f,x'')+\alpha(2f,x'')dx''} dx' \right] \right\} \cdot \gamma(2f,x) \cdot e^{-\int_0^x \alpha(2f,x')dx'} \quad (4\text{-}16)$$

which can be simplified slightly to yield

$$A_2(x) = \left\{ e^{-2\int_0^x \alpha(2f,x')dx'} \cdot \left[p_2(0) + \int_0^x \left(p_{1,m}(x')\right)^2 \cdot h(x') e^{\int_0^{x'} -2\alpha(f,x'')+\alpha(2f,x'')dx''} dx' \right] \right\} \cdot \gamma(2f,x) \quad (4\text{-}17)$$

The second measurement of this experiment samples the backscattered field from a specimen using a linearly propagated ultrasonic beam transmitted at the second harmonic frequency ($2f$). This ultrasonic beam will also be affected by attenuation and diffraction and will propagate the same distance x before being scattered off of the same material site. The scattered signal will be attenuated as it returns to the source plane. The measured signal in this case, A_{II}, can be expressed as

$$A_{II}(x) = \left[p_{2,m}(x) e^{-\int_0^x \alpha(2f,x')dx'} \right] \cdot \gamma(2f,x) \cdot e^{-\int_0^x \alpha(2f,x')dx'} \quad (4\text{-}18)$$

$$A_{II}(x) = p_{2,m}(x) e^{-2\int_0^x \alpha(2f,x')dx'} \cdot \gamma(2f,x) \quad (4\text{-}19)$$

The ratio of equation 4-17 to equation 4-19 is

$$\frac{A_2(x)}{A_{II}(x)} = \frac{p_2(0) + \int_0^x \left(p_{1,m}(x')\right)^2 \cdot h(x') e^{\int_0^{x'} -2\alpha(f,x'') + \alpha(2f,x'')dx''} dx'}{p_{2,m}(x)} \tag{4-20}$$

The purpose of this experiment is to find the lumped nonlinear parameter, h(x), so equation 4-20 can be solved for this parameter,

$$p_{2,m}(x) \cdot \frac{A_2(x)}{A_{II}(x)} - p_2(0) = \int_0^x \left(p_{1,m}(x')\right)^2 \cdot h(x') e^{\int_0^{x'} -2\alpha(f,x'') + \alpha(2f,x'')dx''} dx' \tag{4-21}$$

$$\frac{d}{dx}\left(p_{2,m}(x) \cdot \frac{A_2(x)}{A_{II}(x)} - p_2(0) \right) = \frac{d}{dx} \int_0^x \left(p_{1,m}(x')\right)^2 \cdot h(x') e^{\int_0^{x'} -2\alpha(f,x'') + \alpha(2f,x'')dx''} dx' \tag{4-22}$$

$$\frac{d}{dx}\left(\frac{p_{2,m}(x) A_2(x)}{A_{II}(x)} \right) = \left(p_{1,m}(x)\right)^2 \cdot h(x) e^{\int_0^{x} -2\alpha(f,x') + \alpha(2f,x')dx'} \tag{4-23}$$

$$h(x) = \frac{1}{\left(p_{1,m}(x)\right)^2} \cdot e^{\int_0^{x} \left(2\alpha(f,x') - \alpha(2f,x')\right)dx'} \cdot \frac{d}{dx}\left(\frac{p_{2,m}(x) A_2(x)}{A_{II}(x)} \right) \tag{4-24}$$

The implications of equation 4-24 can now be discussed, including special cases for specific functional forms of the attenuation coefficient of the material and the implications of the dependence of h(x) on the spatial derivative of the diffractive field.

Discussion

From equation 4-24, the expression for the local nonlinear parameter, h(x), has three lumped terms, which are, from left to right:

- a term dealing with the fundamental frequency pressure in the nonlinear generation measurement,

- a term dealing with the relative effects of attenuation for the fundamental frequency pressure versus the second harmonic pressure in the nonlinearly generated harmonic field, and
- a relative rate of change of the backscattered harmonic signals in both measurements, weighted by the local pressure in the fundamentally propagated harmonic frequency measurement.

In this form, the lumped nonlinear parameter h(x) can be determined from measurements of the attenuation and backscatter from a sample at the two frequencies (f and $2f$), provided that the local ultrasonic pressure is known as a function of axial distance (from the diffraction pattern). The most scientifically satisfying method of attempting this measurement would be to measure the attenuation coefficient (at both the fundamental and harmonic frequencies) of the sample as a function of distance, as well as the diffraction pattern of the transmitted ultrasonic field in both measurements. These, combined with the ratio of harmonic backscatter as a function of depth, would then be used in equation 4-24 (the general driving equation) to specify h(x) exactly.

In the specific application of this methodology to heterogeneous solids, however, there are two issues that preclude the exact form of equation 4-24. First, the attenuation coefficient of a heterogeneous material will not usually be a well-known function of position. Second, the diffraction patterns may not be easily determined, because aberrative artifacts inside of a heterogeneous solid are difficult to estimate (as opposed to the case of homogeneous solids, where the diffractive effects are well-known). Both effects can be illustrated by considering the measurement of tissue (say, the liver) inside the human torso. On average, the attenuation coefficients of the specific tissues are

known, but the values of the attenuation coefficient at individual spatial locations would not be known. Such attenuation values could only be determined through pulse-echo methods,[11] because the determination of the attenuation coefficient for tissue *in vivo* cannot be readily obtained by placing a receiver at locations in the tissue for a through-transmission method. Similarly, although the diffraction pattern of a single element transducer or a transducer array can be either simulated or experimentally determined under controlled circumstances (such as an experiment in a water tank), the diffraction of the ultrasonic field in the human torso is likely to be altered by propagation through the myriad tissue types. These irregular tissue interfaces, along with the heterogeneous nature of organs, will cause a distortion of the shape and direction of the ultrasonic beam that cannot be determined without complete knowledge of the properties of the tissue being studied.

The study by Fujii *et. al.*[1] does attempt to resolve these two issues in order to make the determination of the nonlinear lumped parameter h(x) more tractable. The issue of attenuation is rather straightforward, in that an approximation can be utilized to insert into the exponential terms of equation 4-24. For the special case of tissue that has been discussed, the functional form of the attenuation coefficient is a linear function of frequency (or does not differ appreciably from a linear form). This means that

$$\alpha(2f,x) = 2 \cdot \alpha(f,x) \tag{4-25}$$

and, by insertion into the middle term of equation 4-24, the measurement of the lumped nonlinear parameter no longer depends on the attenuation of the overlying tissue (because the term goes to one identically),

$$h(x) = \frac{1}{\left(p_{1,m}(x)\right)^2} \cdot \frac{d}{dx}\left(\frac{p_{2,m}(x) A_2(x)}{A_{II}(x)} \right) \tag{4-26}$$

This result can be compared to the driving equation as proposed by Fujii *et. al.,*[1]

$$h(x) = \frac{A_0(2f_0)}{P_0(f_0)} \frac{d}{dx}\left[\frac{A_2(x)}{A_{II}(x)} \right] \tag{4-1}$$

and, as seen, there are still differences between the derivation as presented through this Chapter and the published result. One difference is the prefactor term in equation 4-26, which is expressed as an amplitude squared (with a dependence on distance). In the Fujii *et. al.* paper the corresponding term P_0 is described in two ways:

- "When the pressure **amplitude** of the transmitted signals of the center frequency f_0 is $P_0(f_0)$, …"
- "Because $P_0(f_0)$ and $A_0(2f_0)$, which, respectively, correspond to the **power** and the amplitude of the transmission…"

Dimensional analysis suggests that this P_0 term is a power, and this is further supported by noting that the derivation of h(x) requires a squared amplitude term for the nonlinear generation term (because the harmonic pressure grows proportionally to the square of the fundamental pressure). This aside, the lack of a functional dependence on the propagation distance for the second harmonic pressure (in the numerator) from equation 4-1 means that this formula can only be exactly correct for plane wave propagation over the entire path length – a scenario that is improbable for any appreciable propagation distance.

The complication of a diffraction term has to be resolved if an exact expression for h(x) is to be determined. In the discussion section of Fujii *et. al.*[1] there is some

discussion concerning the diffraction pattern. The authors propose to add a diffraction term (F(x) or F'(x), for the harmonic imaging and fundamental imaging measurements respectively) in order to express the ratio of received backscattered amplitudes as

$$\frac{A_2(x)}{A_{II}(x)} = \frac{P_0(f_0)}{A_0(2f_0)} \cdot \frac{F(x)}{F'(x)} \int h(x')dx' \qquad \text{(Fujii 10)}$$

$$h(x) = \frac{A_0(2f_0)}{P_0(f_0)} \frac{d}{dx}\left[\frac{A_2(x)F'(x)}{A_{II}(x)F(x)}\right] \qquad \text{(4-27)}$$

This expression still differs from the derivation solution found in this Chapter (see equation 4-26), because the pressure field of the fundamental pressure in the harmonic imaging case was not handled appropriately. Because the diffraction field of this pressure matters (because the local promotion of energy to the harmonic second frequency depends on the square of the local fundamental frequency), the term F(x) cannot be removed from the integral that appears as equation 16 here (where $P_0(f_0)$ * $(F(x))^2$ is represented by $(p_{1,m})^2$). Instead, the derivation would be performed as above, with a spatial derivative used to solve for h(x). Because F(x) lies with h(x) inside of this integral, it would lie outside the derivative found in equation 4-27. Combining P_0 with F(x) to create a diffracted pressure field outside of the derivative (and doing the same with A_0 and F'(x) inside the derivative) recovers equation 4-26.

To proceed, this discussion has to touch on ways of making the full measurement of the terms in equation 4-26 tractable, in order to demonstrate on a theoretical level the feasibility of this measurement method. The backscattered harmonic signals can be measured as a function of depth, but the absolute pressure fields themselves are more challenging to determine. For each measurement, a calibration is required to determine the initial pressure, and a functional form of the diffractive field needs to be known, as

well. It is conceivable that this functional form can be determined at the same time as a calibration, because the pressure field of the transducer in both cases can be determined using a calibrated point-like receiver that samples the ultrasonic field along the main axis of the transducer. For a non-aberrating material, the terms are calculated directly. In the presence of aberration, however, one must justify the functional forms that are used. For example, if the aberration is weak, the corresponding distortion would also be weak, and the error in using the measured, unaberrated field for equation 4-26 would be a small-order term. Alternatively, if the aberration is not a function of frequency, the distortion effects evidenced in the diffraction pattern would operate on both transmitted pressures in a similar manner, and the error in using the measured functional forms might be minimized. In both cases, a more stable value of h(x) can found when the terms inside the differential of equation 4-26 are plotted and the derivative calculated from a line of best fit that covers a spatial region of interest. This method yields a value for the nonlinear lumped parameter while ignoring the random oscillations found by taking the ratio of spatial backscatter values.

For special cases, the pressure field has a known form that can be applied to make the problem easier. One case is for plane wave propagation, which can be approximated by working extremely close to the transducer (such that edge signals cannot interfere with the signals from the middle of a transducer) or to a certain extent in the focal region of the transducer (where there is variation but the spatial derivative of the pressure is modest). In these regions the pressure is independent of position and can be removed from the derivative. In the far field, when the transducer can be approximated as a point-like transmitter, the lateral pressure dependence appears planar (that is, like the tangent

plane to a large sphere) but the axial pressure has a simple inverse dependence on distance. This distance dependence could then be evaluated along with the measured ratio of backscattered amplitudes.

The lumped nonlinear parameter h(x) can be interpreted as-is, or solved for the underlying nonlinear parameter B/A. The work of Fujii *et. al.*[1] focused on the parameter h, because of the dependence not only on the nonlinear parameter B/A, but also the density and speed of sound of the tissue. In this case, the tissue that was studied was liver with varying amounts of fatty infiltrations; the ratio of h values for the *in vivo* fatty versus normal livers closely matched the known *in vitro* values of B/A. It was determined that the change in the speed of sound as well as the density of the tissue did not change enough to be useful as a sensitive marker for finding fatty deposits. However, it should be made clear that larger changes will obscure any dependence in the change of h(x) on the underlying nonlinear parameter B/A, because a large change in the speed of sound, for instance, might cause a change in the value of h(x) independent of a change in the nonlinear parameter B/A. As such, unless the materials making up the heterogeneous system are closely matched in density and speed of sound, care must be taken in inferring a value for the nonlinear parameter B/A from the measurements of h(x).

In conclusion, this Chapter examined the derivation and application of pulse-echo theory for the measurement of the nonlinear parameter B/A, as opposed to the more common through-transmission approaches. Some issues that appeared to exist in previously published work have been examined and resolved to the extent possible at the current time.

References

1. Fujii, Y., N. Taniguchi, I. Akiyama, J.-W. Tsao, and K. Itoh, A new system for in vivo assessment of the degree of nonlinear generation using the second harmonic component in echo signals. Ultrasound in Medicine and Biology 2004;30(11):1511-1516.
2. Akiyama, I., *Reflection mode measurement of nonlinearity parameter B/A*, in *Nonlinear Acoustics At the Turn of the Millennium*, W. Lauterborn and T. Kutz, Editors. 2000, Elsevier: London. p. 321-324.
3. Bjorno, L., Characterization of biological media by means of their non-linearity. Ultrasonics 1986;24:254-9.
4. Law, W.K., L.A. Frizzell, and F. Dunn, Ultrasonic determination of the nonlinearity parameter B/A for biological media. Journal of the Acoustical Society of America 1981;69:1210-12.
5. Ichida, N., T. Sato, H. Miwa, and K. Murakami, Real-Time Nonlinear Parameter Tomography Using Impulsive Pumping Waves. Sonics and Ultrasonics, IEEE Transactions on 1984;31(6):635-641.
6. Bjorno, L. and P.A. Lewin, *Measurement of Nonlinear Acoustic Parameters in Tissue*, in *Tissue Characterization With Ultrasound*, J.F. Greenleaf, Editor. 1986, CRC Press, Inc.: Boca Raton, Florida. p. 141-163.
7. Law, W.K., L.A. Frizzell, and F. Dunn, Determination of the nonlinearity parameter B/A of biological media. Ultrasound in Medicine and Biology 1985;11:307-18.

8. Gong, X.-F., Z.-M. Zhu, T. Shi, and J.-H. Huang, Determination of the acoustic nonlinearity parameter in biological media using FAIS and ITD methods. Journal of the Acoustical Society of America 1989;86:1-5.

9. Thuras, A.L., R.T. Jenkins, and H.T. O'Neil, Extraneous Frequencies Generated in Air Carrying Intense Sound Waves. The Journal of the Acoustical Society of America 1935;6(3):173-180.

10. Shklovskaya-Kordi, V.V., An acoustic method of determining the internal pressure in a liquid. Soviet Physics - Acoustics 1963;9:82-85.

11. Blodgett, E.D., P.H. Johnston, and J.G. Miller. *Estimating Attenuation in Composite Laminates Using Backscattered Ultrasound*. in *IEEE 1984 Ultrasonics Symposium*. 1984, 748-753.

Chapter 5: Improving the Reproducibility of the Measurements of the Magnitude of Cyclic Variation, Utilizing a New "Auto-Averaged" Approach

Background

The goal of myocardial tissue characterization is to augment information provided by two- and three-dimensional echocardiographic imaging, Doppler blood flow, and speckle- or Doppler-derived tissue motion. Myocardial tissue characterization based on the systematic variation of backscattered ultrasound during the cardiac cycle ("cyclic variation") appears to be useful for characterizing both focal and diffuse cardiac pathologies. A recent literature search indicated that more than 350 refereed journal articles that utilize this method have been published.[1] Despite its success as a research tool, measurement of the cyclic variation of backscatter has not enjoyed widespread implementation as a mainstream clinical tool.

Among the factors limiting routine clinical use is the fact that the generation of cyclic variation data is still a relatively time-intensive process. Data from a specific cardiac region are obtained by manually positioning a region-of-interest within the myocardium for each frame of the recorded echocardiographic images over several heart cycles. However, recent enhancements of echocardiographic image analysis systems, including region-of-interest tracking based on speckle tracking methods, may facilitate expanded use of cyclic variation of backscatter measurements by reducing the amount of operator time needed to acquire and analyze the data.

Despite the potential of cyclic variation, as demonstrated by previous animal model and human studies, its clinical relevance might be questioned due to the emergence of methods of tissue characterization utilizing regional strain and strain rate. These methods have also been automated to a significant extent, a development that has spurred their clinical deployment. Relatively few studies have examined the potential relationship between cyclic variation of backscatter and myocardial strain.[2-5] Examination of the literature suggests that cyclic variation and strain-derived information may be complementary rather than duplicative. In segments of myocardium stunned as a result of reversible ischemic injury, for example, cyclic variation of backscatter has been demonstrated to recover significantly earlier than regional myocardial thickening in both animal laboratory and patient studies.[6-9]

Data comparing the reproducibility of cyclic variation and strain methods in the same patient population are not available. Before such direct comparisons designed to assess the strengths and limitations of both approaches can be undertaken, a consistent and reliable method for the analysis of the cyclic variation of backscatter must be available. To appreciate the diverse methods employed for quantifying the magnitude of cyclic variation, one can examine studies from representative laboratories.[2, 9-32] The goals of this study are to examine approaches employed for characterizing the cyclic variation of backscatter and to demonstrate and validate an improved automated method for determining the magnitude of cyclic variation of backscatter. Data acquired from 23 subjects are employed to illustrate an approach for reconciling differences among published data.

Methods

Patient Population

To obtain cyclic variation measurements over a wide range of values, the subject population for this study was drawn from patients who had been referred to the Cardiac Procedure Center for elective, diagnostic cardiac catheterization at Washington University Medical Center's Barnes-Jewish Hospital in Saint Louis, Missouri. These subjects (n = 23, which represented the entire available, consecutively-drawn subject population at the time this study was conducted) were scheduled for the procedure at the request of their referring cardiologist to diagnose the presence of coronary artery disease as a consequence of a positive result from a cardiac stress test or for screening as part of cardiac transplant evaluation. These subjects had previously agreed to participate in a study involving diagnostic catheterization with simultaneous echocardiography in accordance with informed consent procedures approved by the Washington University Medical Center Human Research Protection Office, with this study collecting data during the simultaneous echocardiographic procedure. This approach for subject selection provided individuals with a range of cardiac disorders, including both focal and diffuse pathologies, as well as some with clinically normal cardiac function. Data were collected during an echocardiographic examination and analyzed using the methods described below to determine the magnitude of cyclic variation present.

Acquisition of Data from Clinical Echocardiogram

The echocardiographic imaging system employed in this study was the Philips iE33 (Philips, Andover, MA) utilizing a S5-1 probe in harmonic imaging mode. Data

were collected in the parasternal long-axis view of the heart to avoid any potential influence of myocardial anisotropy.[31-34] Due to limitations imposed by the setting, subjects were imaged in the supine, rather than the left lateral decubitus position, as is customary. A potential disadvantage of this limitation was that shadowing of the heart by the lungs could be present, although by careful manipulation of the transducer the effects of shadowing could be shifted away from the region of interest to be investigated.

For each subject, an experienced sonographer acquired the echocardiographic data. Prior to acquisition, the imaging system was configured using the specially selected settings described in Appendix 2, in a manner similar to that employed and discussed in other studies. In addition, time gain compensation was set to a constant value for all depths, and lateral gain compensation was set to a constant value for all lateral regions. An optimal range of overall gain settings was determined visually for each subject. This configuration permitted the determination of the mean backscatter in decibels (dB) from a region of interest based on the mean grayscale value of the image.[3]

Determination of the Magnitude of Cyclic Variation

As a first step, the backscatter waveforms, such as those illustrated in panel a) of Figure 5-1, were analyzed manually for each heart cycle by four experienced members of this Laboratory. Each member generated manual estimates of the magnitude of cyclic variation by estimating, by hand, the average variation present for a given heart cycle, under the premise that the backscatter alternates between a high and a low level as illustrated in panel b) of Figure 5-1. Data from specific heart cycles were excluded from

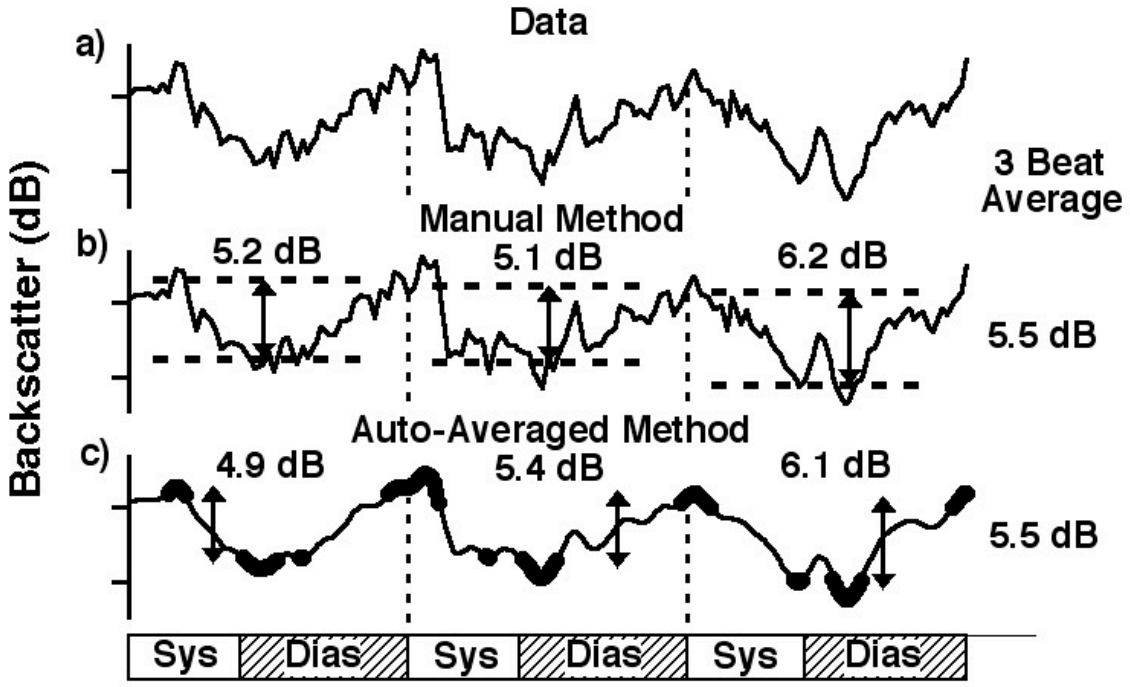

Figure 5-1: Backscatter in decibels (dB) shown over three cardiac cycles of a specific patient. a) Unprocessed data. b) Results of manual determination of the magnitude of the cyclic variation of backscatter by four experienced observers. c) Results obtained using the newly introduced auto-averaged method.

further analysis if it was not possible to distinguish the cyclic variation from random clutter or specific image artifacts (such as transient shadowing by the lungs) that created corresponding artifacts in the data.[32, 35] These artifactual beats were excluded so that the cyclic variation of the underlying myocardium could be accurately assessed. The manual estimate of magnitude reported for each of the 72 heart cycles that were included was computed as the average of the magnitudes obtained by the four observers, and ranged from a low of 2 dB to a high of 10 dB.

To assess the reproducibility of manual analysis, inter-operator and intra-operator errors were evaluated. To estimate intra-operator error, each of the four observers repeated his or her determination of the magnitude of cyclic variation, and the results

were compared to initial estimates that had been carried out a minimum of one month earlier. The difference between the two estimates was computed for each heart cycle, and the intra-operator error was calculated as the standard deviation of this difference. The total (inter- and intra-operator) error for the manual estimate was then calculated via propagation of error, with a negligible covariance found between any two operators. The total error in the manual estimate was 0.42 dB.

The magnitude of cyclic variation was also determined using three automated algorithms. The newly developed automated average or "auto-averaged" algorithm, details of which are described in Appendix 2, makes use of smoothed data, and determines an average high and low level of backscatter by finding the average around the highest and lowest values of backscatter. The difference between these averaged high and averaged low values defines the magnitude of cyclic variation, as illustrated in panel c) of Figure 5-1. This smoothing and averaging approach mitigates the effects of clutter-induced variations on the measurement of the underlying cyclic variation of backscatter. For the model-fit approach, a previously described[14, 35] algorithm, the details of which are indicated in Appendix 2, was employed. The peak-to-peak analysis method was implemented by determining the maximum and minimum of the (unfiltered) backscatter data, with the magnitude of cyclic variation defined by the difference between these values.[20-27]

Results

The ability of the new auto-averaged algorithm to reproduce the results obtained by experienced observers is illustrated in Figure 5-2. The plot in panel a) compares the

magnitude of cyclic variation estimated by the auto-averaged method with that obtained by the experienced observers for each heart cycle analyzed. Excellent agreement is seen between the two methods, with a high degree of correlation ($r = 0.96$). The difference between the reported values of the two different estimators is plotted against the average of the reported values using the Bland-Altman approach in panel b). The standard deviation in the difference between the methods is 0.48 dB, which is essentially identical to that for the manual estimate alone (0.42 dB), confirming the success of the auto-averaged approach.

In order to explore differences between methods of analysis employed by different laboratories, cyclic variation data from a selected patient is presented in Figure 5-3, with the corresponding results for all 23 patients shown in Figure 5-4. Data presented in Figure 5-3 illustrate a case in which the peak-to-peak algorithm yields a magnitude of cyclic variation noticeably larger, and the model fit algorithm yields a value of cyclic variation that is smaller, than the auto-averaged method. Figure 5-4 panel a) illustrates the relationship between the peak-to-peak method and the auto-averaged method for all 23 patients. Figure 5-4 panel b) shows the corresponding relationship between the model-fit method and the auto-averaged method.

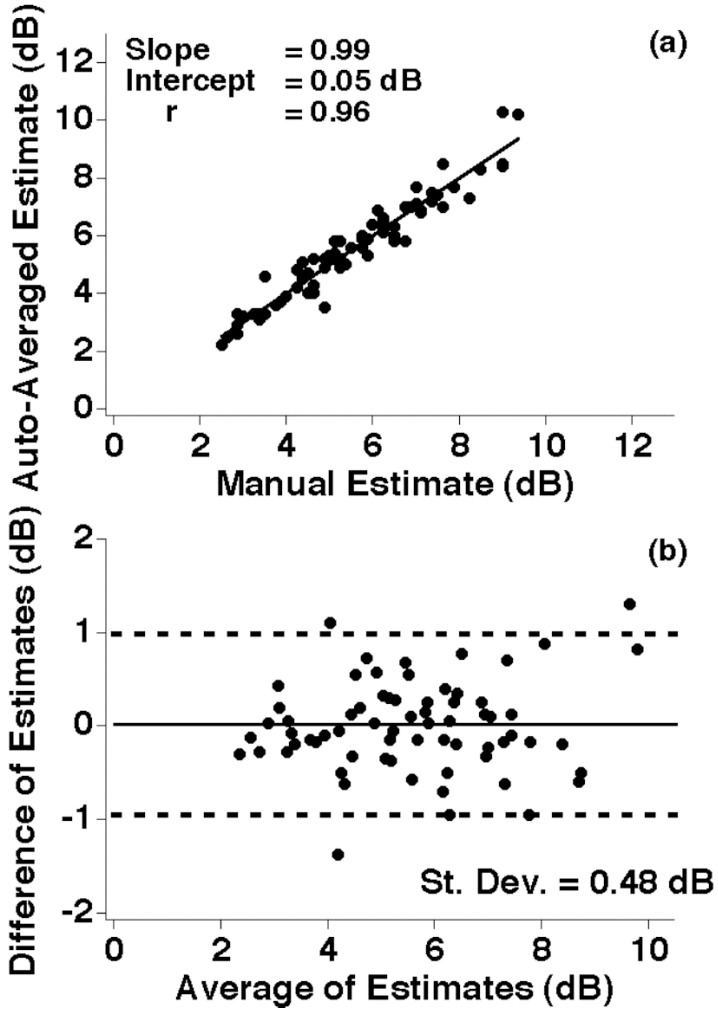

Figure 5-2: a) A comparison of the magnitude of cyclic variation as estimated by the auto-averaged method and the manually estimated values for all 23 patients. b) A Bland-Altman analysis of the magnitude of cyclic variation as estimated by the manual and auto-averaged methods. The dashed lines illustrate the value for twice the standard deviation.

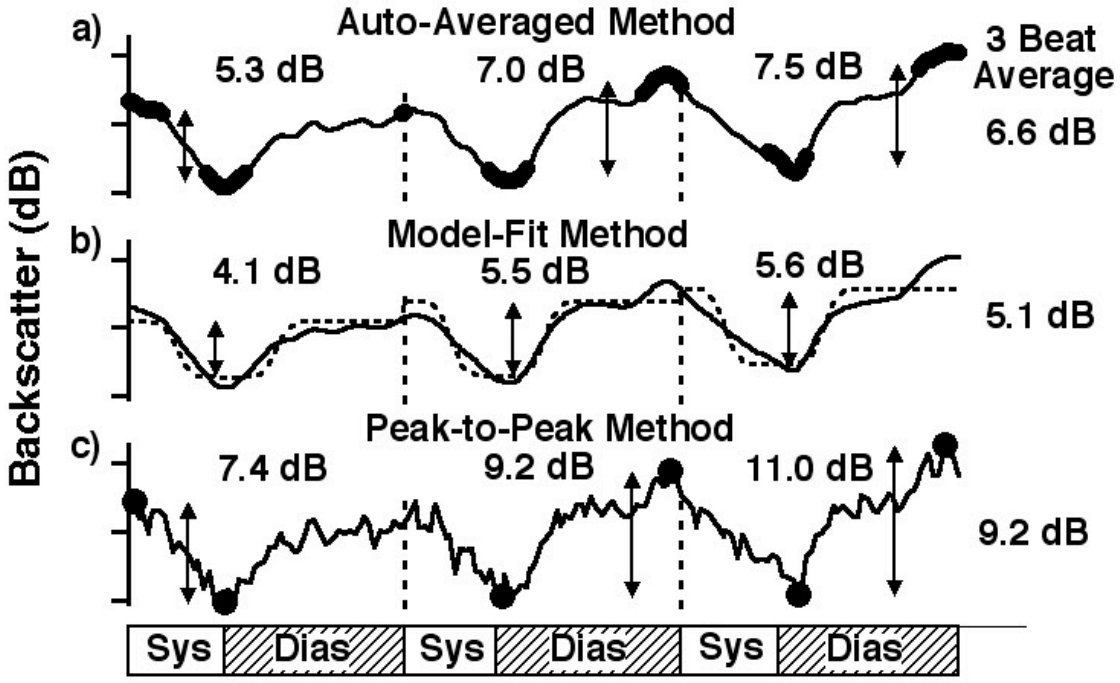

Figure 5-3: Backscatter in decibels (dB) shown over three cardiac cycles for one patient, subjected to a) auto-averaged analysis, b) model-fit analysis, and c) peak-to-peak analysis.

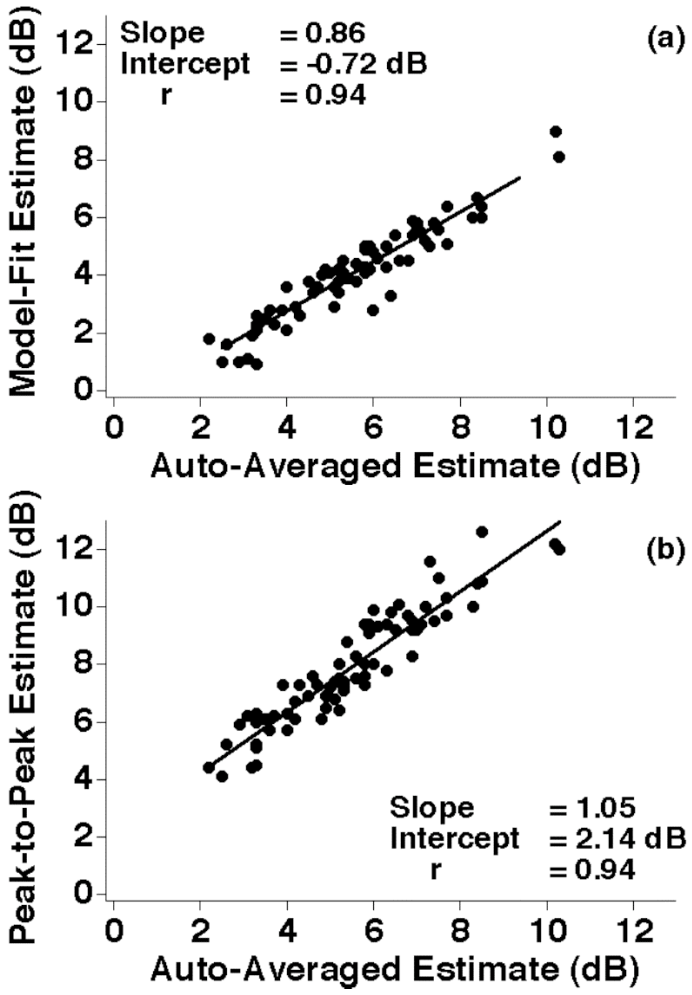

Figure 5-4: a) A comparison of the results of determining the magnitude of cyclic variation with the model-fit method with those obtained using the auto-averaged method. b) A comparison of the results obtained with the peak-to-peak method with those obtained using the auto-averaged method.

Discussion

The hypothesis underlying the present study is that apparent disagreement among values reported for the magnitude of cyclic variation of backscatter may be attributable to the distinct approaches employed by different investigators. Figures 5-3 and 5-4 permit comparisons of representative methods of analysis for studies of the same heart cycles of 23 patients whose magnitudes of cyclic variation cover a wide range. The lines of best fit from Figure 5-4 permit a calculation of the expected magnitude of cyclic variation

anticipated using the peak-to-peak or model-fit relative to those obtained with the auto-averaged method. As an illustration, for a magnitude of cyclic variation of 6.6 dB as determined by the auto-averaged method in Figure 5-3 panel a), the equation for the line of best fit with the model fit method from Figure 5-4 panel a) suggests that the expected magnitude, as measured by the model-fit approach, would be 0.86 * 6.6 dB – 0.72 dB, which equals 5.0 dB. This is essentially identical to the value of 5.1 dB shown in panel b) of Figure 5-3. A similar calculation for the peak-to-peak method (1.05 * 6.6 dB + 1.05 dB) would produce an expected value of 9.1 dB which is essentially identical to the value of 9.2 dB shown in panel c) of Figure 5-3. These differing estimates (for the same underlying data set from the parasternal long-axis view, in the posterior wall of the left ventricle) illustrate that the range of values seen in the literature among laboratories might arise primarily because of differences in the methods of analysis employed.[2, 6, 21, 32, 33]

The auto-averaged approach introduced here seems likely to offer improved performance over earlier methods. Estimates of magnitude arising from the peak-to-peak approach are susceptible to the random variations inherent to the clutter of an image, which can be misinterpreted as an erroneous increase in the total peak to valley magnitude of the waveform. The auto-averaged approach is less sensitive than the peak-to-peak method to such variations in the image clutter level. The rectangular model fit approach can underestimate the magnitude of cyclic variation (relative to that determined by the auto-averaged method or by the manual estimate of experienced observers) when the shape of the model function is not well matched with the shape of the data. The auto-averaged method is less sensitive to the specific shape of the cyclic variation of backscatter data over the heart cycle and works well when only estimates of the

magnitude are desired. Enhanced analyses using model-based approaches may benefit from utilizing model functions that are better matched with the shape of the data.[15]

An examination of the correlation plots shown in Figure 5-4 permits one to appreciate the overall relationship among the three methods of analysis. These relationships, as well as the relatively strong correlation values for the linear fit as shown, indicate that mean values for data analyzed with one method can be transformed into "hypothetical" data for another method, using the line of best fit as an equation of transformation. Further, for two data sets that are statistically significantly different (for example, a normal and a pathologic study population), the transformation from one method to another in this manner should preserve the statistical significance between the populations in the new method. This can be demonstrated by applying the transformation to the data acquired in this study. Figure 5-5 illustrates a histogram for two study populations: the population labeled "group A" is the full data set collected in this study for the model-fit approach, while the population labeled "group B" is an artificially generated data set, with a mean that is 2 dB higher than the group A population but with approximately the same standard deviation. By construction, these populations are significantly different, which can be verified using the Student t-test. The line of best fit from Figure 5-4, panel a), can be directly applied to each of the underlying data points for both populations to generate the expected results for the auto-averaged approach. The histograms for the results of this transformation are found in Figure 5-6. Because the transformation is composed of a shift as well as a stretch, the histograms are shifted to the

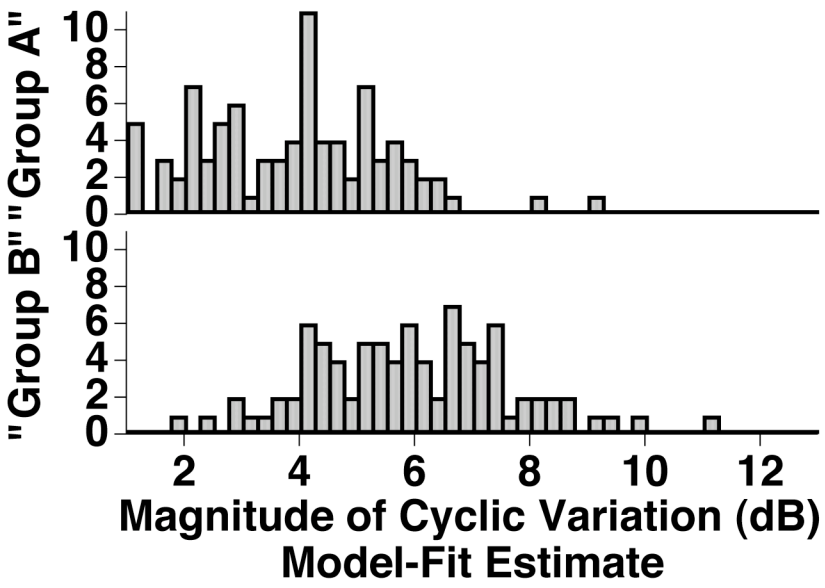

Figure 5-5: A histogram representation of the data collected from this study for the model-fit approach. The population listed as "Group A" is the actual data collected, while the "Group B" population was generated using the "Group A" mean plus two dB, and a random Gaussian factor with the same width as the "Group A" population.

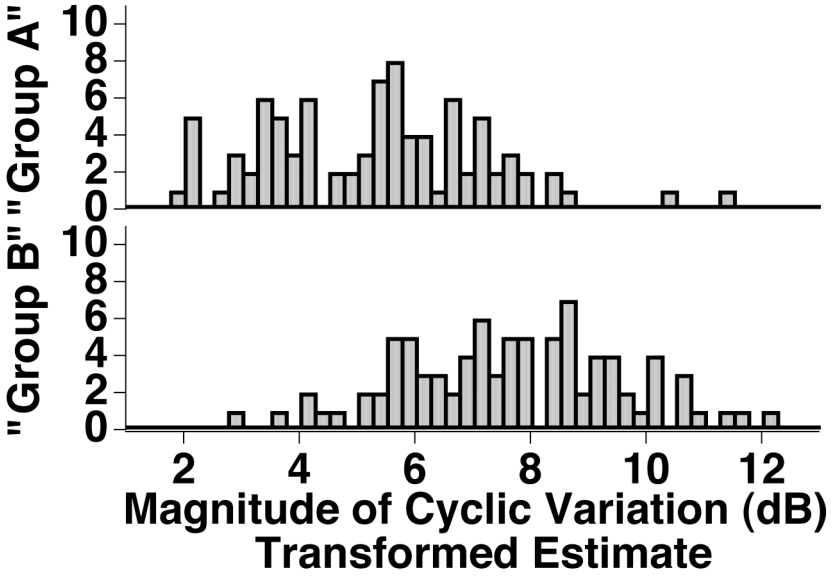

Figure 5-6: The result of a linear transformation of the data that composes Figure 5-5. The "Group A" population is the original model-fit approach's data (transformed by the equation of a line of best fit from Figure 5-4 a), and the "Group B" population shown is the transformation of the "Group B" data from Figure 5-5.

right (an increase in expected measured values) as well as stretched slightly. A reapplication of the t-test between the populations, however, reveals no difference in the statistical significance between the populations after the application of this transformation. Thus, an investigator with data collected using the model-fit method would be able to predict reliably how the average value of the magnitude of cyclic variation would change if the analysis had been performed instead using the peak-to-peak method, due to the shift from the transformation. Further, if two populations were of interest (again, say, a "clinically normal" versus a "non-normal" population), an observed difference in cyclic variation between these populations does not depend on the method used to calculate the cyclic variation. This conclusion permits a retrospective look at the results of published data from different laboratories that have employed different methods of generating the magnitude of cyclic variation, even in the absence of the underlying raw data. The considerations outlined above are in agreement with those of van der Steen *et. al.*[16] and indicate that the choice of the specific method of analysis (model-fit, peak-to-peak, or auto-averaged) employed by an investigator will not affect the statistical significance of a study.

One limitation of this study is that only 23 patients were studied. However, the central concern was to acquire a range of data that would span the range of clinically relevant values of magnitude of cyclic variation. That was accomplished with 23 patients imaged in the supine position from a single echocardiographic view. These choices were appropriate for the goal of this investigation, but would be inappropriate if the goal had been to characterize a specific pathology. Superficially, it might appear that the use of a single region of interest, as opposed to multiple segments from several echocardiographic

views, would represent a limitation of this work. However, the goal of the study is focused on the methods of analysis, and again, the only requirement was that the data cover a wide range of values for the magnitude of cyclic variation of backscatter, a feature that is independent of the details of the location within the heart.

In summary, the present work introduced an improved analysis algorithm and demonstrated that apparent disagreements in the published literature are likely to be attributable to the distinct approaches employed by different investigators. The approach outlined provides a systematic means for standardizing results from all laboratories, thus facilitating potential comparisons between studies obtained using the cyclic variation of myocardial backscatter and results derived, for example, from strain-related approaches.

References

1. Barzilai, B., M.R. Holland, B.R. Lindman, and J.G. Miller, Progress in myocardial tissue characterization based on the cyclic variation of backscatter. Ultrasonic Imaging 2009;31:54-55.
2. D'Hooge, J., B. Bijnens, F. Jamal, C. Pislaru, S. Pislaru, J. Thoen, et al., High frame rate myocardial integrated backscatter. Does this change our understanding of this acoustic parameter? Eur J Echocardiogr 2000;1(1):32-41.
3. Holland, M.R., A.A. Gibson, C.A. Kirschner, D. Hicks, A. Ludomirsky, and G.K. Singh, Intrinsic myoarchitectural differences between the left and right ventricles of fetal human hearts: an ultrasonic backscatter feasibility study. J Am Soc Echocardiogr 2009;22(2):170-6.
4. Madaras, E.I., B. Barzilai, J.E. Perez, B.E. Sobel, and J.G. Miller, Changes in myocardial backscatter throughout the cardiac cycle. Ultrasonic Imaging 1983;5(3):229-39.
5. Thomas, L.J., S.A. Wickline, J.E. Perez, B.E. Sobel, and J.G. Miller, A real-time integrated backscatter measurement system for quantitative cardiac tissue characterization. IEEE Trans Ultrason Ferroelectr Freq Control 1986;33(1):27-32.
6. Milunski, M.R., G.A. Mohr, J.E. Perez, Z. Vered, K.A. Wear, C.J. Gessler, et al., Ultrasonic tissue characterization with integrated backscatter. Acute myocardial ischemia, reperfusion, and stunned myocardium in patients. Circulation 1989;80(3):491-503.

7. Milunski, M.R., G.A. Mohr, K.A. Wear, B.E. Sobel, J.G. Miller, and S.A. Wickline, Early identification with ultrasonic integrated backscatter of viable but stunned myocardium in dogs. J Am Coll Cardiol 1989;14(2):462-71.

8. Vandenberg, B.F., J.E. Stuhlmuller, L. Rath, R.E. Kerber, S.M. Collins, H.E. Melton, et al., Diagnosis of recent myocardial infarction with quantitative backscatter imaging: preliminary studies. J Am Soc Echocardiogr 1991;4(1):10-8.

9. Hancock, J.E., J.C. Cooke, D.T. Chin, and M.J. Monaghan, Determination of successful reperfusion after thrombolysis for acute myocardial infarction: a noninvasive method using ultrasonic tissue characterization that can be applied clinically. Circulation 2002;105(2):157-61.

10. Barzilai, B., E.I. Madaras, B.E. Sobel, J.G. Miller, and J.E. Perez, Effects of myocardial contraction on ultrasonic backscatter before and after ischemia. Am J Physiol 1984;247(3 Pt 2):H478-83.

11. Mottley, J.G., R.M. Glueck, J.E. Perez, B.E. Sobel, and J.G. Miller, Regional differences in the cyclic variation of myocardial backscatter that parallel regional differences in contractile performance. J Acoust Soc Am 1984;76(6):1617-23.

12. Vered, Z., B. Barzilai, G.A. Mohr, L.J. Thomas, 3rd, R. Genton, B.E. Sobel, et al., Quantitative ultrasonic tissue characterization with real-time integrated backscatter imaging in normal human subjects and in patients with dilated cardiomyopathy. Circulation 1987;76(5):1067-73.

13. Perez, J.E., J.B. McGill, J.V. Santiago, K.B. Schechtman, A.D. Waggoner, J.G. Miller, et al., Abnormal myocardial acoustic properties in diabetic patients and

their correlation with the severity of disease. J Am Coll Cardiol 1992;19(6):1154-62.

14. Mobley, J., C.E. Banta, H.M. Gussak, J.E. Perez, and J.G. Miller, Clinical Tissue Characterization: Online Determination of Magnitude and Time Delay Myocardial Backscatter. Video Journal of Echocardiography 1995;5(2):40-48.

15. Vitale, D.F., R.O. Bonow, G. Gerundo, N. Pelaggi, G. Lauria, D. Leosco, et al., Alterations in ultrasonic backscatter during exercise-induced myocardial ischemia in humans. Circulation 1995;92(6):1452-7.

16. van der Steen, A.F.W., H. Rijsterborgh, C.T. LancÈe, F. Mastik, R. Krams, P.D. Verdouw, et al., Influence of data processing on cyclic variation of integrated backscatter and wall thickness in stunned porcine myocardium. Ultrasound in Medicine & Biology 1997;23(3):405-414.

17. Takiuchi, S., H. Ito, K. Iwakura, Y. Taniyama, N. Nishikawa, T. Masuyama, et al., Ultrasonic tissue characterization predicts myocardial viability in early stage of reperfused acute myocardial infarction. Circulation 1998;97(4):356-62.

18. Di Bello, V., R. Pedrinelli, A. Bertini, D. Giorgi, E. Talini, G. Dell'Omo, et al., Cyclic variation of the myocardial integrated backscatter signal in hypertensive cardiopathy: a preliminary study. Coron Artery Dis 2001;12(4):267-75.

19. Giglio, V., V. Pasceri, L. Messano, F. Mangiola, L. Pasquini, A. Dello Russo, et al., Ultrasound tissue characterization detects preclinical myocardial structural changes in children affected by Duchenne muscular dystrophy. J Am Coll Cardiol 2003;42(2):309-16.

20. Masuyama, T., F.G. St Goar, T.L. Tye, G. Oppenheim, I. Schnittger, and R.L. Popp, Ultrasonic tissue characterization of human hypertrophied hearts in vivo with cardiac cycle-dependent variation in integrated backscatter. Circulation 1989;80(4):925-34.

21. Iliceto, S., L. Galiuto, P. Colonna, V.F. Napoli, and P. Rizzon, Effects of atrial pacing stress test on ultrasonic integrated backscatter cyclic variations in normal subjects and in patients with coronary artery disease. Eur Heart J 1997;18(10):1590-8.

22. Yuda, S., J. Dart, O. Najos, and T.H. Marwick, Use of cyclic variation of integrated backscatter to assess contractile reserve and myocardial viability in chronic ischemic left ventricular dysfunction. Echocardiography 2002;19(4):279-87.

23. Hu, X., J. Wang, Y. Sun, X. Jiang, B. Sun, H. Fu, et al., Relation of ultrasonic tissue characterization with integrated backscatter to contractile reserve in patients with chronic coronary artery disease. Clin Cardiol 2003;26(10):485-8.

24. Iwakura, K., H. Ito, S. Kawano, A. Okamura, K. Asano, T. Kuroda, et al., Detection of TIMI-3 flow before mechanical reperfusion with ultrasonic tissue characterization in patients with anterior wall acute myocardial infarction. Circulation 2003;107(25):3159-64.

25. Komuro, K., S. Yamada, T. Mikami, K. Yoshinaga, K. Noriyasu, K. Goto, et al., Sensitive detection of myocardial viability in chronic coronary artery disease by ultrasonic integrated backscatter analysis. J Am Soc Echocardiogr 2005;18(1):26-31.

26. Ohara, Y., Y. Hiasa, S. Hosokawa, N. Suzuki, T. Takahashi, K. Kishi, et al., Ultrasonic tissue characterization predicts left ventricular remodeling in patients with acute anterior myocardial infarction after primary coronary angioplasty. J Am Soc Echocardiogr 2005;18(6):638-43.

27. Micari, A., M. Pascotto, A.R. Jayaweera, J. Sklenar, N.C. Goodman, and S. Kaul, Cyclic variation in ultrasonic myocardial integrated backscatter is due to phasic changes in the number of patent myocardial microvessels. J Ultrasound Med 2006;25(8):1009-19.

28. Fijalkowski, M., A. Koprowski, M. Gruchala, R. Galaska, A. Debska-Slizien, J. Rogowski, et al., Effect of preload reduction by hemodialysis on myocardial ultrasonic characterization, left atrial volume, and Doppler tissue imaging in patients with end-stage renal disease. J Am Soc Echocardiogr 2006;19(11):1359-64.

29. Di Bello, V., F. Santini, A. Di Cori, A. Pucci, E. Talini, C. Palagi, et al., Effects of bariatric surgery on early myocardial alterations in adult severely obese subjects. Cardiology 2008;109(4):241-8.

30. Losi, M.A., S. Betocchi, M. Chinali, G. Barbati, G. D'Alessandro, A. Cacace, et al., Myocardial texture in hypertrophic cardiomyopathy. J Am Soc Echocardiogr 2007;20(11):1253-9.

31. Vandenberg, B.F., L. Rath, T.A. Shoup, R.E. Kerber, S.M. Collins, and D.J. Skorton, Cyclic variation of ultrasound backscatter in normal myocardium is view dependent: clinical studies with a real-time backscatter imaging system. J Am Soc Echocardiogr 1989;2(5):308-14.

32. Finch-Johnston, A.E., H.M. Gussak, J. Mobley, M.R. Holland, O. Petrovic, J.E. Perez, et al., Cyclic variation of integrated backscatter: dependence of time delay on the echocardiographic view used and the myocardial segment analyzed. J Am Soc Echocardiogr 2000;13(1):9-17.

33. Finch-Johnston, A.E., H.M. Gussak, J. Mobley, M.R. Holland, O. Petrovic, J.E. Perez, et al., Dependence of "apparent" magnitude on the time delay of cyclic variation of myocardial backscatter. Ultrasound Med Biol 1999;25(5):759-62.

34. Recchia, D., J.G. Miller, and S.A. Wickline, Quantification of ultrasonic anisotropy in normal myocardium with lateral gain compensation of two-dimensional integrated backscatter images. Ultrasound in Medicine & Biology 1993;19(6):497-505.

35. Mohr, G.A., Z. Vered, B. Barzilai, J.E. Perez, B.E. Sobel, and J.G. Miller, Automated determination of the magnitude and time delay ("phase") of the cardiac cycle dependent variation of myocardial ultrasonic integrated backscatter. Ultrasonic Imaging 1989;11(4):245-59.

Chapter 6: A Relationship Between the Cyclic Variation of Myocardial Backscatter and Diastolic Function, Using the Parametrized Diastolic Filling Formalism

Background

Myocardial tissue characterization represents an extension of currently available echocardiographic imaging. Measurements of the systematic variation of backscattered energy during the cardiac cycle (known as the cyclic variation of backscatter) provide an approach for myocardial characterization.[1] Changes in the pattern of cyclic variation of backscattered ultrasonic energy from a region of myocardium have been studied in a wide range of cardiac pathologies.[2-8] The results of these studies indicate that the cyclic variation of backscatter can be used to monitor changes in the underlying structural and elastic properties of the myocardium. Although a number of studies have described mechanisms thought to contribute to cyclic variation, a complete understanding of the underlying factors responsible for the cyclic variation of backscatter has not been achieved.[9-11]

Another characterization approach, known as the parametrized diastolic filling formalism, is an established kinematic approach for modeling the diastolic function of the heart, using information derived from Doppler measurements of blood flow through the mitral valve.[12] This formalism accounts for the mechanical suction-pump role of the left ventricle by applying a damped harmonic oscillator model to characterize the Doppler transmitral velocity profiles corresponding to the early rapid filling wave (E-wave) and

the subsequent late filling wave (A-wave) driven by atrial contraction. The parameters of the parametrized diastolic filling model have physiologic analogues that have been experimentally validated in-vivo,[13-16] and have also been tested and validated in subjects with a wide range of cardiac pathologies, such as heart failure, hypertension and diabetes.[13, 17-20]

The quantity and forcefulness of blood delivered to the peripheral circulation during systole is highly dependent upon the diastolic filling that precedes that systolic contraction (the Frank-Starling mechanism). Furthermore, diastolic dysfunction precedes systolic dysfunction in many cardiac pathologies.[21, 22] These suggest that relating results obtained with the parametrized diastolic filling formalism to measurements of the cyclic variation of backscatter may represent an approach for determining the role of diastolic function in the observed cyclic variation of backscatter. The hypothesis underlying this work is that the dynamic viscoelastic properties of the myocardium that influence diastolic function are likely to be reflected in the cyclic variation of backscatter. The goal of this study of 32 subjects was to elucidate and characterize the impact of diastolic function on the cyclic variation of backscatter by employing the parametrized diastolic filling formalism for diastolic function quantitation.

Methods

Subject Population

Subjects for this study were recruited from patients who had been referred for elective, diagnostic cardiac catheterization to the Cardiac Procedure Center at Washington University Medical Center's Barnes-Jewish Hospital in Saint Louis,

Missouri. These subjects (n = 32) were scheduled for elective diagnostic cardiac catheterization to rule out the presence of coronary artery disease at the request of their referring physician. All subjects provided informed consent prior to the procedure in accordance with a protocol approved by the Barnes-Jewish Hospital/Washington University Human Research Protection Office. The inclusion criteria included normal valvular function, no acute ischemia, and no significant merging between echocardiographic E- and A-waves. Subjects with issues that would make the acquisition of data untenable, such as poor echocardiographic windows, tachycardia, or significant mitral regurgitation or aortic stenosis, were excluded.

Clinical Data Acquisition

The simultaneous echocardiography-cardiac catheterization procedure utilized for acquisition of the data has been previously described.[13] Prior to catheterization, a complete echocardiographic examination was performed on the subject in the catheterization laboratory, using a Philips iE33 echocardiographic imaging system (Andover, MA, USA) in accordance with ASE guidelines.[23] This examination was performed by a certified sonographer and included 2-D and 3-D imaging of the heart in standard views, as well as Doppler tissue and flow characterization. The examination results were used to determine the eligibility of the subject, as noted above. Due to limitations imposed by the setting, the subject was imaged in the supine, rather than the left lateral decubitus position. This position has the potential disadvantage of introducing additional visual artifacts, but these artifacts can be minimized or eliminated through careful manipulation of the transducer. In addition, the configuration of the imaging

system was such that the grayscale displayed was nearly linearly related to the received signal, to allow for the accurate measurement of cyclic variation. The configuration for the iE33 system was determined to be nearly linear for the M1 grayscale map, with 40 dB compression, and the lateral and time gain compensation held constant. A further offline grayscale remapping was later applied to achieve linearity.

After the initial echocardiographic examination, arterial access was obtained via the femoral artery, and a 6-F micromanometer-tipped pigtail pressure-volume (conductance) catheter (Millar Instruments, Houston, TX, Model SPC 562) was directed into the left ventricle (LV) in a retrograde fashion across the aortic valve under fluoroscopic control. The ventricular pressures were fed to the catheterization laboratory amplifier (GE Healthcare, Fairfield, CT), and output simultaneously into the auxiliary input port of the echocardiographic imaging system and into a digital converter connected to a customized PC. Video clips consisting of several consecutive heartbeats (typically four) were first obtained for the parasternal long axis view, to be analyzed off-line to determine the cyclic variation from the posterior wall of the LV. The echocardiographic view was then shifted to the apical four-chamber view, and a Doppler sample volume, gated to a 1.5 to 2.5 mm depth, was placed between the tips of the mitral valve leaflets. With the Millar catheter in place, simultaneous pressure, volume and transmitral flow data were collected during the acquisition of approximately 25 to 50 consecutive cardiac cycles. Continuous Doppler data was recorded to DVD. To synchronize the hemodynamic and Doppler data, a fiducial square wave signal was fed from the catheter transducer control unit to both the echocardiographic imager and the PC. Following the acquisition of research data, the remainder of the diagnostic procedure was performed.

After the clinical study, the acquired ultrasonic and pressure-volume data were archived for subsequent, off-line analysis.

Determination of E-Wave Parameters

Triangle Approach

Each subject had an average of 10 to 20 cardiac cycles selected for quantitative analysis. Conventional triangle approximations of the E- and A-wave shapes[24, 25] provided the following parameters: E-wave acceleration and deceleration times (AT and DT) and duration (E_{dur}), and the E-wave and A-wave peaks (E_{peak}, A_{peak}) and velocity-time integrals (VTI_E, VTI_A). The ratio of E_{peak} to A_{peak} (E_{peak}/A_{peak}) and VTI_E to VTI_A (VTI_E/VTI_A) were also calculated for all heart cycles.

Parametrized Diastolic Filling Approach

The E-waves selected for each subject for the conventional triangle approximation to E-wave shape approach were also subjected to parametrized diastolic filling model-based image processing, which yielded specific mass-normalized kinematic model parameters (the relaxation/viscosity parameter *c (1/s)*, the stiffness parameter *k* $(1/s^2)$, and the initial load parameter x_o (*m*)) for each E-wave. These parametrized diastolic filling parameters were determined for an E-wave by solving the "inverse" problem, using the clinical E-wave contour as the input and the parameters as the output of a model that is fit to the contour.[26, 27] Briefly, the process of extracting these parameters from an individual wave involves selecting a single transmitral flow image, cropping the image around the Doppler velocity profile, and loading the cropped image into a custom LabVIEW

(National Instruments, Austin, TX) interface. Within the interface the E-wave maximum velocity envelope was digitized, and then a Levenberg-Marquardt algorithm[28] was applied to this envelope to extract the best-fit parametrized diastolic filling model parameters specific to the contour. This process is shown in Figure 6-1, for E-waves shapes well fit by underdamped and overdamped kinematic regimes. After the kinematic model parameters (c, k, and x_o) were determined, four composite indices with physiologic meaning were computed. These composite indices are: kx_0 (the peak driving force 14), $\frac{1}{2} kx_0^2$ (the initial potential energy available prior to mitral valve opening), $\beta = c^2 - 4k$ (an index of the balance between viscosity/relaxation and stiffness in the system[18, 19]), and $y = c / (2\sqrt{k})$ (a dimensionless damping to stiffness ratio, in which y = 1 separates the underdamped from the overdamped kinematic regime of motion[15]).

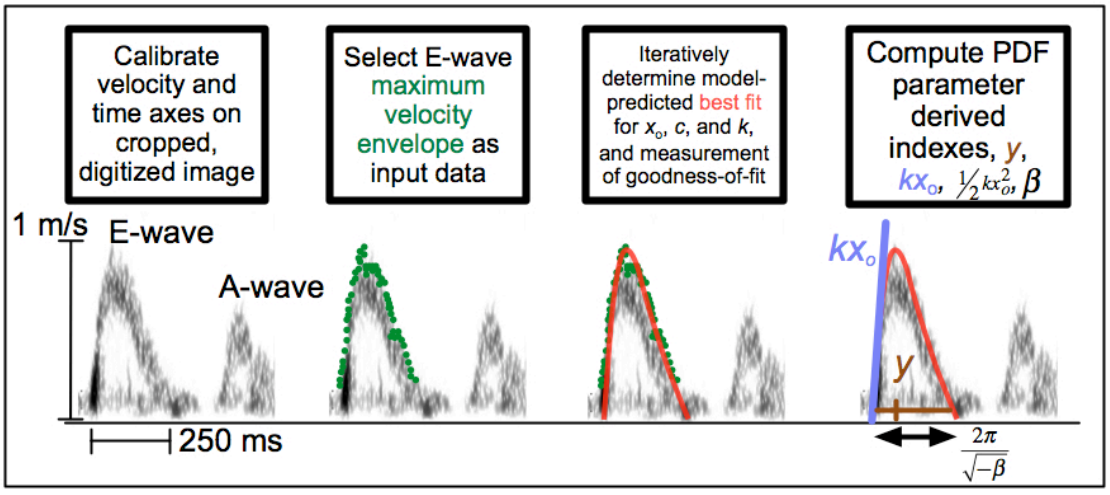

Figure 6-1: The Parametrized Diastolic Filling (PDF) model accurately predicts clinically recorded early rapid filling transmitral flow velocity (E-wave) contours. The model-predicted solution, based on the maximum velocity envelope, is shown, along with indices derived from the model parameters. See text for details.

Determination of Cyclic Variation Parameters

The data consisting of video clips in the parasternal long axis view were viewed using a DICOM reader (Osirix, available from http://www.osirix-viewer.com/) in a manner similar to that described in previous reports.[29] The grayscale for each video clip was remapped to achieve a linear relationship between the received power and the displayed grayscale. A region of interest was defined in the mid-myocardium of the posterior wall of the LV. This region of interest was manually adjusted in each frame of the video clip to ensure the same physical region was analyzed over the heart cycle. The mean grayscale value for this region of interest was determined for each frame. These grayscale values were then partitioned into individual heart cycles, using valve motion and ECG to determine the end of diastole.

The grayscale values over the duration of a single heartbeat were converted into backscatter values in dB using a linear conversion factor, and interpolated in time to 101 points, so that each point corresponds to a percentage of the heart cycle. The magnitude of cyclic variation was determined using an automated approach that closely replicates the values reported by experienced observers without the slight inherent operator variability,[30] and is illustrated for a sample data set in Figure 6-2. The backscatter values were smoothed with fifteen passes of a three-point binomial low-pass filter to minimize the effects of noise. The values for the top fifteen percent of the data were averaged, and likewise the values for the bottom fifteen percent of the data were averaged. The magnitude was calculated as the difference between the averaged high and averaged low values. The normalized time delay of cyclic variation was calculated by first manually determining the percentage of the heart cycle at which the nadir of cyclic variation was

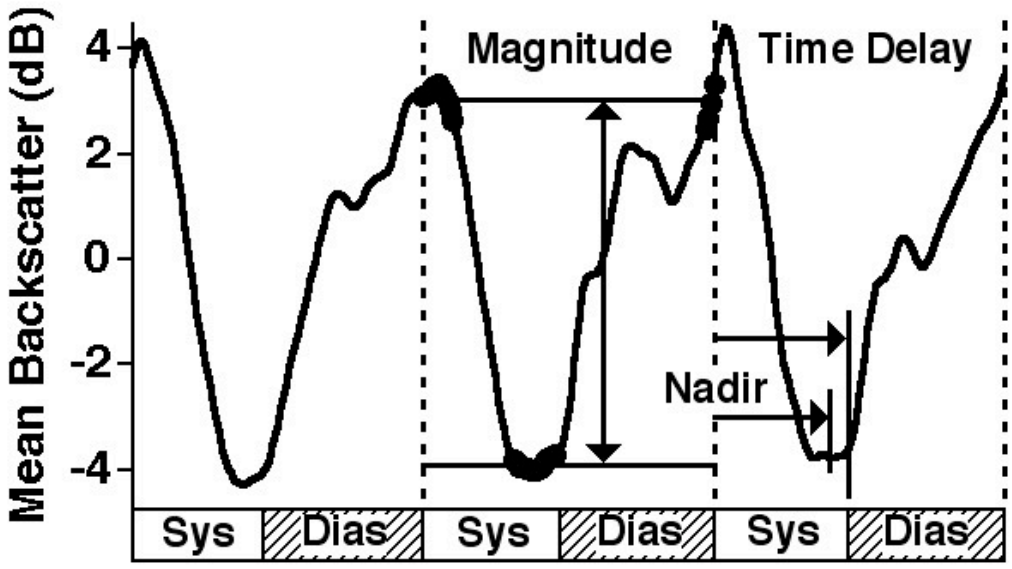

Figure 6-2. A smoothed sample data set of the backscatter from a region of interest over three heart cycles. The quantities required for the determination of the magnitude and the normalized time delay of cyclic variation are illustrated. See text for details.

found, and then dividing that value by the percentage of the heart cycle corresponding to systole. Once this analysis had been completed on all of the individual heart cycles for a specific subject, the overall magnitude and the normalized time delay of cyclic variation were computed as the average of these values across all heart cycles.

Comparisons Between Parameters

The E-wave and cyclic variation parameters were compared using linear correlation, in order to identify significant trends. Although none of the subjects had active ischemia at the time of data acquisition the presence of significant anatomical coronary artery disease, and its resulting effects on the myocardium, could potentially confound comparisons between parameters. To address this concern, the results of the clinical angiogram were used to divide the subject population into those with (n = 21) and

those without (n = 11) significant (>50% luminal diameter narrowing) coronary artery disease. Each correlation between a particular cyclic variation parameter and an E-wave parameter was first tested by performing an analysis of covariance (ANCOVA) with Matlab (The MathWorks, Inc., Natick, MA, USA), to determine if there existed a significant difference between the two populations. If a significant difference existed, then the populations could not be pooled; the populations were pooled for the remaining E-wave parameters. The appropriate line of regression was then tested for significance against the null hypothesis that the correlation coefficient was equal to zero.

Results

The ANCOVA results, for each pair of cyclic variation parameter to diastolic filling parameter, are indicated in Table 6-1. A significant difference was found for the E-wave parameters AT, c, k, and y. Accordingly for subsequent analyses the populations with and without coronary artery disease were not pooled when considering these three parameters.

Plots showing the comparisons of the normalized time delay of cyclic variation as a function of the parameters corresponding to myocardial function (E_{peak}, VTI_E, kx_0, and $\frac{1}{2} kx_0^2$), as measured by the parametrized diastolic filling formalism, are shown in Figures 6-3 and 6-4. A similar plot of the normalized time delay of cyclic variation versus both the index $\beta = c^2-4k$ (the relative influence of chamber stiffness vs. viscosity/relaxation) and the index $y = c/(2\sqrt{k})$ (a ratio for the damping and stiffness characteristics of the system) is shown in Figure 6-5.

	E-wave Shape Fit as a Triangle		**E-wave Shape Fit Via Parametrized Diastolic Filling Formalism**	
Diastolic Function Parameter/Index	**Magnitude**	**Time Delay**	**Magnitude**	**Time Delay**
AT	5.58*	6.28*	10.65**	9.37*
DT	0.01	0.05	3.62	3.43
E_{peak}	0.01	0.04	0.01	0.02
A_{peak}	1.44	1.32	1.50	1.40
VTI_E	0.05	0.23	0.08	0.01
VTI_A	3.37	3.14	2.34	2.29
E_{peak}/A_{peak}	1.70	1.54	1.85	1.72
VTI_E/VTI_A	2.04	1.87	2.23	2.02
c	---	---	10.31**	11.75**
k	---	---	4.65*	4.66*
$c^2 - 4k$	---	---	1.04	2.07
$c / (2\sqrt{k})$	---	---	6.87*	9.04**
kx_0	---	---	3.61	3.86
$\frac{1}{2} kx_0^2$	---	---	1.79	1.68

Table 6-1: Results of the ANCOVA test for significance between populations with and without coronary artery disease. Listed are the F-values for significance between the regression lines for each population, for the variables listed. * - $p < 0.05$, ** - $p < 0.01$.

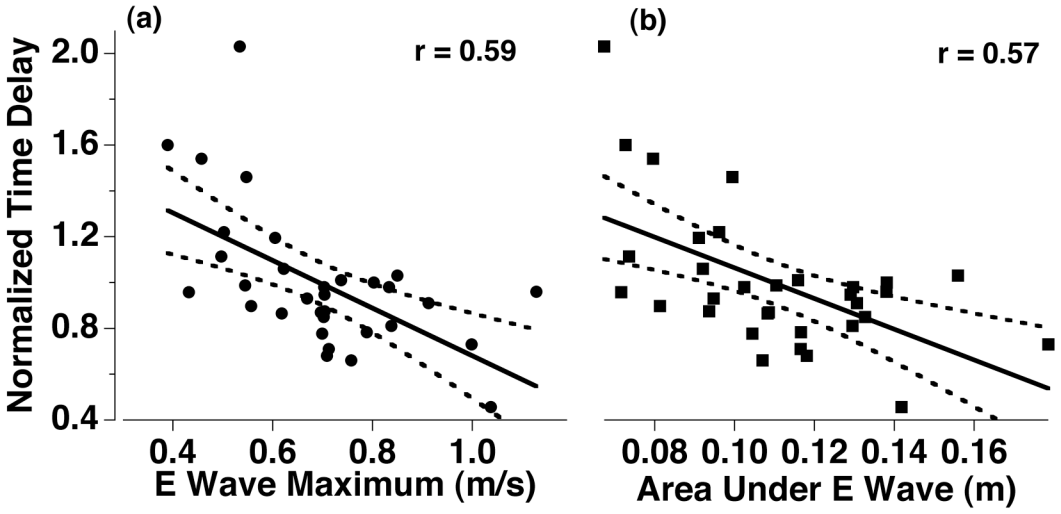

Figure 6-3: Comparisons of the normalized time delay of cyclic variation to E-wave parameters: a) the maximum of the E-wave (in m s^{-1}), and b) the area under the E-wave (in m), as determined with the parametrized diastolic filling formalism. The lines of best fit are a) y = -1.04(s m^{-1})x + 1.72, and b) y = -6.70(m^{-1})x + 1.73. The 95% confidence interval for the regression lines are displayed as dashed lines. See text for details.

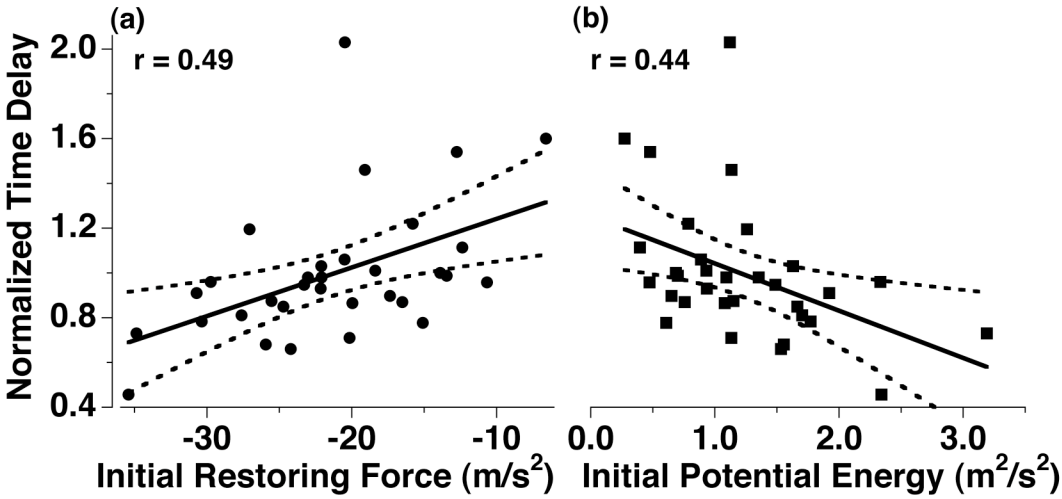

Figure 6-4: Comparisons of the normalized time delay of cyclic variation to parametrized diastolic filling parameter derived indices: a) the initial restoring force kx_o (in m s^{-2}), b) the initial potential energy $1/2kx_o^2$ (in m^2 s^{-2}). The lines of best fit are a) y = 0.022(s^2 m^{-1})x + 1.46, and b) y = -0.21(s^2 m^{-2})x + 1.25. The 95% confidence interval for the regression lines are displayed as dashed lines. See text for details.

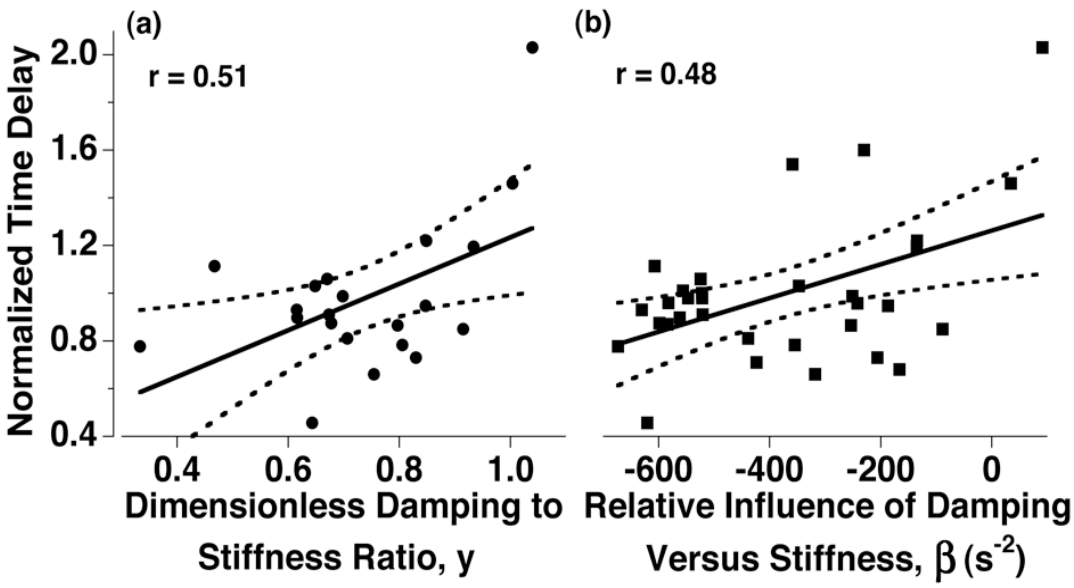

Figure 6-5: Comparisons of the normalized time delay of cyclic variation to parametrized diastolic filling parameter derived indices: a) dimensionless ratio of damping to stiffness $y = c / (2\sqrt{k})$ b) the relative effects of damping versus stiffness $\beta = c^2 - 4k$ (in s^{-2}). The lines of best fit are a) y = 0.97x + 0.26, and b) y = ($7.07 * 10^{-4}$ s^2)x + 1.26. The 95% confidence interval for the regression lines are displayed as dashed lines. See text for details.

The correlation values relating the normalized time delay of cyclic variation to all of the E-wave parameters and indices derived from them that correspond to function and viscoelasticity are summarized in Table 6-2. Likewise, the correlation values for the magnitude of cyclic variation against the E-wave parameters are summarized in Table 6-3.

Discussion

Continued improvements in echocardiographic imaging system technology are likely to encourage expanded use of methods for myocardial tissue characterization that complement information provided by real-time imaging and blood flow visualization. Such improvements include speckle tracking and automatic region-of-interest analysis,

		E-wave Shape Fit as a Triangle		E-wave Shape Fit Via Parametrized Diastolic Filling Formalism	
Diastolic Function Parameter/Index	**Subject Group**	**r**	**p**	**r**	**p**
E_{peak}	All Subjects	0.58^{***}	0.00046	0.59^{***}	0.00040
A_{peak}	All Subjects	0.063	0.73	0.061	0.74
E_{peak}/A_{peak}	All Subjects	0.41^{*}	0.021	0.41^{*}	0.018
VTI_E	All Subjects	0.49^{**}	0.0045	0.57^{***}	0.00072
VTI_A	All Subjects	0.19	0.31	0.053	0.77
VTI_E/VTI_A	All Subjects	0.32	0.07	0.29	0.11
kx_0	All Subjects	---	---	0.49^{**}	0.0044
$½\ kx_0^2$	All Subjects	---	---	0.44^{*}	0.012
AT	Without CAD	0.49	0.13	0.59	0.056
AT	With CAD	0.29	0.21	0.001	0.997
DT	All Subjects	0.33	0.065	0.25	0.17
c	Without CAD	---	---	0.39	0.23
c	With CAD	---	---	0.35	0.12
k	Without CAD	---	---	0.60	0.052
k	With CAD	---	---	0.28	0.22
$c^2 - 4k$	All Subjects	---	---	0.48^{**}	0.0053
$c / (2\sqrt{k})$	Without CAD	---	---	0.17	0.62
$c / (2\sqrt{k})$	With CAD	---	---	0.51^{*}	0.018

Table 6-2: Correlation values and their corresponding p-values for the comparisons between the normalized time delay of cyclic variation and the E- and A-wave parameters corresponding to function and viscoelasticity. n = 32 for all subjects, n = 11 for subjects without CAD, and n = 21 for subjects with CAD. * - $p < 0.05$, ** - $p < 0.01$, *** - $p < 0.001$

		E-wave Shape Fit as a Triangle		E-wave Shape Fit Via Parametrized Diastolic Filling Formalism	
Diastolic Function Parameter/Index	**Subject Group**	**r**	**p**	**r**	**p**
E_{peak}	All Subjects	0.11	0.55	0.079	0.67
A_{peak}	All Subjects	0.17	0.35	0.15	0.41
E_{peak}/A_{peak}	All Subjects	0.13	0.47	0.12	0.50
VTI_E	All Subjects	0.077	0.68	0.071	0.70
VTI_A	All Subjects	0.16	0.39	0.19	0.29
VTI_E/VTI_A	All Subjects	0.14	0.44	0.15	0.41
kx_0	All Subjects	---	---	0.014	0.94
$½\ kx_0^2$	All Subjects	---	---	0.014	0.94
AT	Without CAD	0.28	0.40	0.25	0.46
AT	With CAD	0.045	0.84	0.041	0.86
DT	All Subjects	0.083	0.65	0.068	0.71
c	Without CAD	---	---	0.30	0.36
c	With CAD	---	---	0.027	0.91
k	Without CAD	---	---	0.29	0.39
k	With CAD	---	---	0.096	0.68
$c^2 - 4k$	All Subjects	---	---	0.084	0.65
$c / (2\sqrt{k})$	Without CAD	---	---	0.24	0.48
$c / (2\sqrt{k})$	With CAD	---	---	0.06	0.80

Table 6-3: Correlation values and their corresponding p-values for the comparisons between the magnitude of cyclic variation and the E- and A-wave parameters corresponding to function and viscoelasticity. n = 32 for all subjects, n = 11 for subjects without coronary artery disease (CAD), and n = 21 for subjects with CAD. No result was significant at the p = 0.05 level.

which potentially will minimize the time and effort required to perform myocardial tissue characterization. As a consequence of a significant number of reported studies, the cyclic variation of backscattered energy appears to be a meaningful approach to the characterization of a range of cardiac pathologies despite the fact that the underlying physical mechanisms responsible have not yet been fully determined. As a step toward determining these mechanisms, the goal of this paper was to relate diastolic function quantitated via the parametrized diastolic filling formalism to the cyclic variation of backscatter, to determine the role of diastolic function in the observed cyclic variation of backscatter.

The parametrized diastolic filling formalism accounts for the mechanical suction pump role of the left ventricle and characterizes Doppler transmitral velocity profile E-waves kinematically, according to the motion of a damped simple harmonic oscillator. Transmitral blood flow velocity is thus a consequence of a balance between chamber derived elastic, inertial, and damping forces as required by Newton's Law. During filling, the elastic driving force that generates recoil is due to systolic loading of elastic elements in the chamber (titin, visceral pericardium, elastin, and collagen[31-33]). Relaxation unmasks these stored elastic forces and thereby generates acceleration forces subject to inertial constraints, which are opposed by resistive (damping) forces. The interaction of these three forces (elastic restoring force, inertia, and damping), in the context of an equation of motion, is reflected in the values of the three mathematically independent model parameters: the spring constant k, the damping constant c, and the initial spring displacement x_o. The equation of motion (Newton's Law, per unit mass)

can be solved for the E-wave velocity, which yields a closed form expression for the E-wave contour, in terms of the model parameters (c, k, and x_o).[27] Thus, this formalism draws a causal connection between the E-wave contours and tissue recoil and associated viscoelasticity. This expression for the E-wave velocity additionally permits the calculation of parameters (*AT, DT, VTI,* E_{peak}, A_{peak}) that are traditionally calculated using a triangular shape approximation for determination of E-wave features.

The relationships between the parametrized diastolic filling model parameters and the underlying myocardial properties permit meaningful inferences to be drawn from comparisons between the parametrized diastolic filling parameters and indices derived from them and the cyclic variation parameters. One set of planned comparisons involved the normalized time delay of cyclic variation and the parametrized diastolic filling parameters and PDF derived indices such as kx_0 *and* $\frac{1}{2}\, kx_0^2$. The results of these comparisons, which indicate statistically significant but modest correlations, are found in Table 6-2. The parameters E_{peak} (the peak E-wave velocity), VTI_E (the velocity-time integral of the E-wave), kx_0 (the maximum force of recoil), and $\frac{1}{2}\, kx_0^2$ (the maximum stored energy prior to recoil) all correlated with the normalized time delay of cyclic variation. The plots for these comparisons are shown in Figures 6-3 and 6-4. For each case, a change in the value of a parametrized diastolic filling parameter, in a manner reflecting poorer diastolic function, results in an increase in the normalized time delay. These results suggest that the normalized time delay of the cyclic variation backscatter data provide information beyond that contained in the more frequently reported magnitude of cyclic variation. Additionally, these results suggest that changes in cardiac function, as assessed by the PDF formalism, might be detected using cyclic variation.

In addition to the trends observed between the normalized time delay of cyclic variation and the parametrized diastolic filling parameters associated with function, a significant correlation was found between the normalized time delay of cyclic variation of backscatter and the indices β and y. Both of these indices characterize the relationship between chamber stiffness and damping/relaxation. It is also of interest that the viscosity (c) and stiffness (k) of the chamber did not independently correlate with the normalized time delay of cyclic variation, even though the parameters β and y were positively correlated, as seen in Figure 6-5. For these subjects, an increase in the normalized time delay corresponded with an increase in the viscosity as well as a decrease in the stiffness, so that subjects with high values of the normalized time delay tended to have less stiff and more viscous hearts. As viscosity associated effects increase relative to stiffness, E-wave contours change in a predictable fashion. Relatively symmetric velocity contours characteristic of normal diastolic function are altered towards a delayed relaxation pattern with blunted peak velocity and prolonged deceleration. From a kinematic perspective, this shift represents the transition from the underdamped ($y<1$) to overdamped ($y>1$) kinematic regime. Thus the results in Figure 6-5 are significant, in so far as they suggest that normalized time delay from cyclic variation and the kinematic regime of filling are consonant, and, by extension, may differentiate between normal vs. delayed-relaxation E-wave patterns. Because these results were obtained using an entirely independent method of diastolic function assessment (kinematic modeling) their agreement with previous reports on the increase in the normalized time delay in subjects who have a decreased elasticity due to remodeling, in presence of diabetes[6, 34] or post-myocardial infarction[8] is particularly noteworthy.

The remaining assessments involved the comparison of the magnitude of cyclic variation with parametrized diastolic filling parameters. The results are shown in Table 6-3. They indicate that the magnitude of cyclic variation did not correlate with any of these individual parameters. The results, coupled with previous studies that indicate that the magnitude of cyclic variation is altered in the presence of function- and structure-altering pathologies, suggest that the magnitude of the cyclic variation of backscatter is primarily influenced by systolic function as opposed to diastolic function.[5, 35, 36]

One result of this study was an identification of the some of the mechanisms involved in generating the systematic variation in backscatter from the myocardium. It has been found in prior studies that the alterations in the magnitude and the normalized time delay of cyclic variation associated with reversible myocardial ischemia recover before the resumption of regional myocardial thickening in stunned but viable myocardium.[4, 37-40] Additionally, the role of perfusion of the tissue has been considered both in studies by Wickline *et. al*.[10] in which perfusion did not appear to be the dominant effect, and by Micari[9] in which perfusion was identified as a major source of the cyclic variation in backscatter. The composition of the tissue, and specifically the amount of collagen present, can alter the overall backscatter level[41-43] but has a less-understood effect on cyclic variation. A model based on changes in impedance has been proposed; this model predicts a decrease in the magnitude of cyclic variation as the collagen content in the heart increases.[10, 11]

The significant correlations shown for this study are modest, but suggest that the active and passive elements of the myocardium have a combined effect on the cyclic variation of backscatter. The lack of significance between any single measure of the

diastolic function or viscoelasticity with the magnitude of cyclic variation, combined with past findings concerning the dependence of the magnitude on active contractile properties, suggests that an active, cycle-dependent physical change in the myocardium is responsible for the changes in the level of backscatter corresponding to cyclic variation. From this perspective, an underlying physical change causes a change in the impedance mismatch between neighboring elements in the myocardium (such as myofibers embedded in the extracellular matrix). Additionally, pathologies that affect this impedance mismatch, either by alteration of the efficiency of the active myofibers or by deposition of stiffer materials such as collagen, would affect measurements of the magnitude of cyclic variation. However, the timing of the systematic change in backscatter during the cardiac cycle is governed not only by contraction but also by the tissue properties governing the relaxation of the myocardium and the subsequent loading of this tissue by the filling of the ventricles. As such, the normalized time delay of cyclic variation, a measure of this timing, would be affected by alterations in the function of the ventricles during diastole, which in turn can be influenced by changes in the global viscoelastic properties of the ventricles.

There were some technical limitations in this study. The study of individuals about to undergo catheterization was beneficial, because this provided a wide spectrum of subjects with a corresponding wide range of cardiac function and myocardial structure. On the other hand, this population represented a significant challenge because of the presence of potentially confounding pathologies. These subjects were difficult to image as a result of a number of factors, including in some cases obesity, age, and a history of smoking, as well as the examination setting (a narrow catheterization table, which

required subjects to lie flat on their back). The possibility that the comparisons between the two methods of tissue characterization were confounded by the presence of coronary artery disease was examined, but ultimately was found to be significant only for the comparison concerning *y*. For the comparison of *y* versus the time delay of cyclic variation, the comparison was only valid for the population with coronary artery disease, perhaps because the range of expressed time delay values was larger for that population. The presence of other pathologies might have also had confounding effects on the comparisons in this study, although the inclusion criteria required that specific pathologies were to be excluded for the study population.

One limitation inherent to the use of cyclic variation is that the particular values for the magnitude and normalized time delay of cyclic variation are dependent on the echocardiographic view and region of interest used in the acquisition of data.[44, 45] This study measured the parameters of cyclic variation using the echocardiographic data from the posterior wall of the left ventricle, as viewed in the parasternal long axis view of the heart. The use of one segment only for the characterization of the myocardium circumvents issues arising from the averaging of data from dissimilar segments. However, the use of other segments (especially the lateral or anterior wall) would be expected to generate different values of the normalized time delay than measured in this study. The observed relationships between the normalized time delay of cyclic variation and the parametrized diastolic filling parameters would be altered by the change in the normalized time delay values, but it is anticipated that the trends would still be consistent with the present findings.

An assumption underlying the use of cyclic variation in this study was that the magnitude and the normalized time delay of cyclic variation were independent parameters, and thus can be independently compared to the E-wave parameters. There are pathologies, such as myocardial infarction and diabetes, which affect both parameters of cyclic variation.[4, 6, 46] Additionally, researchers have sometimes chosen to combine these two parameters into a single parameter, such as the magnitude of cyclic variation weighted by a factor derived from the normalized time delay.[39, 40, 46] There is some precedence for assuming that the underlying mechanisms for the magnitude and the normalized time delay of cyclic variation are different.[8] To test this assumption directly, the magnitude and the normalized time delay of cyclic variation were plotted against each other and any relationship between them determined using linear correlation. These parameters were found to be uncorrelated in the current subject population ($n = 115$ heart cycles, $r = 0.086$, $p = NS$), so the assumption of independence between the cyclic variation parameters seems justified.

In summary, echocardiographic tissue characterization of thirty-two subjects has provided mechanistic insight into the diastolic function to normalized time delay of cyclic variation relation. The determinants include relative viscoelasticity and the viscoelastic ratio determined via the parametrized diastolic filling formalism. By extension, time delay was found to be related to the kinematic regime of filling, which is determined by the balance between stiffness and relaxation chamber properties. Further, the mechanism underlying the magnitude of cyclic variation was not strongly coupled with the mechanism underlying the normalized time delay of cyclic variation.

References

1. Madaras, E.I., B. Barzilai, J.E. Perez, B.E. Sobel, and J.G. Miller, Changes in myocardial backscatter throughout the cardiac cycle. Ultrasonic Imaging 1983;5(3):229-39.
2. Perez, J.E., M.R. Holland, B. Barzilai, S.M. Handley, B.F. Vandenberg, J.G. Miller, et al., *Ultrasonic Characterization of Cardiovascular Tissue*, in *Cardiac Imaging - A Companion To Braunwald's Heart Disease*, D.J. Skorton, H.R. Schelbert, G.L. Wolf, and B.H. Brundage, Editors. 1996, W. B. Saunders Co.: Philadelphia. p. 606-624.
3. Giglio, V., V. Pasceri, L. Messano, F. Mangiola, L. Pasquini, A. Dello Russo, et al., Ultrasound tissue characterization detects preclinical myocardial structural changes in children affected by Duchenne muscular dystrophy. J Am Coll Cardiol 2003;42(2):309-16.
4. Milunski, M.R., G.A. Mohr, J.E. Perez, Z. Vered, K.A. Wear, C.J. Gessler, et al., Ultrasonic tissue characterization with integrated backscatter. Acute myocardial ischemia, reperfusion, and stunned myocardium in patients. Circulation 1989;80(3):491-503.
5. Yuda, S., J. Dart, O. Najos, and T.H. Marwick, Use of cyclic variation of integrated backscatter to assess contractile reserve and myocardial viability in chronic ischemic left ventricular dysfunction. Echocardiography 2002;19(4):279-87.
6. Perez, J.E., J.B. McGill, J.V. Santiago, K.B. Schechtman, A.D. Waggoner, J.G. Miller, et al., Abnormal myocardial acoustic properties in diabetic patients and

their correlation with the severity of disease. J Am Coll Cardiol 1992;19(6):1154-62.

7. Di Bello, V., D. Giorgi, E. Talini, G. Dell' Omo, C. Palagi, M.F. Romano, et al., Incremental value of ultrasonic tissue characterization (backscatter) in the evaluation of left ventricular myocardial structure and mechanics in essential arterial hypertension. Circulation 2003;107(1):74-80.

8. Ohara, Y., Y. Hiasa, S. Hosokawa, N. Suzuki, T. Takahashi, K. Kishi, et al., Ultrasonic tissue characterization predicts left ventricular remodeling in patients with acute anterior myocardial infarction after primary coronary angioplasty. J Am Soc Echocardiogr 2005;18(6):638-43.

9. Micari, A., M. Pascotto, A.R. Jayaweera, J. Sklenar, N.C. Goodman, and S. Kaul, Cyclic variation in ultrasonic myocardial integrated backscatter is due to phasic changes in the number of patent myocardial microvessels. J Ultrasound Med 2006;25(8):1009-19.

10. Wickline, S.A., L.J. Thomas, 3rd, J.G. Miller, B.E. Sobel, and J.E. Perez, A relationship between ultrasonic integrated backscatter and myocardial contractile function. J Clin Invest 1985;76(6):2151-60.

11. Holland, M.R., K.D. Wallace, and J.G. Miller, Potential relationships among myocardial stiffness, the measured level of myocardial backscatter ("image brightness"), and the magnitude of the systematic variation of backscatter (cyclic variation) over the heart cycle. J Am Soc Echocardiogr 2004;17(11):1131-7.

12. Kovács, S.J., Jr., B. Barzilai, and J.E. Perez, Evaluation of diastolic function with Doppler echocardiography: the PDF formalism. Am J Physiol 1987;252(1 Pt 2):H178-87.

13. Lisauskas, J.B., J. Singh, A.W. Bowman, and S.J. Kovács, Chamber properties from transmitral flow: prediction of average and passive left ventricular diastolic stiffness. J Appl Physiol 2001;91(1):154-62.

14. Bauman, L., C.S. Chung, M. Karamanoglu, and S.J. Kovács, The peak atrioventricular pressure gradient to transmitral flow relation: Kinematic model prediction with in vivo validation. J Am Soc Echocardiogr 2004;17(8):839-844.

15. Zhang, W., L. Shmuylovich, and S.J. Kovács, The E-Wave Delayed Relaxation Pattern to LV Pressure Contour Relation: Model-Based Prediction With in vivo Validation. Ultrasound in Medicine & Biology 2010;36(3):497-511.

16. Chung, C.S., D.M. Ajo, and S.J. Kovács, Isovolumic pressure-to-early rapid filling decay rate relation: model-based derivation and validation via simultaneous catheterization echocardiography. J Appl Physiol 2006;100(2):528-534.

17. Riordan, M.M., C.S. Chung, and S.J. Kovács, Diabetes and diastolic function: stiffness and relaxation from transmitral flow. Ultrasound Med Biol 2005;31(12):1589-96.

18. Kovács, S.J., J. Rosado, A.L. Manson McGuire, and A.F. Hall, Can trasmitral Doppler E-waves differentiate hypertensive hearts from normal? Hypertension 1997;30(4):788-95.

19. Rich, M.W., N.O. Stitziel, and S.J. Kovács, Prognostic value of diastolic filling parameters derived using a novel image processing technique in patients > or = 70 years of age with congestive heart failure. Am J Cardiol 1999;84(1):82-6.

20. Dent, C.L., A.W. Bowman, M.J. Scott, J.S. Allen, J.B. Lisauskas, M. Janif, et al., Echocardiographic characterization of fundamental mechanisms of abnormal diastolic filling in diabetic rats with a parameterized diastolic filling formalism. Journal of the American Society of Echocardiography 2001;14(12):1166-1172.

21. Grossman, W., Diastolic dysfunction in congestive heart failure. N Engl J Med 1991;325(22):1557-64.

22. Aeschbacher, B.C., D. Hutter, J. Fuhrer, P. Weidmann, E. Delacretaz, and Y. Allemann, Diastolic dysfunction precedes myocardial hypertrophy in the development of hypertension[ast]. Am J Hypertens 2001;14(2):106-113.

23. Gottdiener, J.S., J. Bednarz, R. Devereux, J. Gardin, A. Klein, W.J. Manning, et al., American Society of Echocardiography recommendations for use of echocardiography in clinical trials: A report from the american society of echocardiography's guidelines and standards committee and the task force on echocardiography in clinical trials. Journal of the American Society of Echocardiography 2004;17(10):1086-1119.

24. Appleton, C.P., M.S. Firstenberg, M.J. Garcia, and J.D. Thomas, The Echo-Doppler evaluation of Left Ventricular Diastolic Function - A Current Perspective. Cardiology Clinics 2000;18(3):513-546.

25. Armstrong, W.F., T. Ryan, and H. Feigenbaum, *Feigenbaum's echocardiography*. 2010, Philadelphia: Wolters Kluwer Health/Lippincott Williams & Wilkins. xv, 785 p.

26. Hall, A.F., J.A. Aronovitz, S.P. Nudelman, and S.J. Kovács, Automated method for characterization of diastolic transmitral Doppler velocity contours: Late atrial filling. Ultrasound in Medicine & Biology 1994;20(9):859-869.

27. Hall, A.F. and S.J. Kovács, Automated method for characterization of diastolic transmitral doppler velocity contours: Early rapid filling. Ultrasound in Medicine & Biology 1994;20(2):107-116.

28. Press, W.H., S.A. Teukolsky, W.T. Vetterling, and B.P. Flannery, *Numerical recipies: The art of scientific computing*. 1986, Cambridge: Cambridge University Press.

29. Holland, M.R., A.A. Gibson, L.R. Peterson, M. Areces, J.E. Schaffer, J.E. Perez, et al., Measurements of the cyclic variation of myocardial backscatter from two-dimensional echocardiographic images as an approach for characterizing diabetic cardiomyopathy. J Cardiometab Syndr 2006;1(2):149-52.

30. Lloyd, C.W., M.R. Holland, and J.G. Miller. *Measurements of the Cyclic Variation of Myocardial Backscatter - Does the Analysis Method Matter?* in *34th International Symposium on Ultrasonic Imaging and Tissue Characterization*. June 10-12, 2009, Arlington, VA: Ultrasonic Imaging, 55.

31. Jobsis, P.D., H. Ashikaga, H. Wen, E.C. Rothstein, K.A. Horvath, E.R. McVeigh, et al., The visceral pericardium: macromolecular structure and contribution to

passive mechanical properties of the left ventricle. Am J Physiol Heart Circ Physiol 2007;293(6):H3379-3387.

32. Granzier, H.L. and S. Labeit, The Giant Protein Titin: A Major Player in Myocardial Mechanics, Signaling, and Disease. Circ Res 2004;94(3):284-295.

33. Robinson, T.F., S.M. Factor, and E.H. Sonnenblick, The heart as a suction pump. Sci Am 1986;254(6):84-91.

34. Wagner, R.F., K.A. Wear, J.E. Perez, J.B. McGill, K.B. Schechtman, and J.G. Miller, Quantitative assessment of myocardial ultrasound tissue characterization through receiver operating characteristic analysis of Bayesian classifiers. J Am Coll Cardiol 1995;25(7):1706-11.

35. Hu, X., J. Wang, Y. Sun, X. Jiang, B. Sun, H. Fu, et al., Relation of ultrasonic tissue characterization with integrated backscatter to contractile reserve in patients with chronic coronary artery disease. Clin Cardiol 2003;26(10):485-8.

36. Naito, J., T. Masuyama, T. Mano, K. Yamamoto, Y. Doi, H. Kondo, et al., Influence of preload, afterload, and contractility on myocardial ultrasonic tissue characterization with integrated backscatter. Ultrasound Med Biol 1996;22(3):305-12.

37. Hancock, J.E., J.C. Cooke, D.T. Chin, and M.J. Monaghan, Determination of successful reperfusion after thrombolysis for acute myocardial infarction: a noninvasive method using ultrasonic tissue characterization that can be applied clinically. Circulation 2002;105(2):157-61.

38. Takiuchi, S., H. Ito, K. Iwakura, Y. Taniyama, N. Nishikawa, T. Masuyama, et al., Ultrasonic tissue characterization predicts myocardial viability in early stage of reperfused acute myocardial infarction. Circulation 1998;97(4):356-62.

39. Wickline, S.A., L.J. Thomas, 3rd, J.G. Miller, B.E. Sobel, and J.E. Perez, Sensitive detection of the effects of reperfusion on myocardium by ultrasonic tissue characterization with integrated backscatter. Circulation 1986;74(2):389-400.

40. Iwakura, K., H. Ito, S. Kawano, A. Okamura, K. Asano, T. Kuroda, et al., Detection of TIMI-3 flow before mechanical reperfusion with ultrasonic tissue characterization in patients with anterior wall acute myocardial infarction. Circulation 2003;107(25):3159-64.

41. O'Donnell, M., J.W. Mimbs, and J.G. Miller, Relationship between collagen and ultrasonic backscatter in myocardial tissue. The Journal of the Acoustical Society of America 1981;69(2):580-588.

42. Picano, E., G. Pelosi, M. Marzilli, F. Lattanzi, A. Benassi, L. Landini, et al., In vivo quantitative ultrasonic evaluation of myocardial fibrosis in humans. Circulation 1990;81(1):58-64.

43. Hoyt, R., D. Skorton, S. Collins, and H. Melton, Jr, Ultrasonic backscatter and collagen in normal ventricular myocardium. Circulation 1984;69(4):775-782.

44. Finch-Johnston, A.E., H.M. Gussak, J. Mobley, M.R. Holland, O. Petrovic, J.E. Perez, et al., Cyclic variation of integrated backscatter: dependence of time delay on the echocardiographic view used and the myocardial segment analyzed. J Am Soc Echocardiogr 2000;13(1):9-17.

45. Vandenberg, B.F., L. Rath, T.A. Shoup, R.E. Kerber, S.M. Collins, and D.J. Skorton, Cyclic variation of ultrasound backscatter in normal myocardium is view dependent: clinical studies with a real-time backscatter imaging system. J Am Soc Echocardiogr 1989;2(5):308-14.

46. Vitale, D.F., R.O. Bonow, G. Gerundo, N. Pelaggi, G. Lauria, D. Leosco, et al., Alterations in ultrasonic backscatter during exercise-induced myocardial ischemia in humans. Circulation 1995;92(6):1452-7.

Chapter 7: Summary and Conclusion

The objective of this thesis was to examine the physics underlying the use of nonlinear ultrasound. This branch of ultrasonics was considered not only in the physical laboratory, but also in its applications for clinical imaging. One of the challenging aspects of nonlinear ultrasound was the reliable measurement of the underlying phenomena. These measurements contain the promise of developing a quantitative tool for characterizing tissue in the medical setting. Thus, steps were taken in the laboratory to demonstrate or test the methods of application of nonlinear ultrasound to measure intrinsic material properties. Additionally, existing methods of measurement from the literature were examined and improved upon, to facilitate the enhanced use of these existing methods in current studies.

In Chapter 2, the generation of a plane wave was discussed in the context of measuring the nonlinearity of materials. These plane waves were generated through the novel use of stainless steel as a "delay line", and the resulting transmission of plane waves were validated not only by simulation, but also by the direct measurement of the ultrasonic pressure. The consequences of this method of transmission were also demonstrated at multiple frequencies.

The through-transmission method of measuring the nonlinearity of materials was analyzed in Chapter 3. The methods in the literature were studied and clarified, and this method was utilized in the study of liquids with known nonlinear parameters. The results of this study demonstrated a reasonable level of accuracy (over an average of many measurements), but did not achieve a high level of precision. This current lack of

precision makes the method untenable at the present time, but this study does illustrate the issues with the measurement method and the potential for future improvement.

In contrast to the through-transmission approaches, backscatter methods of measuring the nonlinearity of materials were described in Chapter 4. These methods were derived from a more general formalism, and some concerns with previously published works have been reconciled. The more generalized methodology described in this section has promise for the potential application in medicine because the necessary measurements are commonplace in both ultrasonic physics and imaging.

Chapter 5 was dedicated to the study of the various approaches of quantifying the cyclic variation of backscatter from the myocardium. When different analysis methods were applied to the same underlying data**,** the reported magnitude of variation was found to be different. A new, automated method of quantifying the magnitude of cyclic variation was introduced and demonstrated. The use of this method as a "gold standard" permitted the delineation of the discrepancies among the various cyclic variation methods. This use of a gold standard also directly demonstrated that the differences in the literature between the reported magnitudes for normal patients were very likely due to the different methods of analysis that had been applied.

The mechanisms underlying the observed cyclic variation of myocardial backscatter over the heart cycle are not fully understood, so the study described in Chapter 6 was performed to examine cyclic variation in the context of diastolic function. Diastolic function was quantified using a parametrized diastolic filling formalism, which describes the filling of the heart according to the dynamics of a damped harmonic oscillator. This formalism was used to describe the myocardium of patients that were

also studied using the cyclic variation method. It was shown that the timing of this cyclic variation of backscatter was related to the kinematic regime of filling, or the stiffness and viscous nature of the myocardium.

The studies performed or proposed in this thesis have implications for the successful implementation of both new and existing methods of characterizing materials. The re-derivation and implementation of the methods of measuring the nonlinear properties of tissues, for example, are of use for the characterization of tissue and the detection of pathology. However, without an accurate and precise method of quantifying these nonlinear properties, the utility of the material parameters regarding nonlinearity as a means of quantifying the state of tissue would remain low. The cyclic variation of myocardial backscatter, on the other hand, has been used to investigate a wide variety of pathologies. The work presented here illustrates a method of unifying the different magnitude of cyclic variation measurements into a single measurement metric. This permits meta-analysis of historic data, as well as provides a standardized tool for current applications in diagnostic medicine. Additionally, the continued understanding of the underlying mechanisms of cyclic variation of myocardial backscatter will deepen the insight of the relationship to physical changes in the myocardium.

Appendix 1: An Experimental Approach to Compensate for the Shift in the Ultrasonic Diffraction Field in Materials with Dissimilar Velocities

List of Parameters used in this Chapter:

a - radius of a transmitting transducer

A - transfer functions, which will be subscripted to indicate their particular role

$\alpha(f,x)$ - attenuation coefficient of the material

β - the slope of the attenuation coefficient, for materials exhibiting an attenuation that is linearly dependent on frequency (such that $\alpha = \beta f$)

c - speed of sound of the material (subscripted to indicate when in specific materials)

d - thickness of a sample material (in a substitution experiment)

E - numerical error term to describe alteration of the received diffractive field (used as a multiplicative term: E =1 signifies no error)

f - frequency of the ultrasonic signal

$J_n(\ )$ - nth order Bessel function

k_r - spatial frequency (wave number), in the radial direction

L - distance between transmitting and receiving transducers (subscripted to indicate specific cases)

λ - wavelength of the ultrasonic signal

$N = \frac{a^2}{\lambda}$ - near field distance of a planar transducer (at this distance, the Fresnel number = 1)

$\Phi(x,y,z)$ - velocity potential at a field point (x,y,z) due to all source points

$R(x,y,z) = \left|\vec{R}(x,y,z)\right|$ - distance between a source point and the field point (x,y,z)

ρ - mass density of a material

$S = \frac{4x\lambda}{a^2}$ - Fresnel parameter (also, related to the inverse of the Fresnel number)

T_I - intensity transmission coefficient

$u_x(0,y,z)$ - particle displacement in the x-direction at the source plane (x = 0)

$V(f)$ - amplitude spectrum received from a transducer

x - axial distance from a transmitting transducer

$Y \equiv \frac{ak_r}{2}$ - dimensionless scale parameter for the radial direction

$Z = \rho \cdot c$ - characteristic acoustic impedance of a material

Introduction

One of the myriad ways to characterize materials using ultrasound is to measure the loss of ultrasonic amplitude as a function of propagation distance through these materials. This loss is commonly referred to as the attenuation of signal through the sample, and can be utilized in several ways. For example, attenuation (and the functional form therein) is a material parameter, which depends on the specific characteristics of the sample (such as the material phase (solid, liquid, or gas) and the various heterogeneities

in the sample). Knowledge of the attenuation of a sample, then, can be used to determine the identity of the sample or changes in the material. Along with other techniques, this determination plays a role in the non-destructive evaluation (NDE) of a material, in which information is gleaned about the bulk of a material without the need to destroy the material in the process. The attenuation of an insonified sample also plays an important role in the detection of scattered signals from deeper inside the sample, and accordingly plays a role in clinical ultrasound. The measurement of other physical parameters, such as the scattering coefficient from the bulk of the sample, is colored by this loss, so a proper compensation for the attenuation within the material is necessary for the subsequent determination of these parameters. For example, the study of human physiology (and pathophysiology) via ultrasonic imaging is hindered by the loss of signal strength due to propagation through the human body, so corrections are employed to produce the desired ultrasonic images. The time-gain compensation (TGC) method is used in imaging to counteract the loss due to attenuation, and consists of an application of a depth- (or, equivalently, time-) dependent gain that is applied to offset the increasing loss during signal propagation.

The loss of ultrasonic signal amplitude as a function of depth, due to scattering and absorption of ultrasound in the material, has an exponential form, and as such can be described by

$$e^{-\alpha(f,x)\cdot x} \tag{A1-1}$$

where α is the attenuation coefficient (and in general can be a function of both position and frequency), and x is the distance propagated in the material of interest. The spatial dependence of the attenuation is not necessarily limited to a specific form, although for

many cases this attenuation is considered to be constant (for homogenous materials, as one example), or has a spatial dependence that can be estimated. The frequency dependence of the attenuation, in the context of liquids and tissue (a liquid-like solid) is often found to obey a power law form,

$$\alpha(f) = \alpha_O \cdot f^n \tag{A1-2}$$

Here, α_O represents a constant value and n is the power law coefficient. Overall, the power law coefficient for the majority of materials ranges from 0 to 2, and for liquids and tissues, the power law coefficient is found to be somewhere at or between 1 and 2.[1] A value of note occurs for soft tissue, where $n \approx 1$ (a linear relationship), and the constant value α_O represents the slope of attenuation with frequency. In this case the attenuation is historically represented with the form

$$\alpha(f) = \beta \cdot f \tag{A1-3}$$

where β is known as the slope of the attenuation coefficient (since the derivative of the attenuation with respect to frequency yields the constant β).

This loss parameter can be determined using either pulse-echo or through-transmission methods. In the former, the loss in the ultrasonic signal due to attenuation can be calculated from a comparison of the received pressure that reflects off of a nearly-perfect reflector, for a reference measurement or when the sample "shadows" the reflector by being interposed between the transducer and the reflector. Such a method is termed a "shadowed reflector" measurement, and is useful for homogeneous samples or samples in which the average attenuation coefficient is of importance. Another pulse-echo method calculates the attenuation coefficient from the sound scattered back from the

interior of a sample, as the signal will lose strength as a function of depth due to the increasing path length for an ultrasonic signal within the attenuating sample. This attenuation can also be calculated from the continuously altered spectral characteristics of the signal as a function of depth, since the attenuation coefficient is in general a function of frequency. The resulting shift in the backscattered frequency spectrum thus can be used to infer the attenuation coefficient, given an assumed functional form of the attenuation.[2, 3] These methodologies have been demonstrated to be viable for clinical diagnoses *in vivo*.[4]

The attenuation coefficient of a material can also be determined by using a through-transmission, substitution method. Instead of utilizing the ultrasonic signals that have scattered off of the inhomogeneities in the material, this method is concerned with the propagation of the transmitted ultrasonic signal through the entire bulk of the interrogated material. Such a measurement is a seemingly straightforward process for relatively homogeneous materials (where the spatial dependence of the attenuation is negligible), because there are only two measurements required: one where the material is absent (a reference measurement) and one where the material displaces some of the reference material.[5] These cases are illustrated in Figure A1-1, and for this comparative study, the attenuation coefficient, in dB/cm, can be determined by

$$\alpha(f) = \frac{1}{d \cdot \left(20\log_{10}(e)\right)}\left[10\log_{10}\left(\frac{\left|V_{ref}(f)\right|^2}{\left|V_{samp}(f)\right|^2}\right) + 10\log_{10}\left(T_I^2\right)\right] \qquad \text{(A1-4)}$$

where V(f) is the received amplitude for the sample and reference measurements, d is the thickness of the material, α is the attenuation coefficient within the material, and T_I^2 is the combined transmission coefficient for entering and leaving the sample. A related

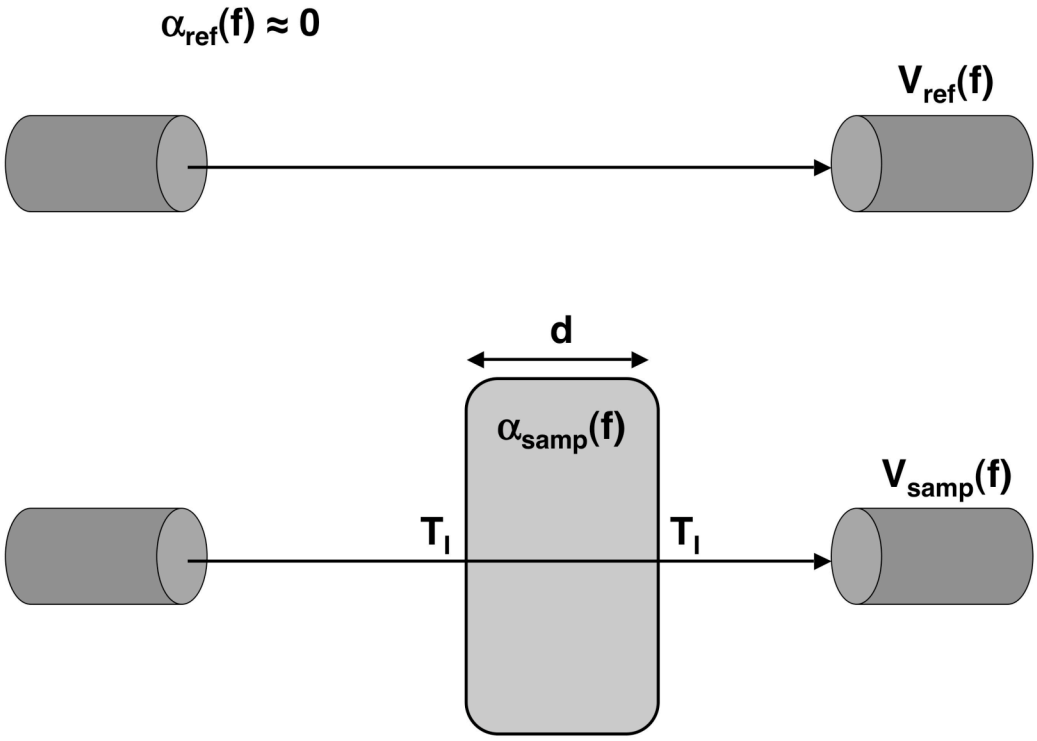

Figure A1-1: A two-step, through-transmission approach for measuring the attenuation coefficient of a material. Above: a reference measurement, when sound passes through only a reference path and is received by a transducer. Below: a sample measurement, when sound passes through a sample, with thickness d, that displaces the same thickness of reference material. The total path length is the same for both cases, and the transmission coefficient between the reference and sample materials is noted.

method, applicable for the study of homogeneous materials, uses two sample measurements, with identical materials but different path lengths.[6] This modification is diagrammed in Figure A1-2, which shows explicitly the difference from Figure A1-1. In this case, the attenuation coefficient, in dB/cm, can be computed from

$$\alpha(f) = \frac{10}{d_{thick} - d_{thin}} \log_{10}\left(\frac{|V_{thin}(f)|^2}{|V_{thick}(f)|^2}\right) \qquad \text{(A1-5)}$$

where the subscripts "thick" and "thin" denote which thickness of material has been used for a particular measurement. The primary advantage of this method is that the

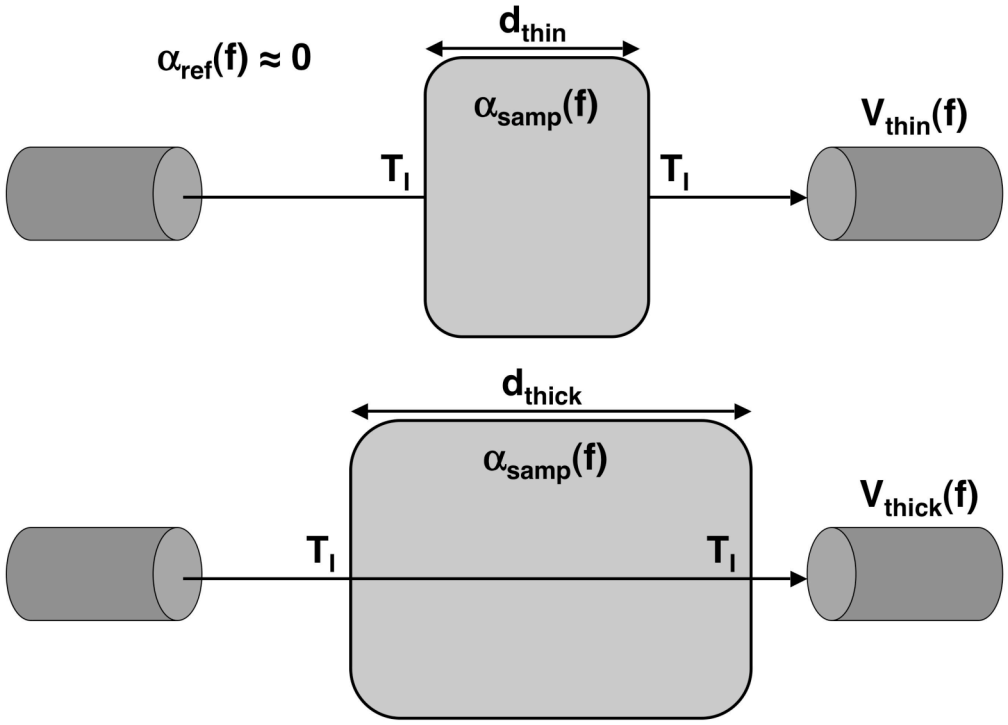

Figure A1-2: An alternative method of determining the attenuation coefficient of a material. Above: a measurement with a fixed total distance between transducers and a "thin" sample interposed between the transducers. Below: a measurement with a "thick" sample instead of the "thin" sample as previously used. No knowledge of the transmission coefficients is needed for this setup, since these coefficients are the same in both cases and will cancel out in a rigorous derivation of the attenuation coefficient of the sample.

compensation for transmission through an interface is not needed, because the interfaces are the same in both measurements.

These formulae make two assumptions regarding the ultrasonic field, which, at a fundamental level, combine to form one assumption for homogeneous materials. They are: the phase cancellation over the face of the receiving transducer is unchanged between measurements, and the axial diffractive pattern is not altered between these measurements. These assumptions are important for the accurate measurement of the attenuation coefficient of the sample, because they permit an experimentalist to assume that the signal loss is primarily due to attenuation within the sample. Should these

assumptions not be valid, there will be an error in the attenuation coefficient measurement because the observed signal loss may have contributions arising from additional factors. The purpose of this Appendix is to explore the consequences of these assumptions on the measurement of the attenuation coefficient of materials, as well as a way to compensate the experimental setup to remove diffractive effects from the measurement. A rigorous theoretical treatment that encompasses the treatment presented here has been previously published by Xu and Kaufman[7] and is included here. These methods are explored because diffraction compensation methods are important in the determination of the attenuation coefficient of samples used in the nonlinear experiments.

Ad hoc determination of the axial correction factor

The earlier work of Kirk Wallace, Ph.D., highlighted the utility of physical delay lines in the generation of ultrasonic beams.[8, 9] These studies utilized the ultrasonic signal that was transmitted through delay lines in order to measure the nonlinear parameter of a material. The term "delay line" is somewhat of a misnomer in this case, because the material employed was stainless steel, and the speed of sound in steel is greater than that of the water in which we usually operate (so that a signal propagating through steel arrives sooner rather than later, and thus is not "delayed"). In these earlier works from our group, the delay lines served two purposes. One purpose, which is of lesser concern here, is the decreased level of nonlinear generation in the delay line, because the increased density and speed of sound in the steel result in a shock formation distance that is far longer than the corresponding distance in water. The other purpose, of primary concern for this Appendix, is that the diffractive field of the ultrasonic beam is effectively

compressed (for materials where the speed of sound is greater than that of the surrounding medium). As a result, with the use of these delay lines the appropriate location in the diffractive field could be obtained in a much smaller physical distance.

One particular distance of note is the near field distance of a planar transducer (termed N), which is the last and strongest of the maxima in the ultrasonic field in the axial direction, corresponding to the natural focus,

$$N = \frac{a^2}{\lambda} \cdot \left[1 - \left(\frac{\lambda}{2a} \right)^2 \right] \approx \frac{a^2}{\lambda} \tag{A1-6}$$

where a is the radius of the transmitting transducer and λ is the wavelength of the emitted ultrasonic signal.[10] The term in the parentheses (λ / (2a)) is small for the transducers used in these studies (1/2" to 1" diameters) over the frequency ranges employed (typically, the low megahertz range). Discarding the term results in an error on the order of one percent or less. This approximate distance can be used for locating the peak pressure in the field for an experimental setting, such that a receiving transducer for an experiment might start at the calculated near field distance, and then be moved slightly around the near field distance to find the strongest ultrasonic pressure.

The utility of the delay line is demonstrated by recasting the near field distance as a function of sound speed (which will vary according to the material present),

$$N = \frac{a^2 f}{c} \tag{A1-7}$$

where c is the sound speed of a material and f is the frequency of the signal. If the frequency and aperture radius are constant, then an increasing sound speed results in a decreasing near field distance. For the case of a steel delay line compared to water, the speed of sound increase by roughly a factor of four, which corresponds to a decrease of

the near field distance by a factor of four. In experiments performed in this laboratory, steel delay lines were utilized to avoid prohibitively long propagation distances in water, by compressing the diffractive field inside of the steel.

The *ad hoc* derivation of the axial diffractive effects proceeds in the following way. Equation A1-7 can be reordered, such that

$$N \cdot c = \text{constant} = a^2 f \qquad \text{(A1-8)}$$

This reordering serves to isolate two groups of terms: terms on the right that do not change for a given experimental setup (because the frequency of interest and the aperture of the transmitting transducer are fixed), and terms on the left that are related in an inverse fashion. One interpretation of equation A1-8 is that the near field distance of a transducer will change in an inverse manner with the material speed of sound that is found in the field. A broader interpretation is that, for a given fixed position in the diffractive field (not necessarily the near field distance), the propagation distance to that diffractive field location must vary inversely with the speed of sound for the material in which the ultrasonic pressure wave propagates. The latter interpretation is the primary concern here, because the issue is one of calculating the proper propagation distance to maintain a given diffractive effect.

Consider two propagation path lengths for determining the attenuation of a sample material as illustrated in Figure A1-3. In this case the two path lengths are permitted to differ between the two measurements. With equation A1-8 in mind, the location of the receiving transducer in the axial diffraction field is such that the product of the propagation distance, L_{ref}, and the speed of sound for the reference material (typically water), c_{ref}, is fixed. For the measurement of a sample material with a speed of

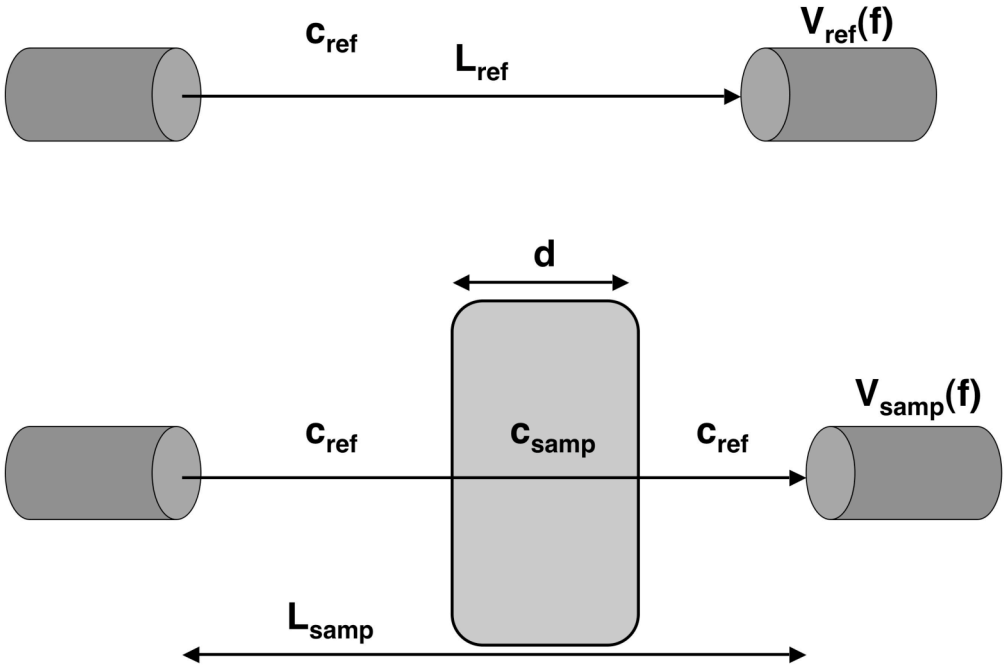

Figure A1-3: A modification of the experimental setup shown in Figure A1-1. Above: a reference measurement setup, with the speed of sound and the propagation length for the reference labeled. Below: a sample measurement setup, with the speeds of sound in each regime labeled, along with the requisite lengths. Notice that the total propagation length is not fixed to be the same as in the reference measurement.

sound c_{samp} and thickness d, the optimal position of the receiver L_{samp} is such that the total propagation through the axial diffractive field of the thickness of the sample as well as the remaining reference material is matched to the reference-only measurement, i.e.,

$$L_{ref}c_{ref} = \text{constant} = \left(L_{samp} - d\right)c_{ref} + dc_{samp} \tag{A1-9}$$

Equation A1-9 can be reorganized to solve for the position of the receiver when the sample is present,

$$L_{ref} = L_{samp} - d + d\frac{c_{samp}}{c_{ref}} \tag{A1-10}$$

$$L_{samp} = L_{ref} + d \cdot \left(1 - \frac{c_{samp}}{c_{ref}} \right) \tag{A1-11}$$

Equation A1-11 has three regimes for the relative speeds of sound, which will be discussed in the context of a fixed reference path length. The easiest to interpret is when the speeds of sounds in the sample and the reference materials are the same. The result from equation A1-11 is that the two total path lengths are the same irrespective of the sample thickness. If the speed of sound in the sample is greater than that of the reference (as in the steel delay line experiment), the ratio of speeds is greater than one, and the term in parentheses is negative. Thus, the total path length for the sample measurement must be shorter than the reference measurement, by a factor proportional to the thickness of the sample. On the other hand, if the speed of sound in the sample is less than that of the reference, this ratio will be less than one and the term in parentheses is positive. In this case, the total path length must be greater than in the reference measurement, so that the receiving transducer must be moved away from the transmitting transducer in order to sample the same location in the diffractive field.

Ad hoc validation by simulation

In a further *ad hoc* attempt to validate equation A1-11, another approach was used based on a custom software tool known as VirtualTank, or colloquially as vTank. This software is a simulation package that was written and maintained by Kirk Wallace during his time in the group. This software is capable of simulating the propagation of ultrasonic signals through regions of varying material properties, for a wide variety of geometric configurations and boundary conditions. Further, one of the output options for

this simulation package is a numerical sampling of the ultrasonic pressure along the primary transducer axis (the axial pressure). The hypothesis of this software experiment is that, by simulating the two measurements required for the calculation of an attenuation coefficient, the resulting effects on the axial pressure pattern would be easily detected.

However, the illustration of the changes in the axial diffractive field must be shown independently of any other effect due to loss. This requires a choice of material properties such that the attenuation of the pressure field can be neglected, and the transmission of pressure into and out of the sample must be lossless. The former condition is straightforward, because the attenuation of both the host and sample medium can be set to zero identically. Thus, the simulation will not include any loss from attenuation by design. The transmission coefficient for this scenario must be one to avoid insertion losses, or alternatively the reflection coefficient for the measurement must be zero. The intensity transmission coefficient for an ultrasonic signal between two materials (for insonification normal to the surface) is

$$T_I^{1\to 2} = T_I^{2\to 1} = \frac{4Z_1Z_2}{\left(Z_1 + Z_2\right)^2} \tag{A1-12}$$

where $Z = \rho c$ is the acoustic impedance of a material (which is an approximation for when α/k is much less than one). Note that the intensity transmission coefficient is symmetric, and that the coefficient goes to one when

$$\left(Z_1 + Z_2\right)^2 = 4Z_1Z_2 \tag{A1-13}$$

$$Z_1^2 + 2Z_1Z_2 + Z_2^2 = 4Z_1Z_2 \tag{A1-14}$$

$$Z_1^2 + Z_2^2 = 2Z_1Z_2 \tag{A1-15}$$

which can only be satisfied for $Z_1 = Z_2$. Thus, if the properties of the reference material are known, then for a given speed of sound for the sample, a transmission coefficient of one results for

$$\rho_{samp} = \rho_{ref} \cdot \frac{c_{ref}}{c_{samp}} \tag{A1-16}$$

For this simulation, the water properties were taken to be 1500 m/s for the speed of sound and 1 gm/cm^3 for the mass density. Using a speed of sound of 1220 m/s for the sample material (corresponding to a simulation of isopropanol previously performed[8]), the density used for the simulation corresponds to 1.2295 gm/cm^3.

Two simulations were performed: one simulation using only a lossless reference medium, and another simulation where the sample material, with a slower speed of sound than the reference, takes the place of the reference medium between 40 and 80 mm distance from the transmitting transducer. The results of this simulation are depicted in Figure A1-4 (with a subset shown in Figure A1-5 to highlight more explicitly the difference between the two simulations). Here, the change in the pressure field can be seen as a deviation of the dotted line (the sample path) away from the reference path. This change begins at 40 mm (the start of the sample material) and reaches its largest deviation at 80 mm (the end of the sample material). For this simulation the sample material has a slower speed of sound than the reference material, which means that the axial diffractive field is expanded for the propagation length in the sample material. Accordingly, the peak axial pressure is shifted to a larger distance away from the transducer, and at locations beyond the peak pressure the sample pressure is consistently larger than the reference pressure.

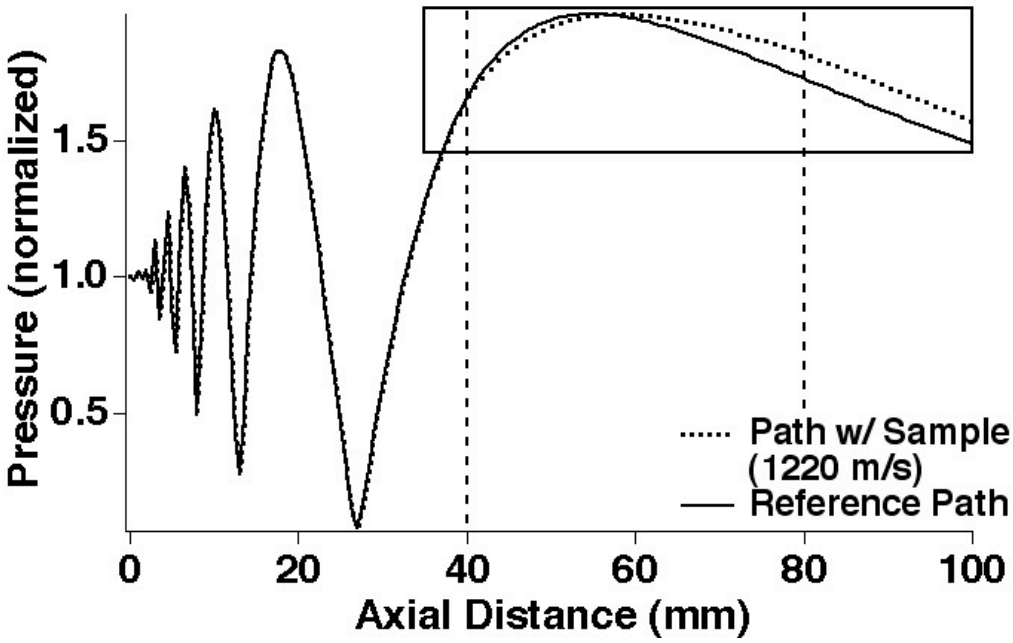

Figure A1-4: Simulated pressure profiles for two different measurements, using vTank to calculate the field pressures. The solid line corresponds to a reference path, where the simulated pressure results from transmission from a source piston transducer propagating through a medium with no attenuation and a speed of sound of 1500 m/s (an approximation for water). The dotted line corresponds to a path where, at 40 mm, a sample with a speed of sound of 1220 m/s (representing isopropanol) with no attenuation replaces the water path for 40 mm. The cutout box refers to Figure A1-5.

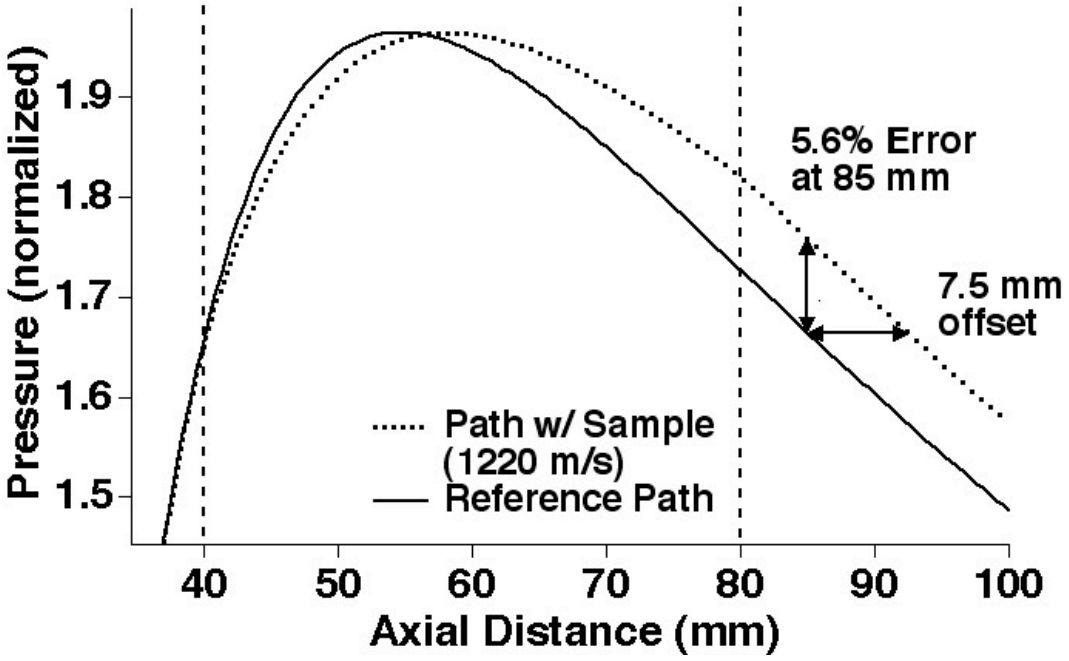

Figure A1-5: A subset of Figure A1-4, to illustrate better the change in the simulated pressure field due solely to the interposition of a 40 mm-deep sample of isopropanol (in the distance between 40 and 80 mm). The error in the pressure is expressed, as well as the offset required to bring the receiving transducer in the sample measurement to the equivalent location in the reference diffractive field.

As demonstrated in Figure A1-5, at a distance of 85 mm from the plane of transmission, a receiving transducer would overestimate the pressure passing through the sample by 5.6%, when accounting for the diffractive field alone. The amount of error this overestimation corresponds to for the attenuation coefficient depends on the value for the true attenuation coefficient. Additionally, for some circumstances, it is possible that this error causes the calculation of the attenuation coefficient to return an unphysical value of a negative (or zero) value. Physically, this would mean that the propagation of an ultrasonic signal through the material of interest results in a gain instead of a loss. This interesting (but physically impossible) result can be found by deriving the values for the experimental parameters for which the calculated attenuation coefficient would be zero,

$$\alpha_{calc}(f) = \frac{1}{d \cdot \left(20\log_{10}(e)\right)}\left[10\log_{10}\left(\frac{\left|V_{ref}(f)\right|^2}{\left|V_{samp}(f)\right|^2}\right) + 10\log_{10}\left(T_I^2\right)\right] = 0 \qquad \text{(A1-4)}$$

$$\log_{10}\left(\frac{\left|V_{ref}(f)\right|^2 T_I^2}{\left|V_{samp}(f)\right|^2}\right) = 0 \qquad \text{(A1-17)}$$

$$\left|V_{ref}(f)\right|^2 T_I^2 = \left|V_{samp}(f)\right|^2 \qquad \text{(A1-18)}$$

The sample term in the equations above is composed of four terms: the measured reference term again, along with a simple numerical modification (E, a multiplicative term) that is currently used to illustrate the error due to the altered diffractive field, the transmission coefficients into and out of the sample (hence, the term is squared), and the exponential loss term that represents the loss inside the sample. These are substituted into equation A1-18, which results in

$$\left|V_{ref}(f)\right|^2 T_I^2 = \left|V_{ref}(f)\right|^2 E^2 T_I^2 e^{-2\alpha d} \qquad \text{(A1-19)}$$

By canceling terms and reorganizing, the true material attenuation that would result in a calculated attenuation coefficient of zero would be

$$\frac{1}{E^2} = e^{-2\alpha d} \tag{A1-20}$$

$$\alpha = -\frac{1}{d}\ln\left(\frac{1}{E}\right) \tag{A1-21}$$

For the values of this particular simulation (E = 1.056, d = 40 mm), $\alpha = 0.0136$ Np cm^{-1}, such that if the true attenuation of the sample were equal to or smaller than this value, the naively calculated attenuation would be negative or, at best, zero. This is a relatively small value for many materials of interest, but for isopropanol the attenuation coefficient at 2.25 MHz is roughly 0.014 Np cm^{-1}. Experimentally this error can be remedied either by working deeper in the far field for the attenuation measurements (which reduces the value of E, since the error in the pressure between the shifted and unshifted pressure fields decreases with increasing distance, past the focus) or by moving the receive transducer slightly further back (by 7.5 mm in this example) for the sample measurements, to eliminate the error from the experiment as much as possible.

A derivation of the fractional error involved in the calculated value of the attenuation coefficient can also be considered. This calculated value is intended to represent the value of the attenuation coefficient that is obtained for a stationary (unadjusted) receiving transducer. For this, the subscripts "calc" and "true" will be used to separate the calculated attenuation value from the true material coefficient,

$$\alpha_{calc}(f) = \frac{1}{d\cdot\left(20\log_{10}(e)\right)}\left[10\log_{10}\left(\frac{\left|V_{ref}(f)\right|^2}{\left|V_{samp}(f)\right|^2}\right) + 10\log_{10}\left(T_I^2\right)\right] \tag{A1-4}$$

$$2\alpha_{calc}(f)d\log_{10}(e) = \log_{10}\left(\frac{\left|V_{ref}(f)\right|^2 T_I^2}{\left|V_{ref}(f)\right|^2 T_I^2 E^2 e^{-2\alpha_{true}d}}\right) \tag{A1-22}$$

where the substitution for V_{samp} has been made as in equation A1-19,

$$2\alpha_{calc}(f)d = \ln(10)\cdot\log_{10}\left(\frac{e^{2\alpha_{true}(f)d}}{E^2}\right) \tag{A1-23}$$

Exponentiation of both sides of the equation results in

$$e^{2\alpha_{calc}(f)d} = \frac{e^{2\alpha_{true}(f)d}}{E^2} \tag{A1-24}$$

$$e^{2\left(\alpha_{calc}(f)-\alpha_{true}(f)\right)d} = \frac{1}{E^2} \tag{A1-25}$$

$$\left(\alpha_{calc}(f)-\alpha_{true}(f)\right)\cdot 2d = \ln\left(\frac{1}{E^2}\right) = -2\ln(E) \tag{A1-26}$$

$$\frac{\alpha_{calc}(f)-\alpha_{true}(f)}{\alpha_{true}(f)} = \frac{-\ln(E)}{\alpha_{true}(f)d} \tag{A1-27}$$

Thus, the fractional error in the calculated value of the attenuation coefficient relies on three terms: the true attenuation coefficient, the thickness of the sample (which, combined with the attenuation coefficient, yield the true loss in the system, neglecting diffraction effects), and the natural logarithm of the error term that describes the diffractive effect. Limited to the focal zone or the far field, there are two behaviors that are seen. First, for speeds of sound in the sample that are slower than the reference medium, the error term E is greater than one, and the calculated attenuation will underestimate the true attenuation. This occurs as the change in the diffractive field acts as an effective gain, which masks a portion of the attenuation. Conversely, for speeds of sound in the sample that are faster than the reference medium, the error term is less than

one, and the calculated attenuation will overestimate the true material attenuation. Here, the diffractive field advances into the far field faster in the fast material, and the subsequent decreased signal at the receiver is interpreted as an additional loss. These general statements are limited to the focal and far field, however, because of the nature of these fields: the diffractive pressure field remains a monotonically decreasing function of distance in this regime. The compression or rarefaction of the axial diffractive field thus obeys simple relationships in this special case – for different diffractive behaviors such as the near field (where the pressure varies rapidly with distance in a non-monotonic fashion) equation A1-11 is still correct, but the diffractive error E cannot be easily derived without simulation.

One final issue with the error involved in the attenuation coefficient measurement concerns the minimization of error when the experiment cannot be readily changed to accommodate this diffractive effect, and one total path length is used for the entirety of the experiment. Equation A1-27 shows that the fractional error in the measured attenuation coefficient is related both to the total loss due to the sample as well as a term related to the error between the reference diffractive field and the sample diffractive field. As such, this fractional error can be minimized in two ways. The first (and more obvious from many applications) is to simply make the total loss bigger by increasing the amount of material that is insonified in the sample path. However, the difference in value between the error term E and the error-free value of one is related to the thickness of the material, as thicker materials will affect the diffractive field more than thinner materials. Additionally, it is not always an option to increase the thickness of a material specimen, for a number of reasons (sample container sizes are limited, specimen sizes are fixed,

etc.). The other way to minimize the error would be to reduce the impact of the error term. This term is not only related to the speed of sound and the thickness of the material, but also the location in the diffractive field. For locations in the field that are varying rapidly, the error term potentially could be quite significant. In the limit of true plane wave propagation, though, the change in the diffractive field with respect to distance is zero, and the error would also go to zero. Because a true plane wave is hard to generate, one can consider a location in the diffractive field where the spatial derivative is small – the corresponding error in the attenuation measurement will also be small. The focal zone works well for small distances; for larger required distances of adjustment the far field would also suffice (and the deeper into the far field, the better for the minimization of error, which will be a tradeoff between the pressure required in the field to make a measurement of the attenuation coefficient and the minimization of the error in such a measurement).

Derivation of the diffraction compensation by Xu and Kaufman

Xu and Kaufman published a rigorous treatment of the axial diffraction effects in their 1993 manuscript. To illustrate the equivalence of their method with that described above, the relevant sections will be reproduced here for comparison. There are two diffraction corrections that are derived by Xu and Kaufman: a theoretical diffraction correction used to numerically compute a correction to the calculated value of the slope of the attenuation coefficient (β), and an experimental diffraction correction used to calculate a corrected water path only transducer separation, needed for the correct measurement of the attenuation coefficient. The former is of potential future use to other

investigators looking to numerically compensate for the effects of diffraction, whereas the latter is of more immediate use for experimenters seeking to physically eliminate the error, as well as to illustrate an alternate method of deriving equation A1-11 from above.

Motivation: Analytic description of an attenuation measurement

In a manner similar to the motivation described above, Xu and Kaufman were interested in the accurate measurement of the attenuation of a sample material (in their case, a plastic called Lucite). For a measurement of a reference material that spans a distance x between two transducers, the received amplitude spectrum is

$$A_{ref}(f,x) = A_{diff}^{ref}(f,x) \cdot \left[A_T(f) A_R(f) A_{signal}(f) \right] \qquad \text{(Xu 2)}$$

where the subscripts "T" and "R" refer to the electronic efficiencies of the transmitting and receiving transducers, "signal" refers to the electronic excitation signal used to stimulate the transmitting transducer, and "diff" refers to the effects of diffraction in the propagation length, for this reference measurement. Similarly, for the same setup except with the sample included, the received amplitude spectrum becomes

$$A_{samp}(f,x) = A_{samp}(f) A_{diff}^{samp}(f,x) \cdot \left[A_T(f) A_R(f) A_{signal}(f) \right] \qquad \text{(Xu 1)}$$

where the diffraction effects are explicitly different and a sample transfer function is included to explicitly represent the lossy effects due to the material itself. Division of equation (Xu 1) by equation (Xu 2) reveals the diffraction dependence in the measured material transfer function,

$$\frac{A_{samp}(f,x)}{A_{ref}(f,x)} \equiv \hat{A}_{samp}(f) = A_{samp}(f) \frac{A_{diff}^{samp}(f,x)}{A_{diff}^{ref}(f,x)} \qquad \text{(Xu 3)}$$

So, the estimate of the material transfer function, $\hat{A}_{samp}(f)$, is affected by the respective diffractive fields associated with the two measurements. Accordingly, another transfer function can be defined as the ratio between these two diffraction functions,

$$A_{diff}(f,x) \triangleq \frac{A_{diff}^{samp}(f,x)}{A_{diff}^{ref}(f,x)}. \qquad \text{(Xu 4)}$$

For materials in which the attenuation coefficient is linear with frequency, such that a slope of attenuation can be defined (equation (Xu 3) above), the actual value for the slope of attenuation can be expressed by

$$\beta = \frac{20}{fd} \cdot \left[\log_{10}\left(A_{ref}(f,x)\right) - \log_{10}\left(A_{samp}(f,x)\right) + \log_{10}\left(A_{diff}(f,x)\right) \right] \qquad \text{(Xu 8)}$$

The error comes with the estimate of the slope of the attenuation coefficient when the compensation for the diffraction contribution is not implemented. This can be accomplished either by the calculation of this diffraction term so that it can be inserted into Xu's equation 8, or by alteration of the experiment such that the diffraction term is equal to one (and the log of the diffraction term goes to zero, eliminating the error).

Theoretical diffraction correction

Assuming a transducer of radius a located at the origin and directed in the +x direction, the velocity potential of the field is cited as being[11]

$$\Phi(x,y,z) = -\frac{1}{2\pi}\int_S u_x(0,y',z')\frac{e^{-ikR}}{\vec{R}}dS' \qquad \text{(Xu 9)}$$

where u_x is the axial particle displacement at the face of the transmitting transducer (at x = 0), R is the distance (or vector) from the origin to the field point (x,y,z), and k is the

wave number (or spatial frequency). This can be transformed using the Hankel transform to eventually find the average particle displacement at a distance x as

$$\bar{u}_x(f,x) = 2u_0 e^{-ikx} \int_0^\infty \frac{J_1^2(Y)}{Y} e^{iY^2(S/4\pi)} dY \qquad \text{(Xu 13)}$$

where $Y = ak_r/2$ is a dimensionless scaling parameter, and $S = (4\lambda x/a^2)$ is the Fresnel parameter. This definition differs from other definitions of the Fresnel number as well as the calculation of the near field distance, by the factor of four that has been inserted into the Fresnel parameter and the factor of two that has been inserted into the dimensionless scaling parameter. These factors of two come from the use of a radius in the equations instead of a diameter, but if kept consistent throughout these factors will not matter.

With this expression for the theoretical particle displacement field, a theoretical diffraction correction can be determined and then plugged directly in Xu's equation 8 to find the slope of the attenuation coefficient directly. If the Fresnel approximation holds, then the Fresnel parameter can be used to find the effects of diffraction, by assuming that the total Fresnel parameter is the sum of the Fresnel parameters in the individual regimes. Thus, for the experimental setup containing a sample of thickness d, which resides between two transducers located a distance x apart,

$$S = S_{ref} + S_{samp} = \frac{4(x-d)\lambda_{ref}}{a^2} + \frac{4d\lambda_{samp}}{a^2} \qquad \text{(Xu 14)}$$

which describes the total propagation in the sample experiment. However, one can also consider an apparent wavelength that describes the same total propagation,

$$\lambda_{app} = \frac{(x-d)\lambda_{ref} + d\lambda_{samp}}{x} \qquad \text{(Xu 15)}$$

and an apparent Fresnel parameter $S_{app} = 4x\lambda_{app} / a^2$ which is used to evaluate the particle displacement at the receiver in Xu's equation 13 to describe the diffraction of the ultrasonic field in the sample material measurement. This can also be interpreted as the wavelength required for a material, which spans the full distance between the ultrasonic transducers, to produce the same diffractive effect as the sample – reference complex found in the true sample path measurement.

This wavelength can be utilized in the analytic description of the diffractive effects of the sample experiment. Each of the diffractive transfer functions for the two different experiments can be described as a normalized, averaged particle displacement,

$$A_{diff}^{samp}(f,x) = \left| \frac{u_{x,app}(f,x)}{u_0} \right| = \left| 2e^{-ik_{app}x} \int_0^\infty \frac{J_1^2(Y)}{Y} \cdot e^{iY^2\left(S_{app}/4\pi\right)} dY \right| \qquad \text{(Xu 16)}$$

where the apparent wave number and apparent Fresnel parameter are defined by the apparent wavelength from above, and

$$A_{diff}^{ref}(f,x) = \left| \frac{u_{x,ref}(f,x)}{u_0} \right| = \left| 2e^{-ik_{ref}x} \int_0^\infty \frac{J_1^2(Y)}{Y} \cdot e^{iY^2\left(S_{ref}/4\pi\right)} dY \right| \qquad \text{(Xu 17)}$$

The diffractive transfer function from Xu's equation 4 is then the ratio of these two functions, which can be reduced to

$$A_{diff}(f,x) = \left| \frac{\int_0^\infty \frac{J_1^2(Y)}{Y} \cdot e^{iY^2\left(S_{app}/4\pi\right)} dY}{\int_0^\infty \frac{J_1^2(Y)}{Y} \cdot e^{iY^2\left(S_{ref}/4\pi\right)} dY} \right| \qquad \text{(Xu 20)}$$

This expression can be evaluated to provide a value for Xu's equation 8, so that the error found in the measurement of the slope of the attenuation coefficient can be corrected numerically.

Experimental diffraction correction

The other method described by in Xu and Kaufman[7] is, by their statement, "a simpler method" for properly compensating for the diffraction effect. In this method, assume that the apparent Fresnel parameter for the sample measurement (S_{app}) is known. Additionally, consider that the total path length in the sample path measurement, L_{samp}, is known and fixed for this purpose. With these known, the "diffraction corrected transducer separation distance" can be determined for the reference material-only path, such that the Fresnel parameter for this corrected reference is equal to the apparent Fresnel parameter for the sample measurement. This distance, L_{ref}^{*}, can be derived from the starting equation $S_{ref} = S_{app}$ and results in

$$L_{ref}^{*} = \frac{\left(L_{samp} - d\right)\lambda_{ref} + d\lambda_{samp}}{\lambda_{ref}} \qquad \text{(Xu 22)}$$

For comparison to the *ad hoc* derivation above, the wavelengths from Xu's equation 22 can be converted into speeds of sound, and the equation is then rearranged to find

$$L_{ref}^{*} = L_{samp} - d + d\frac{c_{samp}}{c_{ref}} \qquad \text{(A1-28)}$$

$$L_{samp} = L_{ref}^{*} + d - d\frac{c_{samp}}{c_{ref}} \qquad \text{(A1-29)}$$

$$L_{samp} = L_{ref} + d \cdot \left(1 - \frac{c_{samp}}{c_{ref}}\right) \qquad \text{(A1-11)}$$

This illustrates that these two derivations reach the same operational formula for the transducer separation distance adjustment necessary to correct for the effects of diffraction. Further, under these conditions, the Fresnel parameters from Xu's equation

20 are the same (because the reference Fresnel parameter is explicitly matched to the sample Fresnel parameter), and the diffraction correction term from equation (Xu 20) goes identically to one. So, by changing the reference path length in this fashion, the diffraction error in the measurement of the slope of attenuation goes to zero, and thus does not need to be numerically calculated.

Verification of the utility of the diffraction correction

The theoretical diffraction compensation discussed earlier also has the benefit of being conducive to the determination of the error due to diffraction for a wide range of cases, because this error can be calculated numerically. Given that the speed of sound for both the reference and the sample are fixed, as is the thickness of the sample, the error in the slope of the attenuation coefficient can be determined for a wide range of axial propagation distances. For the data shown by Xu and Kaufman[7] these values were: 2710 m/s for the speed of sound for the sample, 1500 m/s for the reference speed, and 2.4 cm for the thickness of the sample. Additionally, the transducer radius was fixed at 0.95 cm (corresponding to a ¾" diameter transducer), and the frequency ranges examined were from 350 to 600 kHz, and additionally from 750 kHz to 1.25 MHz. The slope of attenuation was determined for these frequency ranges using a least-square fitting approach over the bandwidth, which was performed at total distances ranging from 5 to 30 cm from the transmitting transducer.

As discussed earlier, if the speed of sound in the sample is greater than in the reference material, the corresponding change in the diffractive field is expected to lead to an overestimation of the attenuation coefficient, at least in the focal region and in the far

field. The maximum overestimation is calculated and recast as a maximum relative error for a range of slopes of the attenuation coefficient (since the relative error is of more concern), and plotted in figures in the papers. The maximum relative error approached 2000% for a true attenuation of 0.1 dB cm^{-1} MHz^{-1}, and decreased as the true attenuation increased, which is expected because the true loss grows increasingly dominant compared to the diffractive loss. It is noted that, even for relatively large values of the slope of the attenuation coefficient (1 to 10 dB cm^{-1} MHz^{-1}) the relative error is still 100% to 30%, respectively, for the lower frequency range (and is still 80% to 10% for the 750 to 1250 kHz range). Additionally, for the figures showing the slope of the attenuation coefficient with respect to propagation distance, there is a region, in which the propagation distance is still small (5 to 9 cm), where negative values of the estimated slope of the attenuation coefficient are seen, even with the large (and positive) difference in speed of sound between the sample material and the reference material. This negative result is likely the result of a measurement that is taken in the near field for the reference measurement (as the near field distance is 5 to 7 cm over this bandwidth (see equation A1-7)), and the corresponding shift of the sample path's diffraction field (that does not match the near field of the reference path) can lead to varying results.

The work of Xu and Kaufman also demonstrates the validity of both corrective measures through a direct demonstration on experimental data (above and beyond the simulated case). For this case, instead of simulating the diffraction correction, a physical experiment is performed, and the two corrective techniques are employed. For the uncorrected data in this case, the error in the estimate of the slope of the attenuation coefficient, compared to the known slope, was 28% and 95% for a 1 MHz and a 500 kHz

transducer through-transmission setup, respectively. The first correction applied was the theoretical diffraction correction, and using this method the error in the measurement of the slope of the attenuation coefficient was reduced to 7.9% and 17%, respectively. The other method employed was the experimental diffraction correction, in which a different path length was used for the reference path to compensate for the change in the diffractive field. Using this method, the errors were reduced to 7.6% and 31%, respectively. Both methods demonstrate an improvement in the measurement of the slope of the attenuation coefficient. The choice of method to use depends on the ability of an investigator either to numerically compute the integrals for the theoretical correction, or to alter the total path length of an experiment for the experimental correction.

Historically, the work that many members of this Laboratory have performed involved the study of mammalian tissue specimens (primarily heart tissues), in which the attenuation of the samples are of moderate size but the speed of sound for these samples is very closely matched to that of the standard reference material, water. Using equation A1-11 and the appropriate sample and reference sound velocities (1540 and 1500 m/s, respectively), the correction term for the total sample path length can be seen as being a few percent of the sample thickness. For many measurements this tissue thickness is no more than a few centimeters, so the corresponding change in path length is less than a millimeter. Over this small distance the change in the pressure field is correspondingly small, for the pressure fields employed in physical experiments in the low-megahertz frequency range. Hence, for these measurements, it is unlikely that a correction for the diffraction in the sample path is necessary. However, there have also been experiments

in this Laboratory on non-tissue materials, such as graphite-epoxy laminates, metals, and alcohols, where the speeds of sound differ appreciably from the standard reference material (water). In these cases, care must be taken to take the change in the diffractive field into account for the measurement of the attenuation coefficient, or handle the experiment in a different manner (such as using a well-matched reference or no reference, using a pulse-echo method that doesn't require a reference, working in the deep far field, etc.).

Summary

The measurement of the attenuation coefficient of a material can be useful for a number of reasons, but this measurement can be confounded if there is a substantial contribution from the diffraction of the ultrasonic field. This effect can be important if either

- the speed of sound for the sample being measured is significantly different than that of the reference material, or
- the attenuation coefficient of the sample is small enough that the diffractive loss becomes a significant portion of the total loss in a through-sample measurement.

In cases where the additional effects of diffraction can alter the measured value for the attenuation coefficient, there are methods, both experimental and numerical, to correct for the diffraction that occurs in the field. This Appendix has summarized both an *ad hoc* manner that this diffraction correction can be determined as well as a detailed derivation from the existing literature that is in agreement with the *ad hoc* results.

References

1. Szabo, T.L., Causal theories and data for acoustic attenuation obeying a frequency power law. The Journal of the Acoustical Society of America 1995;97(1):14-24.
2. Flax, S.W., N.J. Pelc, G.H. Glover, F.D. Gutmann, and M. McLachlan, Spectral characterization and attenuation measurements in ultrasound. Ultrasonic Imaging 1983;5(2):95-116.
3. Blodgett, E.D., P.H. Johnston, and J.G. Miller. *Estimating Attenuation in Composite Laminates Using Backscattered Ultrasound*. in *IEEE 1984 Ultrasonics Symposium*. November 14-16, 1984, Dallas, TX: IEEE, 748-753.
4. Parker, K.J., M.S. Asztely, R.M. Lerner, E.A. Schenk, and R.C. Waag, In-vivo measurements of ultrasound attenuation in normal or diseased liver. Ultrasound in Medicine & Biology 1988;14(2):127-136.
5. Baldwin, S.L., K.R. Marutyan, M. Yang, K.D. Wallace, M.R. Holland, and J.G. Miller, Measurements of the anisotropy of ultrasonic attenuation in freshly excised myocardium. The Journal of the Acoustical Society of America 2006;119(5):3130-3139.
6. Madsen, E.L., J.A. Zagzebski, and G.R. Frank, Oil-in-gelatin dispersions for use as ultrasonically tissue-mimicking materials. Ultrasound in Medicine & Biology 1982;8(3):277-287.
7. Xu, W. and J.J. Kaufman, Diffraction correction methods for insertion ultrasound attenuation estimation. Biomedical Engineering, IEEE Transactions on 1993;40(6):563-570.

8. Wallace, K.D., C.W. Lloyd, M.R. Holland, and J.G. Miller, Finite amplitude measurements of the nonlinear parameter B/A for liquid mixtures spanning a range relevant to tissue harmonic mode. Ultrasound in Medicine and Biology, Ultrasound Med Biol 2007;33(4):620-9.

9. Lloyd, C.W., K.D. Wallace, M.R. Holland, and J.G. Miller, Plane wave source with minimal harmonic distortion for investigating nonlinear acoustic properties. The Journal of the Acoustical Society of America 2007;122(1):91-96.

10. Kinsler, L.E., A.R. Frey, A.B. Coppens, and J.V. Sanders, *Fundamentals of Acoustics, 4th ed.* 2000, New York: John Wiley and Sons, Inc. 179-184.

11. Kino, G.K., *Acoustic Waves: Devices, Imaging, and Analog Signal Processing*. 1987, Englewood Cliffs, NJ: Prentice Hall.

Appendix 2: Specific Details Concerning the Acquisition of Backscatter Data In an Echocardiographic Setting

The purpose of this Appendix is to briefly describe and discuss two important considerations for the measurement of the cyclic variation of backscatter from myocardium. The first section of this Appendix addresses the specific methods that were employed to collect the requisite data from a patient in an echocardiographic setting. The second section, meanwhile, discusses the specifics of the various methods of measuring the cyclic variation from the data acquired from these patients. Specific mention is given to the exact method of measurement for the auto-averaged method, which is of interest as a calibration standard in Chapter 5.

Configuration of the Current Echocardiographic System

Prior to the commencement of the study described in Chapter 5, the relationship between changes in displayed grayscale levels and changes in backscatter expressed in dB was determined using a phantom with known scattering properties (CIRS Model 047; CIRS, Norfolk, VA). In order to verify the linearity of the system and to determine the optimal range of grayscale to be employed, this phantom was imaged at a series of gain settings.[1, 2] The compression and grayscale settings were held fixed at the values that would later be used with subjects (40 dB and the M1 grayscale map, respectively). This approach provided an approximately linear mapping of the backscattered power to the grayscale magnitude, with a further grayscale remapping employed during the subsequent

offline analysis. Together these resulted in a mapping that was linear to within 0.5 dB over the 20 dB range used in echocardiographic imaging of subjects.

For each subject, a sequence of video clips was recorded, each consisting of echocardiographic data over three or four cardiac cycles. During this sequence, the overall gain between video clips was systematically changed in 2 dB steps over the previously determined permissible range of grayscale. These echocardiographic clips, acquired with specific gain settings, permitted subsequent analyses to be performed on data acquired using an optimal level of gain for the individual subject. The acquired movie files were downloaded to a server for subsequent offline analysis.

For analysis, the clips were read with a DICOM reader (Osirix, available at no cost from http://www.osirix-viewer.com/). As described above, a remapping of the gray scale values was performed to achieve a linear relationship between the received backscattered signal and the displayed gray scale. A single region of interest was defined in the mid-myocardium of the posterior wall of the left ventricle, and the mean grayscale value in the region of interest was determined for each frame of the echocardiographic video clip. The grayscale values were converted into backscatter values in dB using the linear relationship determined for the grayscale mapping. Individual heart cycles were identified using the start of systole as a marker for delineation.

Details of the Methods of Analysis of Cyclic Variation

In addition to automated methods of determining the magnitude of cyclic variation, this parameter can be estimated by experienced human observers. This manual approach has the benefit of being directly analogous to the methods that have been

historically used (and are still in use) by clinical investigators. Simply, this method involves the examination of the varying backscatter from a region of interest of the heart, and the subsequent assignment of a magnitude of variation by a human observer. Presumably, the underlying method employed by a human observer is the suppression of noise in the signal, followed by the determination of a representative variation between the maximum and minimum levels in the backscatter. Additionally, this direct approach can subsequently be studied, in the context of the automated approaches, as a calibration tool for these automated approaches.

A previously described algorithm was employed for the automated model-fit approach.[3, 4] The measured backscatter data from the region of interest for a heart cycle was interpolated to 101 points and low-pass filtered with thirty-one passes of a three-point binomial filter. A rectangular pulse, whose width was fixed to that of the systolic interval of the heart as determined from the echocardiogram, was then constructed, and was similarly filtered. The model was fitted to the backscattered data, first by maximizing the similarity between the model and the data by correlation of the model function, and then by rescaling the model according to a selective spectral power approach.[4] The magnitude of cyclic variation was found for this method by taking the difference between the high and low values of this appropriately scaled model function.

This model-fit approach has been used previously and can be used to assess whether the current approach for manually estimating values of the magnitude of cyclic variation is consistent with that employed in previously published studies. In Figure A2-1, the results obtained in the present study by the experienced investigators using manual estimates of the magnitude of cyclic variation are compared with results of the model-fit

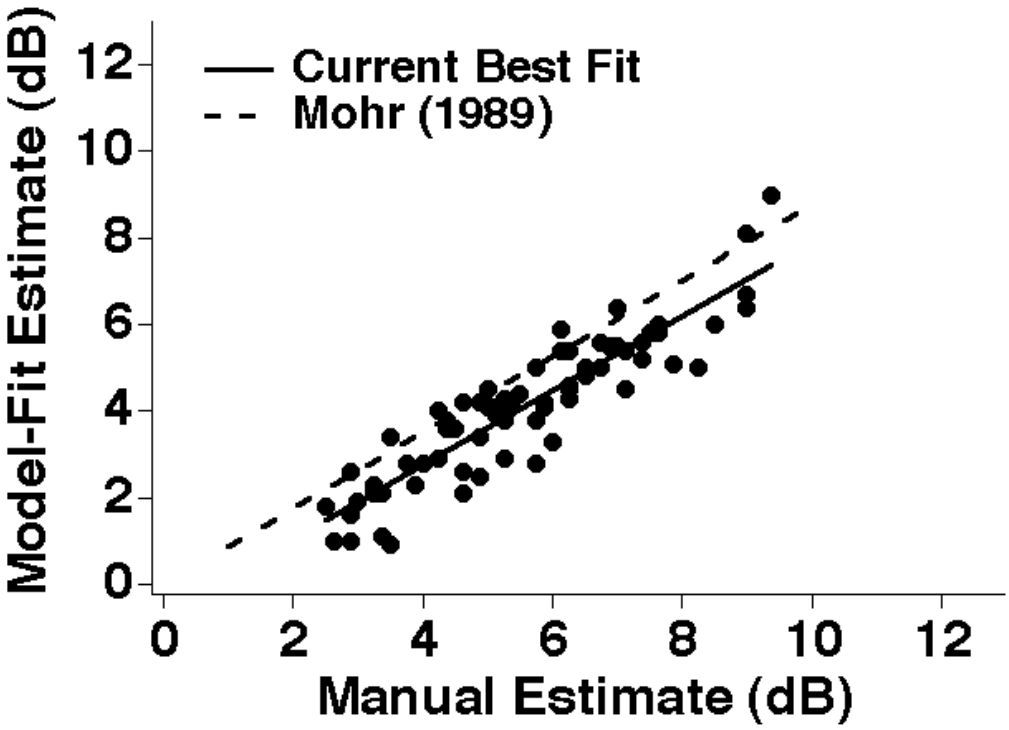

Figure A2-1: A comparison of the results of the current study with the results presented in Figure 7 of the study by Mohr (1989), which introduced the model-fit method. The magnitude of cyclic variation obtained with the model-fit approach carried out by the current investigators is compared with the manually estimated values. The line of best fit comparing the model-fit results to manual estimates obtained from the 1989 manuscript is superimposed.

method, in the same manner as Mohr.[4] The regression line for the present study (with slope 0.86) is essentially the same as that for Mohr (with slope 0.88), suggesting that the manually estimated values for the present study do not exhibit a magnitude-dependent bias. The offset value shown in Figure A2-1 is reasonable, given the potential for variations among different operators in manual estimation, but illustrates the benefits of an automated method, such as the auto-averaged approach, for estimation of the magnitude of cyclic variation.

For the auto-averaged approach, the backscatter data for each heart cycle are interpolated to 101 points, corresponding to values ranging from zero to one hundred percent of the heart cycle. After the application of a specific number of passes of a (low

pass) binomial filter, a percentage of high values and low values of backscatter are then averaged. Optimization of these two parameters (degree of low pass filtering and percentage of high and low values to average) was achieved by plotting the resulting data against the manual results of experienced investigators and iterating until the line of best fit had a slope of 1.0, an intercept of 0, and the best achievable degree of correlation. The optimum choices were determined to be fifteen passes of a three-point binomial filter and averaging the top and bottom fifteen percent of the data. A summary of the auto-averaged approach, as well as the manual analysis approach that is being reproduced on average with the auto-averaged approach, is illustrated in Figure A2-2.

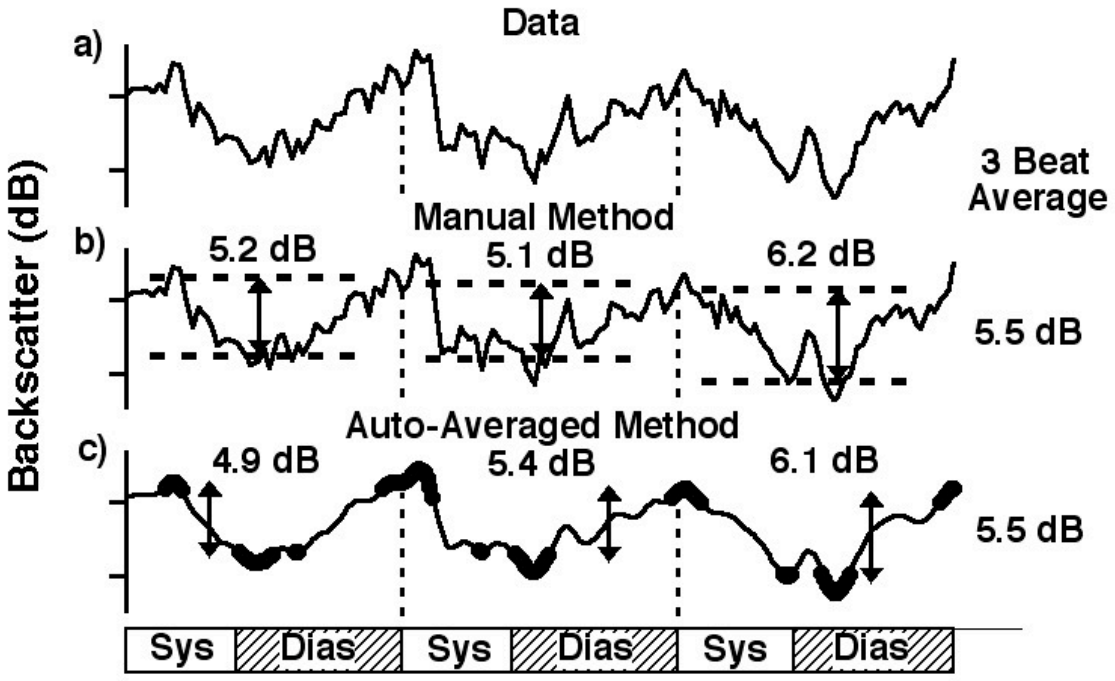

Figure A2-2: Backscatter in decibels (dB) shown over three cardiac cycles of a specific patient. a) Unprocessed data. b) Results of manual determination of the magnitude of the cyclic variation of backscatter by four experienced observers. c) Results obtained using the newly introduced auto-averaged method.

References

1. Finch-Johnston, A.E., H.M. Gussak, J. Mobley, M.R. Holland, O. Petrovic, J.E. Perez, et al., Cyclic variation of integrated backscatter: dependence of time delay on the echocardiographic view used and the myocardial segment analyzed. J Am Soc Echocardiogr 2000;13(1):9-17.
2. Holland, M.R., A.A. Gibson, C.A. Kirschner, D. Hicks, A. Ludomirsky, and G.K. Singh, Intrinsic myoarchitectural differences between the left and right ventricles of fetal human hearts: an ultrasonic backscatter feasibility study. J Am Soc Echocardiogr 2009;22(2):170-6.
3. Mobley, J., C.E. Banta, H.M. Gussak, J.E. Perez, and J.G. Miller, Clinical Tissue Characterization: Online Determination of Magnitude and Time Delay Myocardial Backscatter. Video Journal of Echocardiography 1995;5(2):40-48.
4. Mohr, G.A., Z. Vered, B. Barzilai, J.E. Perez, B.E. Sobel, and J.G. Miller, Automated determination of the magnitude and time delay ("phase") of the cardiac cycle dependent variation of myocardial ultrasonic integrated backscatter. Ultrasonic Imaging 1989;11(4):245-59.